

2020

Suspension Near-Field Electrospinning: a Nanofabrication Method of Polymer Nanoarray Architectures for Tissue Engineering

Alexander R. Nagle
University of Wollongong

Follow this and additional works at: <https://ro.uow.edu.au/theses1>

University of Wollongong

Copyright Warning

You may print or download ONE copy of this document for the purpose of your own research or study. The University does not authorise you to copy, communicate or otherwise make available electronically to any other person any copyright material contained on this site.

You are reminded of the following: This work is copyright. Apart from any use permitted under the Copyright Act 1968, no part of this work may be reproduced by any process, nor may any other exclusive right be exercised, without the permission of the author. Copyright owners are entitled to take legal action against persons who infringe their copyright. A reproduction of material that is protected by copyright may be a copyright infringement. A court may impose penalties and award damages in relation to offences and infringements relating to copyright material.

Higher penalties may apply, and higher damages may be awarded, for offences and infringements involving the conversion of material into digital or electronic form.

Unless otherwise indicated, the views expressed in this thesis are those of the author and do not necessarily represent the views of the University of Wollongong.

Recommended Citation

Nagle, Alexander R., Suspension Near-Field Electrospinning: a Nanofabrication Method of Polymer Nanoarray Architectures for Tissue Engineering, Doctor of Philosophy thesis, Intelligent Polymer Research Institute, University of Wollongong, 2020. <https://ro.uow.edu.au/theses1/787>

Suspension Near-Field Electrospinning: a Nanofabrication Method of Polymer Nanoarray Architectures for Tissue Engineering

Alexander R. Nagle

PhD Candidate, University of Wollongong.

Submitted in fulfillment of the requirements for the award of the doctoral degree:
PhD in Synthetic Biosystems

Conducted at the University of Wollongong - Intelligent Polymer Research Institute, ARC
Centre of Excellence for Electromaterials Science, Wollongong, NSW, Australia.

April 2020

Certification

I, Alexander R. Nagle, declare that this thesis, submitted in fulfillment of the requirements for the award of Doctor of Philosophy in the School of Chemistry, University of Wollongong, is wholly my own work unless otherwise referenced or acknowledged. This document is submitted as a thesis by compilation, containing published, accepted or submitted articles as the main body. The document has not been submitted for qualifications at any other academic institution.

Alexander R. Nagle

1st April 2020

Acknowledgements

I would like to start by thanking Prof. Michael Higgins, the lead research supervisor, whose excellent and patient supervision guided me through this research. I wish to thank Prof. Gordon Wallace for his supervision, his commitment and thoughtful, inventive ideas. I would like to thank Dr. Cormac Fay whose expertise, support and hard work made this research possible. I would like to thank Dr. Xungai Wang for his advice and support; and Xie Zhigang for his help and expert training. I would like to thank Tony Romeo, who's support and technical expertise made developing methods for SEM analysis achievable. I would like to thank Dr. Paul Molino, and Dr. Binbin Zhang, for their advice and support.

To the researchers and students at the Intelligent Polymer Research Institute, thank you all for your help and inspiration. I would like to thank in particular Mr. Grant Barnsley, Dr. Holly Warren and Mr. Thomas Robinson. To all those I have worked alongside with, my sincerest thanks.

To my friends; you certainly made things interesting, and to my family, thank you for your patience and love.

Table of Contents

Certification	1
Acknowledgements	2
Table of Contents	3
List of Figures	7
List of Tables	10
List of Publications and Submitted Manuscripts	11
List of Abbreviations and Notation	12
Chapter 1. Introduction	14
1.1. Preface	14
1.2. Neural Cell Therapy	14
1.2.1. Neural Tissue Trauma	14
1.2.2. Current Neural Cell Therapies	15
1.2.3. Neural Stem Cell Microenvironment	16
1.2.4. Biomaterial Criteria	19
1.2.5. Fiber Hydrogel Composites	21
1.3. Nanofiber Fabrication Techniques	22
1.4. Electrospinning	25
1.4.1. Introduction to Electrospinning	25
1.4.2. Solution Parameters	28
1.4.2.1. Solvent	28
1.4.2.2. Solute	29
1.4.2.3. Synthetic Polymers	32
1.4.2.4. Electrical Properties	35
1.4.3. Process Parameters	37
1.4.3.1. Electric Field	37
1.4.3.2. Flow Rate	38
1.4.3.3. Capillary Tip	38
1.4.3.4. Collector Configuration	39
1.4.3.5. Ambient Conditions	40
1.5. Near Field Electrospinning	42
1.5.1. Limitations of FFES	42
1.5.2. NFES 2D Patterning	43
1.5.3. NFES 3D Patterning	47
1.5.3.1. 3D Melt Electrowriting	48
1.5.3.2. Novel 3D NFES	50
1.5.4. 3D Suspension Electrospinning Techniques	52
1.6. Thesis Aims	56
1.6.1. Thesis Structure	57
1.6.1.1. Chapter 2.	57
1.6.1.2. Chapter 3.	58

1.6.1.3. Chapter 4.	58
1.6.1.4. Chapter 5.	58
1.7. Supplementary Section	59
Chapter 2. A Direct 3D Suspension Near-Field Electrospinning Technique for the Fabrication of Polymer Nanoarrays.	60
2.1. Abstract	61
2.2. Introduction	62
2.3. Materials and Methods	64
2.3.1. Materials	64
2.3.2. NFES Device	64
2.3.2.1. Instrumentation	64
2.3.2.2. Software Design	65
2.3.3. Accuracy Validation	66
2.3.3.1. Planar NFES Dimensional Accuracy and Precision	66
2.3.4. Suspended Nanofiber Fabrication	67
2.3.4.1. Electrode Fabrication and Mounting	67
2.3.5. Characterisation	69
2.3.5.1. Light Microscopy	69
2.3.5.2. Scanning Electron Microscopy (SEM)	70
2.4. Results and Discussion	71
2.4.1. Accuracy Validation by Planar Nanofiber Patterning	71
2.4.2. 3D Suspended Nanofiber Array Fabrication	72
2.4.2.1. Nanofiber Suspension by Square Wave pattern	72
2.4.3. Nanofiber Suspension by Square Iteration Pattern	74
2.4.3.1. Characterizing Fiber Diameter	75
2.4.3.2. Discussion of Technique and Outlook	77
2.5. Conclusions	79
2.5.1. Acknowledgements	80
2.6. Supplementary	81
Chapter 3. Patterning and Process Parameter Effects in 3D Suspension Near-Field Electrospinning of Nanoarrays	84
3.1. Abstract	85
3.2. Introduction	85
3.3. Materials and Methods	88
3.3.1. Materials	88
3.3.1.1. Materials	88
3.3.1.2. Apparatus	88
3.3.1.3. Electrode Fabrication and Mounting	89
3.3.2. Suspended Nanoarray Fabrication	90
3.3.2.1. Parameter Variation Study	90
3.3.2.2. Iteration Study	91

3.3.2.3. Patterning Variation	92
3.3.3. Characterisation	93
3.3.3.1. Rheological Analysis	93
3.3.3.2. Light Microscopy	93
3.3.3.3. Scanning Electron Microscopy	94
3.3.3.4. Image Analysis	94
3.3.3.5. Statistical Analysis	96
3.4. Results and Discussion	96
3.4.1. Effects of Process Parameters on Nanoarrays	96
3.4.1.1. Effect of Process Parameters on Nanoarray Distribution	97
3.4.1.2. Effect of Process Parameters on Nanoarray Fiber Diameter	99
3.4.2. Effect of Pattern Iteration on Fibre Number and Diameter	101
3.4.3. Pattern Variation	104
3.4.3.1. Effect of Pattern and Maximum Speed on Nanoarray Distribution	104
3.4.3.2. Effect of Pattern and Maximum Speed on Fibre Density	105
3.5. Conclusions	106
3.5.1. Acknowledgements	108
3.6. Supplementary Section	109
3.6.1. Centroid Function	109
3.6.2. Fiber Count Functions	110
3.6.3. Image Analysis Process	112
3.6.4. Electric Field Simulation	113
3.6.5. PEO Rheological Characterisation	114
3.6.6. Effects of Parameter Variation	115
3.6.7. Fiber Examples	118
3.6.8. Video Files	118
Chapter 4. Suspended Three-dimensional Polycaprolactone Nanofibers Encapsulated within a Gelangum Methacrylate Hydrogel for Neural Tissue Engineering	119
4.1. Introduction	120
4.2. Materials and Methods	124
4.2.1. Materials	124
4.2.2. NFES System	124
4.2.3. Synthesis of Gellan Gum Methacrylate	125
4.2.4. Suspended Nanofiber Fabrication	125
4.2.5. Encapsulation of Nanofiber Arrays	127
4.2.6. Rheological and Dynamic Mechanical Analysis	129
4.2.7. Optical Characterisation	130
4.2.7.1. Light Microscopy	130
4.2.7.2. Scanning Electron Microscopy (SEM)	130
4.2.7.3. Laser Confocal Fluorescence Microscopy	130
4.2.7.4. Image Analysis	131
4.2.7.5. Statistical Analysis	131

4.3. Results and Discussion	132
4.3.1. Effect of Changing Polymer Concentration on Fibre Diameter and Construct Properties	132
4.3.2. Effect of Changing Iteration and Electrode Structure on Fiber Array and Construct Properties	137
4.4. Conclusions	141
4.5. Acknowledgements	142
4.6. Supplementary Section	143
Chapter 5. Conclusions and Future Perspective	146
5.1. Conclusions	146
5.2. Future Perspectives	149
References	151

List of Figures

<u>Chapter 1</u>	17
Figure 1.1: Neural extracellular matrix (nECM)	
Figure 1.2: ECM protein networks	19
Figure 1.3: Far-field electrospinning (FFES)	26
Figure 1.4: Timeline of electrospinning history	27
Figure 1.5: Emission process	43
Figure 1.6: Electric field effects in novel direct write NFES	46
Figure 1.7: MEW scaffolding	49
Figure 1.8: Novel NFES methods	52
Figure 1.9: Suspension ES techniques	54
 <u>Chapter 2</u>	
Figure 2.1: Design of the NFES system	65
Figure 2.2: Electrode and pattern design	69
Figure 2.3: Planar nanofiber patterning	72
Figure 2.4: Microscopy and analysis of suspended nanofiber arrays	73
Figure 2.5: Square pattern generation of suspended nanofiber arrays	75
Figure 2.6: SEM and diameter distributions	76
Figure 2.7: Automatic cleaning device	81
Figure 2.8: Graphic user interface	82

Figure 2.9: Microscopy images of 2D patterned nanofibers on silicon substrate using varied working distances	83
--	----

Chapter 3

Figure 3.1: System schematic	89
Figure 3.2: Pattern variations	93
Figure 3.3: R patterned nanofibrous arrays	98
Figure 3.4: Orientation distribution statistics across varying process parameters	99
Figure 3.5: Fibre number and diameter as a function of process parameters	101
Figure 3.6: Iteration studies	102
Figure 3.7: Pattern variation	105
Figure 3.8: Pattern variation statistical information	106
Figure 3.9: Centroid function	19
Figure 3.10: Fibre counting macro function	111
Figure 3.11: Image analysis processing steps for microscopy and SEM	112
Figure 3.12: Simulation of electric field lines as the emitter moves relative to the electrode pillars at a voltage of 1.6kV	113
Figure 3.13: PEO rheology	114
Figure 3.14: Fiber variation as a function of process parameter variance	116
Figure 3.15: Intersection per fiber number variation as a function of process parameter setting in raster pattern SNFES	117
Figure 3.16: SEM micrographs of PEO arrays exhibiting (a) fibre bundling and (b) fibre fusing	118

Chapter 4

Figure 4.1: Electrodes and toolpath routes for patterns	127
Figure 4.2: A) Viscosity of PCL solutions in AA:FF (3:1) as a function of concentration at shear rate of 10 Hz	134
Figure 4.3: Characterisation of GGMA-array constructs with arrays of varying fiber diameter	136
Figure 4.4: Iteration and electrode variation	140
Figure 4.5: Viscosity of PCL solutions as a function of shear rate	143
Figure 4.6: Microscopy of fiber arrays on four- and eight-pillar electrodes with varying iteration (15, 60)	144

List of Tables

Chapter 1

Table 1.1. Established nanofiber production methods.	24
Table 1.2. Synthetic electrospinning materials for biofabrication.	34
Table 1.3. Linear and planar electrode suspension electrospinning	55
Table 1.4. 3D electrode suspension electrospinning.	56
Table 1.5. Electrospinning timeline	59

Chapter 3

Table 3.1. Orthogonal sample grouping T1. Constants 1.6kV and 14 wt% PEO.	91
Table 3.2. Orthogonal sample grouping T2. Constants S_{max} of 50mm.s ⁻¹ and WD of 1 mm	91

List of Publications and Submitted Manuscripts

Published Articles:

1. Nagle, A. R., Fay, C. D., Zhigang X., Wallace, G. G., Wang, X., and Higgins M. J. A Direct 3D Suspension Near-Field Electrospinning Technique for the Fabrication of Polymer Nanoarrays. *Nanotechnology* (2019).¹
2. Nagle A. R., Fay C. D., Zhigang X., Wallace G. G., Wang, X. & Higgins M. J. Patterning and Process Parameter Effects in 3D Suspension Near-Field Electrospinning of Nanoarrays. *Nanotechnology* (2019).²

Submitted Articles:

3. Nagle A. R., Fay C. D., Robinson T., Zhilian Y., Wallace G. G. & Higgins M. J. Suspended Three-dimensional Polycaprolactone Nanofibers Encapsulated Within a Gellan Gum Methacrylate Hydrogel for Neural Tissue Engineering. Submitted to *Materials Science & Engineering C* (2019)

Thesis by Compilation Declaration

The author of this thesis is the first author of the above papers, which are either in print or under review, as stated. These substantiate the main body of this thesis, Chapters 2 through 4.

List of Abbreviations and Notation

2D - Two Dimensional
3D - Three Dimensional
AC - Alternating Current
ACD - Automatic Cleaning Device
ANOVA - Analysis of Variance
ECM - Extracellular Matrix
ES - Electrospinning
FFES - Far-field Electrospinning
GelMa - Gelatin Methacrylate
HV - High Voltage
HV-PSU - High Voltage Power Supply Unit
IDC - insulation displacement contact
MES - Melt Electrospinning
MEW - Melt Electrowriting
MSC - Mesenchymal Stem Cells
MTC - Microtissue Constructs
 M_v - Molecular Weight
nECM - Neural Stem Cell Extracellular Matrix
NFES - Near-field Electrospinning
NOI - Normalised Orientation Index
NSC - Neural Stem Cell
NTE - Neural Tissue Engineering
OD - Orientation Distribution
OI - Orientation Index
PASA - Poly(Amide-Sulfonamide)
PCB - Printed Circuit Board
PCL - Polycaprolactone
PEO - Poly(ethylene oxide)
PLA - Poly(Lactic Acid)
PLGA - Poly(Lactic-co-Glycolic Acid)

PVDF - Polyvinylidene Fluoride

R - Raster

R^2 - R-squared

RH - Relative Humidity

RS-232 - Recommended Standard 232

SCI - Spinal Cord Injury

SEM - Scanning Electron Microscopy

Si - Square Iteration

SLM - Selective Laser Melting/Melt

S_{max} - Maximum Speed

SNFES - Suspension Near-Field Electrospinning

SVZ - Subventricular Zone

TBI - Traumatic Brain Injury

TE - Tissue Engineering

USB - Universal Serial Bus

WD - Working Distance

Chapter 1. Introduction

1.1. Preface

This chapter is divided into six sections. The first will discuss the issue of nerve tissue loss, and the strategies of therapy (1.1). The second describes the role of nanofabrication in tissue engineering (1.2). The third section details the theoretical background of electrospinning in terms of solution and process parameters (1.3). The fourth section introduces near-field electrospinning (NFES), recent advances in this field and the principles of NFES techniques (1.4). The fifth section details objectives for a tissue engineered construct for neural cell therapy, and presents possible viable solutions (1.5). The sixth summarizes the aims and structure of this thesis (1.6).

1.2. Neural Cell Therapy

1.2.1. Neural Tissue Trauma

In the brain; disease, oxygen deprivation and traumatic brain injury (TBI) cause permanent damage; leading to debilitating symptoms of cognitive, motor, and psychotic dysfunction. Spinal cord injury (SCI) and TBI are the most detrimental nerve injuries, due to the severe health ramifications, the scale of those affected, and the high cost of treatment. The brain is limited in its ability to self-repair traumatic or chronic injury, as neurogenesis is restricted to specific niches within the adult brain ³, and so therapeutic intervention is required to return lost function. After sustaining a severe brain injury, those who do not die within the first few months are often left with disabilities and pain for the rest of their lives.

Current clinical therapies focus on minimising further damage and ameliorating symptoms ⁴⁻⁸. For example, in the case of TBI, clinical strategies focus on ensuring oxygen supply and blood flow to the brain as well as alleviating symptoms via pharmaceuticals and mobility rehabilitation. In the event of haemorrhage, surgical intervention to remove subdural haematomas may be necessary. However, these treatments are limited when it comes to achieving complete faculty recovery, as they do not address the loss of tissue incurred post-trauma.

Nerve cell therapy aims to address nerve tissue loss through the application and development of neural tissue cells (neural cells and supporting neuroglia); as well as precursor cells (allogeneic or autologous neural stem cells (NSCs)). Transcranial intraparenchymal ^{9,10} injections are the most commonly performed administration of neural cell therapy ¹¹. Transplant cell therapy can be enhanced by a growth medium: a tissue engineered (TE) scaffold, surgically implanted at the site of trauma, either before or after glial scar formation ^{12,13}. The encompassing supposition of neural tissue engineering (NTE) is that imitating the natural microenvironment of the system will lead system specific or precursor cells to proliferate and develop naturally to form macro-scale living tissue. The application of these therapies in clinical settings on a large scale, remains limited ¹¹, only being applied in preclinical models and there remains a number of challenges to address before NSC therapies can be applied in broad clinical treatments ^{14,15}.

1.2.2. Current Neural Cell Therapies

Cell therapies aim to reinnervate damaged tissue, but are hindered by poor stem cell survival and uncontrolled differentiation of transplanted cells ^{16,17}. Tissue engineering scaffolds for cell therapy are designed to mimic the native growth tissue by providing cues to seeded cells ¹⁸. Survival and differentiation of cells rely on environmental cues: neurotrophic factors, molecules which promote cell adhesion, dynamic forces, topographical features, and the presence of other cell types ^{4,19}. A scaffold implant, enriched with neurotrophic factors and binding peptides, provides cues to seeded cells to develop and replace damaged nerve tissue ¹².

The impact of cell therapies has been limited to date, due to the inherent complexity of cell proliferation, differentiation, scalability, as well as regulatory barriers ¹⁵, particularly in stem cell research. To replace, repair and regenerate neural tissue specifically; to restore function at the cellular and organ level; the medium must successfully promote endogenous reinnervation and/or seeded neurogenesis. In principle, the greater the accuracy of imitation - the healthier the engineered tissue. Fundamental studies in TE may still rely on investigating development and use of highly accurate tissue models (such as 'Brain-on-a-Chip' devices).

Microtissue construct (MTC) technologies aim to recapitulate the niche microenvironments of native tissue, as well as temporal events that occur during cell development, in order to achieve directed cell maturation and integration. To replace, repair and regenerate neural tissue; as well as to restore network function locally and at the organ level; the medium must successfully promote endogenous reinnervation and vascularisation, in addition to its primary goal of neurogenesis from seeded cells.

1.2.3. Neural Stem Cell Microenvironment

To imitate the microenvironment, it is important to understand the matrix composition, the gradients of trophic factors, and the interplay of different supportive cells. NSCs originate in two specific areas of the brain: the ‘Lateral Ventricle-Subventricular Zone’ (SVZ) and the ‘Dentate Gyrus’ of the hippocampal formation^{20,21}. These regions are surgically inaccessible; to extract brain tissue for NSC isolation requires a highly invasive procedure. This has led to trends in research that focus on more readily available sources of stem cells: mesenchymal stem cells (MSC) and induced pluripotent stem cells. These cell types require a slightly deviated, but analogous, development path to NSC; as they are, by design, a precursor to this cell type.

Adult NSCs are self-renewing, multipotent cells that primarily differentiate into neurons, astrocytes and oligodendrocytes (see Figure 1.1 (C)); signalled via exogenous stimuli from their environment illustrated in Figure 1 (B).

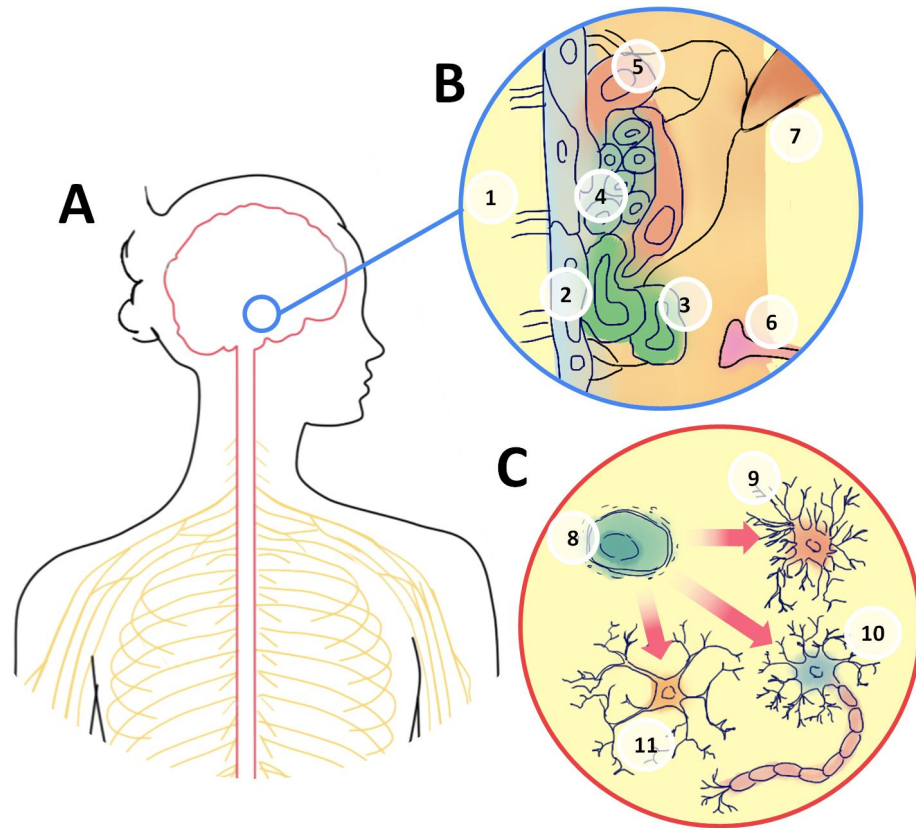


Figure 1.1. Neural Extracellular Matrix (nECM). (A) Illustration of central nervous system (red) and peripheral nervous system (yellow). (B) Cell schematic diagram showing the nECM of the SVZ. Based on illustration in work by Zhao *et al.*³ and Riquelme *et al.*²⁰. (1) lateral ventricle, (2) ependymal cell layer, (3) transit amplifying cells, (4) migrating neuroblasts, (5) GFAP-positive progenitors, (6) neuronal axon terminal, (7) blood vessel with basal laminae projections (black) i.e. fractones. (C) Neural stem cell differentiation products. (8) neuroblast/neural stem cell, (9) oligodendrocyte, (10) neuron, (11) astrocyte.

The NSC Extracellular Matrix (nECM) is the medium in which NSCs cells differentiate. As shown in Figure 1.1 (B), the nECM elements include: (i) the porous hierarchical architectures of the tissue; (ii) cellular components such as supporting neuroglia and descendent/progenitor cells, (iii) acellular elements such as soluble and membrane bound paracrine and endocrine signalling factors, (iv) neural axon signalling and (v) fibrous structures comprised of collagen, fibronectin, elastin, and laminin.

The ependymal layer (see Figure 1.2 (B2)) separates the ventricle from the SVZ tissue ECM, which contains these fibrous structures as ‘fractones’, basal laminae projections from blood

vessels ²². Generally, such fibrous structures are important in tissue and organ regeneration as they provide physical support and adhesion cues, as well as sequester and release paracrine signalling factors. These cues and factors direct NSCs to perform a number of actions: attach or migrate, differentiate, replicate ²³, to remain in a quiescent state, or to commit apoptosis ^{20,24}. Nerve growth factors are termed neurotrophins: a family of proteins that induce the survival, development and function of neurons. During nervous system development, nerve target cells or surrounding glia secrete these factors ^{3,20}. NSCs are affected by other environmental elements; such as growth factor gradients, dynamic forces, and the presence of another cell type ²⁵.

A 3D environment is preferential when culturing cells, as cells as well as nutrients and waste can transfuse more readily. A further benefit of this environment is that fluid can surround the cells in 3D porous medium. This allows a greater degree of interaction and there is more cell surface available. In nerve tissue regeneration, mechanical stress can be more readily displaced in 3D. A cell in a 3D environment has the ability to minimise an impacting force by free migration, whereas in a 2D setting a cell may be pinned and prevented from even planar migration, with fewer degrees of free migration and no recourse ²⁶. ²⁶. In 1997 Weaver *et al.* showed change in cell behaviour between 2D and 3D environments ²⁷, while in 2003 Wolf *et al.* showed tumor cell migration through a 3D collagen matrix ²⁸, both experiments demonstrating the benefits of 3D systems for cell motility.

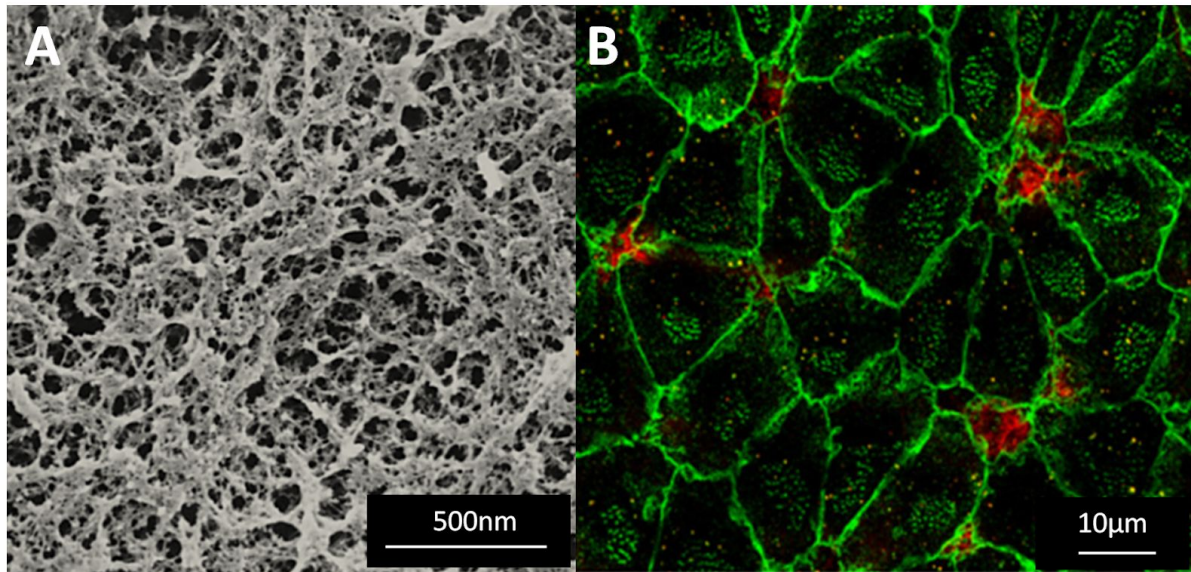


Figure 1.2. ECM protein networks. (A) SEM image of the corneal basement membrane nanostructure. (B) Fluorescent microscopy of ‘Pinwheel’ extracellular neural stem cell niche, with red highlighting the NSC cells ²⁹.

1.2.4. Biomaterial Criteria

TE research most commonly addresses the objective of growing living tissues and organelles by applying one or more of the following techniques: (i) scaffolding, (ii) bioactive encapsulation, (iii) fluid flow or ‘vascularization’, and (iv) electrostimulation. In principle, these combine to cumulatively aid cell survival, differentiation, re-establishing a functional neural network and forming new healthy tissue. To facilitate cell growth and development, a growth environment must:

1. Regulate cell: adhesion, proliferation, migration, and differentiation
2. Facilitate fluid flow; supplying nutrients and removing metabolic wastes
3. Present cells with cues: spatial, temporal, and electrostatic.
4. Present physical properties such as structural guidance of neurite outgrowth.
5. Deter further degeneration and fibrosis.

The criteria for an MTC fall into two broad categories. The first follows the traditional Hippocratic Oath: “First, do no harm”. The second is the promotion of regrowth by fulfilling the objectives described above. To do no harm, an implant must completely succeed by a number of criteria at a minimum. An implant:

- i. Must be chemically inert, not generating a reaction with elements in the system or forming new products.
- ii. Must be non-immunogenic, *i.e.* must not cause irritation provoking an immune system response, for example inflammation. Allowing pathogen growth or biofilm formation in the scaffold would cause a deleterious immune response.
- iii. Must be sterile, as well as sterilisable. Must be free of any pathogens prior to implantation. Sterilization may be achieved by irradiation, or filtration.
- iv. Must be non-thrombogenic, *i.e.* must not cause blood clotting at the implant site. This is particularly important for brain implantation as thrombosis may cause ischemic stroke.
- v. Must be cytocompatible, *i.e.* must not cause cell death or apoptosis. Must not be comprised of toxic elements, to prevent the release of toxic elements upon degradation.
- vi. Must be non-fibrogenic. Fibrosis can envelop irritant material, blocking its potential bioactivity. Nanofiber scaffolds can provoke an immune response, as large surface-area-to volume ratio enables non-specific protein adsorption. Antifouling surface modification can reduce fibrosis.

In the promotion of regrowth, there are several objectives. To be effective:

- i. Implant material must remain robust during implantation time frame.
- ii. Implant mechanical characteristics must mimic the native viscoelastic tissue. In stiffness and deformability. These properties provide inputs into cell behavior ²⁴. A highly stiff scaffold can cause nerve dislocation, while too flexible a scaffold may not support neural regeneration ³⁰. Native brain tissue typically has an elastic modulus of 0.5 - 1 kPa ³¹.
- iii. Minimum swelling characteristics are preferred to prevent chronic nerve compression ³². Swelling of nerve guides constructs can result in nerve compression and impede the outgrowth of regenerating nerves.
- iv. Implant material should degrade completely, and be resorbed in the body, once tissue regrowth is complete. This allows cellular infiltration and full tissue recovery. Anisotropic tissues such as tendon, ligament or nerves, take a longer time to heal due to low cell density and limited vasculature ³³. Degradation is led by enzymes,

microorganisms, as well as abiotic reactions like hydrolysis and oxidation ³⁴. Homogeneous degradation of the material means mechanical stability will be maintained for the greatest possible time. An inhomogeneous cell distribution results in irregular scaffold biodegradation. Maintaining the porosity of scaffolds promotes effective cell distribution by migration ³⁵.

- v. Implant material should be hydrophilic. Poor hydrophilicity leads to low cell adhesion and proliferation. A hydrophilic molecule or part of a molecule is typically charge polarized and capable of hydrogen bonding.

These objectives narrow the viable materials that can match native tissue. Hydrophilic polymer networks, or hydrogels, have proven to be the most viable, covering the majority of the objectives inherently. With advanced fabrication methods, hydrogels can be tailored to imitate the mechanical properties and biochemical motifs of native tissues.

1.2.5. Fiber Hydrogel Composites

Hydrogels are crosslinked networks of hydrophilic polymers that can swell in water to capture many times their original mass ³⁶. Hydrogels can act as a matrix support structure for incorporating fibrous scaffolding. Physical and biochemical properties of hydrogels largely depend on their compositions, methods used for their polymerization, and their crosslinking density. Hydrogels are classified:

- i. Permanent gel: covalently cross-linked networks, replacing hydrogen bonds by stronger and stable covalent bonds.
- ii. Reversible gel: cohesive networks of molecular entanglements, as well as cohesive forces including ionic, hydrogen bonding, or hydrophobic effects. This cohesion is reversible, and can be reversed by stress.

Hydrogels for biomedical applications are designed to resemble the characteristics of native ECM and to provide 3D scaffolds for cellular growth and tissue formation. Common Hydrogels used for this purpose include: methylcellulose (MC), hyaluronic acid (HA), and agarose hydrogels ⁶. Hydrogels are highly investigated materials for NTE due to a number of advantageous qualities; tissue-like mechanical properties, conformable to soft neural tissue. Its porous structure allows cell infiltration and axon outgrowth, as well as excellent nutrient

and oxygen permeability¹⁸. The inner structure has a high surface area attach adhesion and/or growth-promoting molecular cues or incorporate drug or other bioactive materials. Hydrogel's ability to gel in situ allows for minimally invasive surgical implantation and effective application as the gel conformally fills irregular cavities created in lesion excision⁶.

Cell migration in hydrogels is often poor due to weak mechanical structure, and neurons do not extend their neurites through these three-dimensional matrices efficiently^{30,37,38} and so researchers have affected the mechanical properties of hydrogels through a number of means, including fiber encapsulation³⁹⁻⁴⁴ and chemical/process modification to increase crosslinking density⁴⁵. The encapsulation of fibers has the added benefit of presenting structural motifs shown to affect cell behaviour⁴⁶ and guidance⁴⁷⁻⁵⁰, improving cell viability^{30,37,38}.

A design objective in TE is the generation of three-dimensional scaffolds that can mimic the nanofibrous structure of the nECM fibers to enable the guidance of cellular migration, provide mechanical support, and regulate cellular activities⁵¹. Cells are capable of sensing individual polymer fibers with diameters as low as several nanometers⁴⁶, while sub-micron diameter fibers have exhibited improved cytocompatibility^{30,37}. Kijenska *et al.* showed that smaller diameter fibers (327 nm) are more compatible towards the nerve cells, compared to nanofibers with higher fiber diameter (746 nm)³⁰, while Yang *et al.* showed that NSC differentiation rate was higher for nanofibers (700 nm) than for microfibers (3.5 μ m)³⁷.

These studies demonstrate the advantages of ultrafine fibers in cell viability and behavioural studies; and, as such, nanofabrication continues to be investigated in TE in an extensive number of studies.

1.3. Nanofiber Fabrication Techniques

Nanofibers have a high surface area to volume ratio, are anisotropic, are less agglomerative than nanoparticles and can modify bulk material properties when part of a multilayer fibrous assembly. There exist a large number of nanofabrication tools and techniques capable of producing nanofibrous structures, see table 1.1. Each of these has their respective abilities and limitations with regards to: scalability; material versatility; speed; fiber morphology and dimension; ease of use; and efficiency.

For example, the self-assembly technique has the benefits of easy incorporation of cells during peptide nanofiber formation, generating a 3D porous assembly; and can be injected, assembling *in vivo* ⁵². *In vivo* forming materials, naturally conform to the void space left after surgical excision of damaged tissue. Gelain *et al.* produced nanoscale scaffolds from self-assembled peptides combined with polyesters: Poly(lactic acid) (PLA) and poly(lactic-co-glycolic acid) (PLGA); and applied this to a rat spinal cord injury model ⁵³. However, self-assembly is hindered by its complex procedure, lack of fiber arrangement control, and limited fiber diameter (~2-30 nm) and length (~10 μm) ⁴⁶.

Of the existing nanofabrication techniques, electrospinning is counted as one of the most popular due to its simple setup, material versatility, and its ability to deposit *in situ* at room temperature and pressure (RTP) using a wide variety of setup variations. In the following section we discuss this technique, its process parameters, conventional setup variations, and a proposed advanced technique which aims to produce nanofibrous assemblies for TE.

Table 1.1. Established nanofiber production methods.

Method	Description	Advantages	Disadvantages
Drawing	A polymer solution droplet is contacted with a sharp tip and then drawn to a second position. The fiber solidifies after solvent evaporation.	Simple process	Limited to viscoelastic material, discontinuous process
Electrospinning	Nanofibers are ejected from a viscoelastic solution of a polymer or melt from a tip under high potential bias. ⁵⁴⁻⁵⁶	Unlimited fiber length, simple setup, diverse polymers and solvents used, single-step	High voltage, solvents required, numerous parameters affecting the process
Force-spinning (centrifugal)	High concentration polymer solution or melt under applied centrifugal force. ⁵⁷	Simple, high production yield	Submicron diameter fibers difficult
Interfacial polymerisation	High local concentrations of both monomers and dopant anions at the liquid interface of two immiscible solutions promote the formation of monomer-anion aggregates which further act as nucleation sites for polymerisation. ^{58,59}	Simple equipment	Poor control over nanofiber morphology
Melt blowing	Polymer melt extruded under hot air force through a die, and drawn to a collector. ^{60,61}	Simple, single-step, fiber diameter control, no solvents	Thermal degradation limited to melt high viscosity
Phase separation	A gel is formed by cooling a polymer solution to its gelation temperature. The gel is immersed in distilled water for solvent exchange, and then lyophilised, resulting in nano-porous foam structure. ⁶²	Simple process	Numerous parameters, limited to a few polymers, slow process
Self-assembly	Amphiphilic molecules are used as basic building blocks that self-assemble to produce nanofibers. ^{50,63,64}	Produces very thin nanofibers	Poor control over morphology and orientation, time consuming
Template melt extrusion	Molten polymer is forced through a nanoporous Anodic aluminium oxide (AAO) membrane and cooled to solidify. ⁶⁵	No solvents, homogenous fiber diameter	Short length of fibers, time consuming
Template Synthesis	Nanofibers, of solid or hollow shape, are formed within numerous cylindrical pores of an AAO membrane by oxidative polymerisation, electrochemically or chemically. ⁶⁶	Aligned nanofibers, homogenous and easily controlled fiber diameter	Complex method, cannot make continuous fiber

1.4. Electrospinning

The charged jet, in Electrospinning (ES), experiences several forces that influence the jetting velocity and instability: electrostatic force, drag force, gravitational force, coulombic repulsion force, surface tension, and viscoelastic force. By understanding the forces and the parameters that affect them, electrospun fiber morphology, diameter, and orientation may be controlled. In the following section we discuss the electrospinning technique, its theoretical background, and its parameters.

1.4.1. Introduction to Electrospinning

ES is an electrostatic drawing technique that forms ultrafine polymer fibers from a polymer solution or melt. Polymeric solution is fed to a metallic capillary tip, forming a sessile or pendant droplet at the outlet. A high potential bias is applied between the capillary tip and a distant grounded electrode, which has a collecting substrate on its surface. As the potential is increased, electrostatic charge builds within the solution and the electric field intensity increases. Electric tensile force, due to the electric field, causes a typical ‘Taylor Cone’ elongation of the charged solution droplet.

As the potential is increased beyond a threshold intensity, the electrostatic tensile force overcomes both the droplet surface tension and cohesive resistance, and solution is drawn from the cone tip to the electrode, in an ultrafine jet. As the jet is stretched, its diameter and surface area are reduced, leading to reduced interfacial vapour pressure ⁶⁷. Pronounced solvent evaporation causes an increase in viscosity, solidifying the jet. Fiber is continuously deposited on the collector substrate from the jet. In conventional, or ‘far-field’, electrospinning (FFES), tip-to-collector interspacing can range from ten centimetres, to hundreds of centimetres; with voltage ranging from 10-30 kV ⁶⁸, (Figure 1.3 (A))

During transit, the jet experiences electrically and environmentally driven bending instabilities, which cause a whipping motion in the stream. The whipping produces a randomly oriented, fibrous mat at the collector (Figure 1.3 (B)). Point charges cannot be maintained in a static equilibrium in the absence of external force, by the principles of

Earnshaw's theorem ⁶⁹. By this theoretical principle, instability is primarily caused by the electrostatic interactions between the external electric field and the surface charges on the jet ⁵⁶; and with greater surface area, more charges are exposed leading to a more pronounced instability effect ⁷⁰.

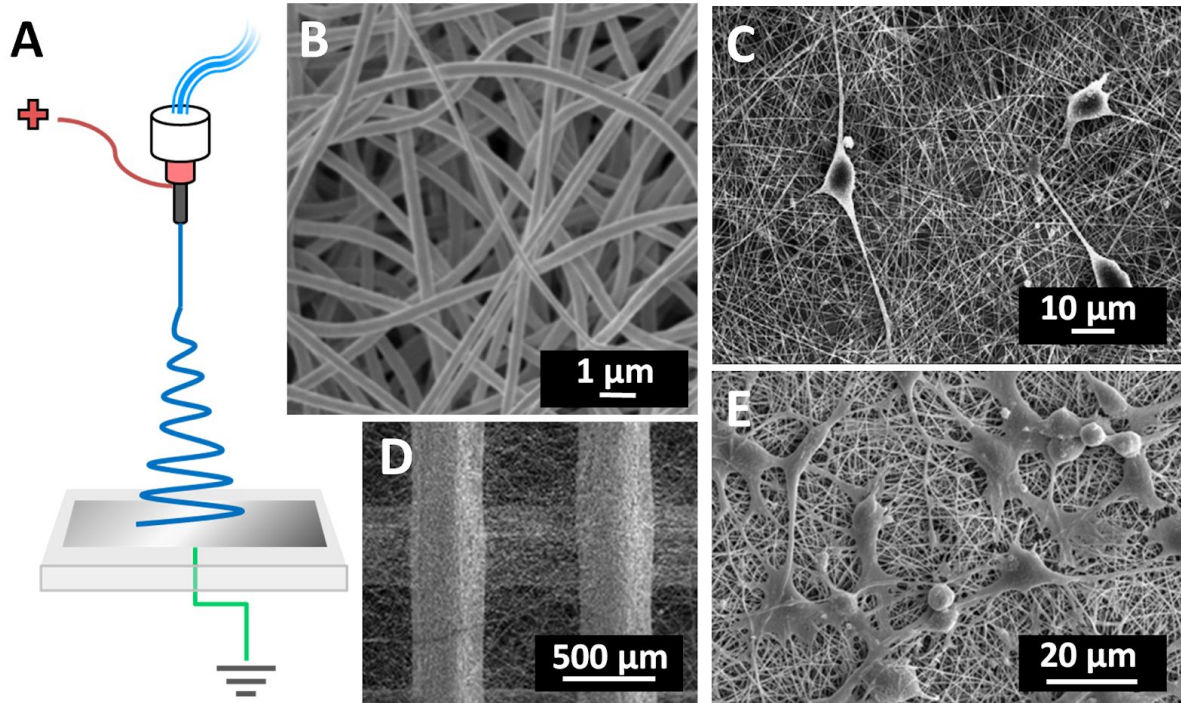


Figure 1.3. Far-Field Electrospinning (FFES). (A) Diagram showing FFES whipping jet emanation from emitter tip which is positively bias charged with grounded collecting plate below. (B) SEM image of FFES electrospun PEO fibrous mesh. (C) ES spun fibrous mesh with neural stem cells ³⁸. (D) ES spun fibers on the surface of an extrusion printed PCL lattice structure ⁷¹. (E) Schwann cells on the surface of ES spun fibers ³⁰.

ES originates from the analogous electrospraying process, discovered in the 17th century, which applies electric field to draw a spray of micro-droplets from polymer solution. ES was formally discovered at the end of the 19th century by Baron Rayleigh, and throughout the 20th century various theoretical models and applications have since been developed (see Figure 1.4). For a full breakdown of major individual contributions to ES theory please refer to table 1.5. TE has a long history of applying electrospun scaffolds: In 1978 Annis and Bornat published work examining electrospun polyurethane mats for use as vascular prosthetics. In 1985 Fisher and Annis examined the long-term in vivo performance of an electrospun arterial

prosthesis. These pioneering studies using ES scaffolds would not see further development until a decade later, when ES found widespread popularity for its applications in TE and drug delivery.

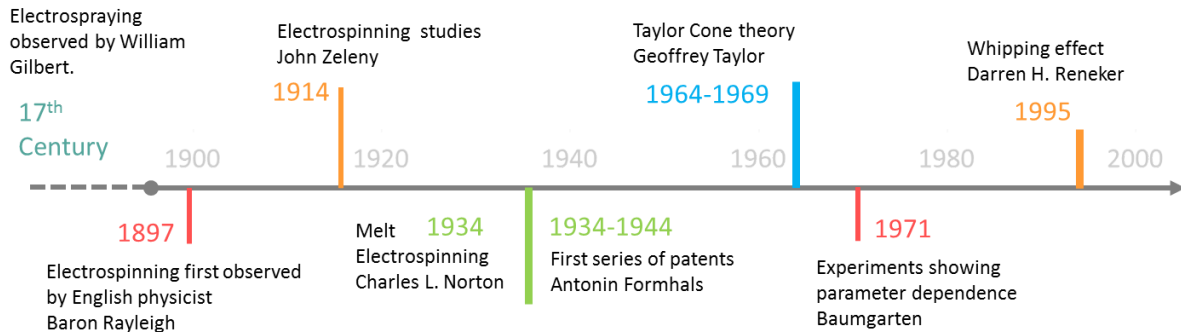


Figure 1.4. Timeline of electrospinning history.

FFES has been applied in many studies to create nanofibrous mats/meshes to mimic the ECM of native tissues. In 2005, PLA and PLGA scaffolds for heart tissue constructs were developed by Zong *et al.*⁷² testing with cardiomyocytes, which were found to prefer hydrophobic surfaces. Yang *et al.*³⁸ grew neural stem cells on the surface of a PLA nanofibrous mesh (Figure 1.3(C)), finding increased surface roughness promoted cell adhesion. In 2008, Park *et al.* combined direct polymer melt grids with FFES PCL/Collagen nanofibers interstitially placed to create hybrid scaffolds (Figure 1.3 (D))⁷¹, however by using HFIP, it is likely that the collagen was denatured in the solution preparation. Kijeńska *et al.*³⁰ (2013) grew schwann cells, a peripheral nervous system cell type, on more complex core-shell PCL–laminin scaffolds (Figure 1.3 (E)).

To control the ES process, input factors are rigorously controlled to generate desired outputs of fiber morphology, diameter and orientation. In the following section we discuss electrospinning parameters and theoretical principles by which parameter variation can be understood in their effects. Further to this, topics and theoretical phenomena that are not explicitly discussed in further chapters, which nevertheless influenced decisions of experimental and solution design, are also discussed.

1.4.2. Solution Parameters

1.4.2.1. Solvent

In order to develop solutions for ES, we must consider the miscibility parameters of the material, to choose appropriate solvents. For non-polar materials, without hydrogen bonding, the difference between solvent and solute ‘Hildebrand solubility parameter (δ)’ indicates the miscibility of the solution. The parameter is defined as the square root of the cohesive energy density in Eq. 1:

$$\delta = \sqrt{\frac{\Delta H_v - RT}{V_m}} \quad (1)$$

Where ΔH_v is the heat of vaporisation, V_m is the molar volume and δ has units of $(\text{cal}/\text{cm}^3)^{1/2}$. Using reference tables; values of δ can be compared, with greater disparity indicating a less miscible combination.

For polar materials, Hansen solubility parameters are used. These three-dimensional coordinate parameters in Hansen space are:

- i. δ_d The energy from dispersion forces between molecules
- ii. δ_p The energy from dipolar intermolecular force between molecules
- iii. δ_h The energy from hydrogen bonds between molecules.

Combining the parameters in Eq. 2, we can provide the ratio Eq. 3:

$$(Ra)^2 = 4(\delta_{d2} - \delta_{d1})^2 + (\delta_{p2} - \delta_{p1})^2 + (\delta_{h2} - \delta_{h1})^2 \quad (2)$$

$$\frac{Ra}{Ro} = RED \quad (3)$$

Where Ra is the distance between coordinate parameters, Ro is the interaction radius and the ‘relative energy difference’ (RED) value indicates the miscibility, where: $RED < 1$ soluble; $RED \sim 1$ partially soluble; $RED > 1$ insoluble.

Binary solvent systems are regularly used in ES, as effective spinning solvents are highly volatile and often require a stabilising solvent. In the case of highly volatile chloroform, DMF is often added, stabilising the solution, reducing the evaporation rate, and preventing clogging issues at the capillary outlet. Binary systems can drastically reduce the diameter of fibers produced. For example, Van der Schueren *et al.* showed fibers more than ten times smaller can be achieved by using a binary rather than a single solvent system ⁷³.

Evaporation rate based on volatility is important for ES, as mentioned, due to the destabilising effect of drying at the outlet. Solution vapour pressure indicates the volatility of the solution and solvent evaporation rate. The vapour pressure of binary solvent mixtures can be approximated using reference tables and Raoult's law using Eq. 4 and Eq. 5:

$$p = p_A x_A + p_B x_B \quad (4)$$

$$p = p_A (1 - x_B) + p_B x_B \quad (5)$$

Where p is the total vapour pressure, p_A and p_B are the vapour pressures of the individual components, and x is the molar fraction of the respective components (identified A and B). The balance of volatility is important to manage in ES, as it can affect fiber morphology and distribution: A more rapidly evaporating solvent can cause pore formation, while a slowly evaporating solvent can leave fibers still solvated on the substrate, resulting in collapsed and fused fibers.

1.4.2.2. Solute

ES can be applied to almost any material that can flow; uptake charge; maintain cohesivity during jetting, and readily solidify. Synthetic and natural polymers, as well as polymer alloys and composites, can be electrospun; given necessary conditions are met. However, the ES process can detrimentally affect some materials, degrading polymer chains and sensitive motifs in some cases ⁷⁴. Polymers are categorised based on origin (natural | artificial), on physical properties (thermoplastics | thermosets | non-Newtonian | conductive), and on composition (monomer | copolymer | molecular weight | crystallinity).

To represent mass distribution for a given sample of polymer, we use the average molecular mass, or Number Average (M_n) (Eq. 6):

$$M_n = \frac{\sum M_i N_i}{\sum N_i} \quad (6)$$

The M_n of the polymer influences the fiber morphology: High M_n results in a large fiber diameter whereas a much lower M_n results in pores and beading. Polymer molecular weight and distribution can also determine the rate of degradation: the greater the chain length, the more bonds, and therefore the more extended the period of degradation. Given that M_n is polydisperse in most cases, the viscosity of the solution is a more reliable solution-to-solution comparative parameter in ES.

Viscosity (η) is a proportionality factor of resistance to shearing flow, with units of **poise** ($\text{1g.cm}^{-1}.\text{s}^{-1}$). This is defined by a system based relation: Two plates, separated by a fluid, move parallel in relation to one another generating viscoelastic resistance to shear, force F shown in Eq. 7:

$$F = \eta \cdot A \frac{u}{y} \quad (7)$$

Where η is the dynamic viscosity of the fluid, u is the relative speed, y is the separation, and A is the area. Viscosity is a means of differentiating solutions, given that the molecular weight of raw polymer material can have large polydispersity. In ES, 1–20 poise is a reasonable viscosity range to use for Poly(ethylene oxide) (PEO), for example.

Polymer solution viscosity is primarily caused by the friction of entangled polymer chains. The variation of viscosity with polymer concentration depends on the nature of the polymer and solvent. Viscosity can be defined in terms of the specific viscosity (Eq. 8), the reduced specific viscosity (Eq. 9) and relative viscosity (Eq. 10). These are defined:

$$\eta_{sp} = (\eta - \eta_s)/\eta_s \quad (8)$$

$$\eta_{red} = ((\eta/\eta_s) - 1)/c \quad (9)$$

$$\eta_{rel} = \eta/\eta_s \quad (10)$$

Where η is the solution viscosity, η_s is the solvent viscosity and c is the polymer concentration (g/ml).

The viscosity of a polymeric solution significantly affects fiber diameter, morphology, as well as the spinnability of the solution. If the viscosity is too low (e.g. under one poise for PEO), the emanating jet experiences varicose instabilities, intermittently forming droplets, resulting in beaded fiber morphologies ⁷⁵. Micropores and beaded structures are less likely to form if the viscosity of the solution is above this lower limit, however if the viscosity is too high (e.g. above 20 poise for PEO), then ES is prohibited due to flow instabilities; caused by the high viscoelastic cohesiveness of the solution ⁷⁶.

Solute concentration influences solution properties of viscosity, surface tension, and conductivity; all of which affect fiber diameter and morphology ⁵⁰. Whether a fiber can remain cohesive during jetting transit is determined by solute concentration. Concentration is commonly measured in w/w% (i.e. wt%), v/v%, and w/v; but not mol.L⁻¹, as polymer M_n is commonly polydisperse. Polymer entanglement depends on solution concentration and when polymer entanglement is high the jet is stabilized, and more force is required to deform the viscoelastic solution.

Chain entanglement determines the viscosity of a polymer solution. Dilution affects this, as for highly dilute polymer solutions the molecular overlap is low. At a minimum critical concentration the molecules begin to overlap. In ES this region typically produces bead-on-string effects. The entanglement can be quantified using the entanglement number n_e , which is given by Eq. 11:

$$(n_e)_{soln} = \frac{M_w}{(M_e)_{soln}} = \frac{(\phi_p M_w)}{M_e} \quad (11)$$

Where M_w is the molecular weight, M_e is the solution entanglement molecular weight, and ϕ_p is the polymer volume fraction.

Viscoelastic cohesivity and viscosity are functions of polymer chain entanglement intensity, which itself is a function of polymer concentration. Entanglement is important in ES as it maintains a cohesive, viscous jet stream and for some systems this becomes an issue. For example, when electrospinning Liquid crystalline graphene oxide (LCGO), the planar graphene sheets fail to entangle, slipping in parallel planes, and so the bulk solution acts as a shear thinning fluid, disallowing stable ES jet formation. This issue may be overcome by adding an assisting polymer to stabilise the jet during spinning, and once spinning is complete this polymer can be removed from the final product.

Surface tension (γ), units of N.m^{-1} , is the liquid surface tendency to minimise surface area due to cohesive intermolecular attractive forces, which are approximately inversely proportional to temperature. Reducing the surface tension of a solution lowers the threshold voltage, that enables electrospinning to occur, as well as eliminating beading effects. This makes surfactants useful additives for ES solutions ^{77,78}, as they reduce the surface tension via the Marangoni effect ⁷⁹. Surfactants, in water for example, can reduce the surface tension by a factor of three or more.

In ES, copolymer systems are often chosen as a means of stabilising a polymer which has proven difficult to spin alone. Many proteins, which are notoriously difficult to spin, are given assisting copolymers to allow electrospinning. Some copolymers systems are designed to present a specific degradation profile, e.g. aliphatic polyesters are blended in order to achieve a certain time-frame of degradation.

1.4.2.3. Synthetic Polymers

Synthetic materials may have advantages over biopolymers, as the synthetic polymers are chemically synthesized and processed, they are relatively free of pathogens and contaminants. Additionally they can be tuned to control the degradability timeframe, degrading into bioresorbable monomers, freeing space for regenerating or infiltrating nerve tissue ⁸⁰. Table

1.2 shows a list of polymer Aliphatic polyesters such as PLA, PCL and PGA are the most commonly used synthetic polymers for NTE applications as they can be tuned to hydrolytically degrade based on crystallinity and copolymer ratio. The hydrolysis of aliphatic polyesters is initiated by water absorption, followed by hydrolytic breaking of ester bonds.

The degree of crystallinity affects the rate of degradation as the crystal segments hinder water transfection through the medium ³⁴. PLA and PLGA produce lactic acid as a degradation product which may adversely influence axonal growth and nerve function, according to Chang *et al.* ⁸¹, despite lactic acid being relatively benign in the body as it is readily metabolised.

Synthetic polymers have a few disadvantages in NTE application. Pure synthetic fibers could support nerve cell growth and proliferation, but the capability is limited, as synthetic polymers are often hydrophobic and lack recognition sites, both of which impede cell attachment ³⁰. Implantable materials are compared and categorised according to their respective strengths. They also present limited surface bioactive elements necessary for cell signalling to promote cell development. Due to these inherent limitations, there is a trend towards producing bio-synthetic materials by combining nECM molecules with biodegradable synthetic polymers, combining the advantages of both.

Table 1.2. Synthetic electrospinning materials for biofabrication.

Name	Acronym	Application	References.
Carbon (Copolymer PAN)	C	Tissue Engineering	82
Poly(l-lactide-co- ϵ -caprolactone)	P(LLA-CL)	Tissue Engineering	83,84
Polyacrylonitrile	PAN	Ultrafiltration	85,86
Polyaniline	PANI	Conductive	87
Poly(ϵ -caprolactone)	PCL	Tissue Engineering	88–90
Poly(ϵ -caprolactone-co-ethyl ethylene phosphate)	PCLEEP	Tissue Engineering	91
Poly(3,4-ethylenedioxythiophene)	PEDOT	Conductive	92,93
Poly(ethylene oxide)	PEO	Vector for Biomaterial	94–96
Poly(ethylene terephthalate)	PET	Tissue Engineering	97,98
Poly(ethylene-co-vinyl acetate)	PEVA	Tissue Engineering	99
Poly(glycolide)	PGA	Tissue Engineering	86
Poly(lactic acid) / Poly(lactide)	PLA	Tissue Engineering	37,38
PLA-poly(ethylene glycol)	PLA-PEG	Tissue Engineering	100
Poly(lactic-co-glycolic acid)	PLGA	Tissue Engineering	100–104
Polypyrrole	Ppy	Conductive	105
Polyurethane	PU	Drug Release	106,107

1.4.2.4. Electrical Properties

The electrical properties of ES solutions heavily influence the outcomes of spinning, particularly influencing the force of the jet. Low conductivity solutions cannot be spun due to the lack of surface charges on the fluid droplet, while very high conductivity solutions cannot be spun, as there is a reduction in the tangential electric field on the surface of the fluid droplet, prohibiting Taylor cone formation ¹⁰⁸.

Fiber morphology has been shown to be affected by changing solution conductivity. The jet experiences increased force due to higher charge concentration in solution. Addition of ionic salt to the solution led to the reduction of fiber diameter in FFES electrospinning by Zong *et al.* (2002) ⁸⁶. The increase in charge density also exacerbates the whipping instabilities of FFES resulting in longer jet paths, reduced fiber diameter and expanding the depositional area. Increasing the conductivity of their solutions Xue *et al.* (2014) ¹⁰⁹ showed NFES outcome change from beaded to straight to curling fibers, implicating an increase in jet velocity.

Electrolytic conductivity (σ) of a solution depends on electrolyte concentration, and is measured in S.m^{-1} . High conductivity solutions have a greater charge carrying capacity. Injected charge, in combination with electric field, dictates the electrostatic force the solution experiences ¹¹⁰ and thus the velocity of the exiting jet. Increasing this force generates lower diameter fibers; however, under enough force, the jet cohesivity can breakdown, resulting in electrospraying ¹¹¹. Ionic mobility (μ), units of $\text{m}^2.\text{V}^{-1}.\text{s}^{-1}$, dictates the charge motion in the polymer by Eq. 12:

$$\mu = \frac{v_d}{E_\infty} \quad (12)$$

Where v_d is the drift velocity (units of m.s^{-1}), and E_∞ is the electric field intensity. The limiting molar ionic conductivity (λ) is defined by Eq. 13 and Eq. 14 defines the total electrolyte ionic conductivity:

$$\lambda = z\mu F \quad (13)$$

$$\Lambda_m^\circ = \sum_i n_i \lambda_i \quad (14)$$

Where n is the number of ions in the formula of the electrolyte, z is the ionic charge and F is the Faraday constant. When an ion is moving at a constant drift velocity v_c , two forces are in opposing equilibrium: an electrical force (F_{el}) (Eq. 15), and a frictional force (F_{drag}) defined by Eq. 16:

$$F_{el} = zeE_\infty \quad (15)$$

$$F_{drag} = (6\pi\eta a) \cdot v_c \quad (16)$$

Where ze represents ionic charge in integer multiples of electron charge, ' a ' is the Stokes Radius of the ion, and η is the solution viscosity. The ion mobility is inversely proportional to the friction coefficient, described by Eq. 17:

$$\mu = \frac{ze}{f} = \frac{ze}{6\pi\eta a} \quad (17)$$

Where the Stokes radius (a), is related to the temperature and the diffusion coefficient D via the Einstein relation (Eq. 18):

$$a = \frac{k_B T}{6\pi\eta D} \quad (18)$$

As a further complication to electrolytic conductivity, there are some situations in which the solvent chemistry can directly affect the conductivity. For example, H^+ ions have higher conductivity in alcohols, compared to other ions, due to alcohols' hydroxyl group, whereas, in other solvents, H^+ ions behave normally.

The above relations connect the conductivity of a solution to: solute concentration, solvent properties, its ionic concentration and the ambient temperature. This has profound ramifications for ES, as any parameter that is uncontrolled, in a parametric study, will

produce noise in the output, possibly disabling output altogether. This necessitates the strict control of this wide array of parameters for such studies.

1.4.3. Process Parameters

1.4.3.1. Electric Field

In ES, a positive or negative bias potential is applied to a conductive capillary tip electrode relative to a grounded electrode collector (or the system is reversed), creating a voltage and an intense local electric field in the space between the electrodes. The electric field (E_{∞}) is approximated as static and uniform for convenience, as described in Eq. 19:

$$E_{\infty} = V . d \quad (19)$$

Where d is the tip-to-collector interspacing. This is an approximation because of the boundary effects of both electrodes, as well as the negligible contribution of charge motion in the jet. When a bias is applied to a polymeric solution, mutual charge repulsion generates charge on the droplet surface and an induced force is felt by the surface in the presence of the external field. Taylor calculated the threshold voltage (V_c) of a suspended hemispherical conducting drop in air (Eq. 20):

$$V_c = \sqrt{\frac{\gamma . d^2}{\epsilon_0 . r}} \quad (20)$$

Where r is the radius of the cone, γ is the surface tension of the polymeric solution. The interspacing between the emitting tip and the collecting electrode affects the electric field shape and intensity, as well as the jet travel time (t_j) (Eq. 21):

$$t_j = \frac{d}{v_j} \quad (21)$$

Where v_j is the jet velocity. Jet travel time affects the fiber diameter and residual solvent in the fiber.

In the event of electric field intensity exceeding material dielectric strength, dielectric breakdown occurs; with a sudden reduction in the electrical resistance. The dielectric becomes electrically conductive with an associated plasma ion arc discharge. The specific breakdown mechanisms are distinct between material phases. In gases, regions of local, intense electric field partially ionize the gas particles, and thermionic and electrons conduct through the medium to the ground, generating a current.

Breakdown voltage in air was first approximated by Paschen ¹¹². Arcing voltage is proportional to electrode interspacing and gas pressure, down to a certain point of low interspacing, where the relation becomes inversely proportional. In an electrical field of *c.a.* 3 kV/mm, air begins to break down. Its exact value varies with the shape and size of the electrodes, and increases with ambient pressure. In ES, breakdown relies on: dielectric material and density (i.e. gas pressure); electrode material, geometry and interspacing; and electric field intensity.

1.4.3.2. Flow Rate

Flow rate in ES is controlled in order to adequately maintain droplet size at the capillary outlet. With highly volatile solvents, a higher throughput is necessary in order to prevent clogging due to rapid solvent evaporation and solidification of polymer at the tip. Increased electric field may be applied to remove the solution more rapidly and, in order to maintain the droplet radius, higher flow rates are used to supply material at an equal rate of loss. Typical methods used to feed solution from a reservoir to the tip include: syringe pumps, gravitational force and pressurised gas, with syringe pumps arguably having the greatest accuracy and control.

1.4.3.3. Capillary Tip

Tip design can be classed: ‘single channel’ or ‘coaxial channel’. Single channel tips produce uniform fibers whose diameter is proportional to the inner diameter of the tip. When using a coaxial tip, two polymeric solutions are simultaneously spun; one forming the core, the other enveloping as a sheath ¹¹³. This method is particularly useful in bioencapsulation;

biopolymers in general are denatured by volatile spinning solvents. It is difficult to electrospin using water as a solvent as it has a high surface tension and evaporates rapidly. This issue can be resolved by coaxially spinning using a readily spinnable, volatile solvent solution as a sheath over an aqueous biopolymer solution ³⁰. Jayasinghe *et al.* ^{114,115}, demonstrated electrospinning of living cells through the use of coaxial tip, forming scaffolds of smooth muscle cells in Polydimethylsiloxane (PDMS).

1.4.3.4. Collector Configuration

In ES, the grounded collector electrode commonly has a thin collecting surface (tin foil, paper or glass) on the surface of the electrode. The geometry and material of the electrodes influence the shape of the electric field, and by relative motion can control fiber orientation ¹¹⁶. Geometries of ES collectors can be classed: linear, planar, or three-dimensional; with planar being the most common choice as it is the most straightforward. Translational and rotational collectors are often used to achieve fiber alignment. As the fibers emanate from the tip, the high speed stage motion mechanically draws the fibers in the direction of motion.

Translational and rotational collectors are often used to achieve fiber alignment. As the fibers emanate from the tip, the high speed stage motion mechanically draws the fibers in the direction of motion, achieving alignment. The most straightforward electrospinning method for collecting aligned fibers is through the use of a high speed rotating mandrel or drum ^{117–119}. This allows fibers to be collected over a relatively large area. Theron *et al.* produced overlapping alignment of electrospun nanofibers on the surface of a sharpened rotating disc ¹²⁰. Mechanical drawing force increases proportionally to the rotational velocity of the collecting surface. The greater the total drawing force, the smaller the diameter of fibers produced. At extremes of drawing force for a given material, jet cohesivity can breakdown in transit ¹²¹, and so an ideal working speed is constrained below this critical value.

The choice of electrode material can affect both the fiber orientation and morphology. An electrically conductive collector dissipates electric charges and reduces the repulsion among fibers, thus favouring a tightly packed and thick membrane structure. Liu and Hsieh ⁷⁶ found that both the conductivity and the porosity of the collector play an important role in determining the packing density of the collected fiber. Fibers collected on paper showed

smooth surfaces, with few defects. Fibers collected on water were more densely packed and had a greater range of diameter distribution. On a nonconductive collector, the presence of surface electrostatic charges causes fibers to repel each other, giving a more loosely packed fibrous network.

Presence of residual charges on a planar collector can deflect the electrospinning jet away from the intended path to the collector. The charged jet may also be attracted or deflected by surrounding objects. The loss of fiber material may be significantly high, particularly for mass production. Secondary electrodes were employed by Viswanadam *et al.* (2013)¹²² to focus the ES jet, improving yield from 23% to 87%. Kessick *et al.* utilised AC without auxiliary electrodes to reduce whipping instabilities and thus achieve improved precision¹²³.

1.4.3.5. Ambient Conditions

The ambient environment affects many ES processes and impacts fiber morphology substantially. Conditions include: Relative Humidity (RH); air speed; vibration; atmospheric composition; temperature; and pressure.

RH affects the fiber morphology based on the solution properties¹²⁴. In the case of hydrophobic polymers dissolved in organic solvent: the jet forms a thin dry surface due to solvent evaporation. At high humidity, the water in the air acts as a non-solvent preventing solvent from evaporating over the entire surface area, and pores form to allow the diffusion of solvent. In the case of aqueous polymer solutions: at low humidity, aqueous solvent evaporation is more rapid, and the fiber solidifies earlier, experiencing stretching for less time, resulting in thicker fibers. With increasing humidity, fibers are first thinner, then form beads, and finally remain film-like on the surface due to the lack of solvent evaporation.

Air convection in the atmosphere will apply impinging forces on the fiber. The higher the interspacing distance, the greater the surface area presented to be impacted upon. Gas-jet electrospinning uses a spinning tip surrounded by a circular tube which feeds gas in a stream parallel to the solution jet, to both control its stability and impart additional drawing forces

¹²⁵.

Environmental originating vibrations are particularly difficult to control in NFES, where the effects are more visible. The stage must act to suppress external and stage translation associated vibration. This can be achieved by the combination of setup isolation, reinforcement of the stage base, and the application of engineering principles, material and design, to minimize force transmittance.

As the fiber jet travels through the atmosphere toward the collector, a phase separation/evaporation occurs before the solid polymer fibers are deposited. This phase separation can be vapour-induced, which occurs when non-solvent from the vapour phase penetrates the polymer solution. However, transport of the non-solvent into the polymer solution is limited by the slow diffusion of the non-solvent at the fiber surface. For very volatile solvents, the near-surface area can be saturated with evaporating solvent in the vapour phase, which further limits the penetration of non-solvent. This can hinder surface solidification leading to the development of a porous surface morphology, where solvent concentrates at local pore points, evaporating after the main fiber has formed.

Temperature affects the solvent evaporation rate and solution viscosity, where higher temperatures result in thicker fibers due to increased evaporation, leading to early solidification and less drawing. The solvent boiling point is the temperature at which the vapour pressure of the liquid equals the pressure surrounding the liquid. Boiling point temperature is dependent on the surrounding environmental pressure. As mentioned, the dielectric breakdown is related to the pressure of the dielectric medium, gas in the case of ES.

1.5. Near Field Electrospinning

1.5.1. Limitations of FFES

FFES has a simple set-up, operates at room temperature, producing continuous fibers with controllable diameter, using a wide range of materials. However, FFES has a number of drawbacks. Fiber morphology, in FFES, is easily destabilised by process parameters, some of which require stringent control (e.g. humidity, temperature). This is problematic, as surface morphology can influence cell attachment: e.g. increasing the surface roughness promotes attachment and proliferation of nerve cells¹²⁶. Volatile solvents used in ES leads to the denaturation of many biopolymers, limiting the range of processable materials, however there are options to address this as mentioned (Coaxial spinning, aqueous solution). With instability issues, as well as potential clogging issues of solution ES, the process becomes difficult to upscale for mass-production^{126,127}.

The high surface area to volume ratio of nanofibers, combined with typically microporous structure, favours cell adhesion, proliferation, migration, and differentiation. Because of these qualities, FFES has been pursued to produce scaffolds specifically for NTE^{128,129} as well as for other tissue engineering applications^{40,51,130–132}. However, FFES is limited in a number of ways, affecting its applicability to NTE. FFES produces nonwoven random or aligned mats due to the inherent whipping instability of the jet. This hinders its ability to control bulk porosity; the random layering of nanofibers produces bulk pore sizes too low for cell infiltration. Randomly deposited fibers require a minimum diameter of 4 μm to generate a scaffold with a minimum effective pore size of 20 μm ⁴⁸. Because of the limitations of FFES, there are many alternate ES techniques; designed to better control precision patterning.

In the 20th century, ES saw a surge of new experimental investigations, resolving many of the fundamental mysteries surrounding ES physical phenomena. We see this in the works of John Zeleny¹³³ in 1914, Geoffrey Taylor¹³⁴ in 1964 and Peter Baumgarten¹³⁵ in 1971. By this time, the instability of the whipping jet was understood, but only first observed in 1995 using high speed cameras, in work by Reneker *et al.*¹³⁶. The ES jet whips due to electrostatic instability. This instability was finally overcome in 2006, in the demonstration of the first direct write electrospinning method, by Sun *et al.*^{137,138}. Near-Field Electrospinning (NFES).

Their method was akin to dip pen lithography, where a pointed tip, dipped in polymer solution, drew patterns using the jet under a high voltage, at a reduced working distance of 500 μm to 3 mm. This allowed a straight jet to form, avoiding the whipping effect.

1.5.2. NFES 2D Patterning

In ES, the jet initially emanates as a coherent stream for a short distance, with limited axial perturbation, and this coherence is exploited by several modified methods of ES. Near-field electrospinning is a technique, analogous to FFES, which uses a reduced working distance (<10mm) ¹¹¹ and voltage. This forestalls jet whipping instabilities and, using stage translation, directly drawn fiber patterns can be achieved. As the electric field strength is inversely proportional to electrode separation, far lower bias potentials are required (~200V- 2kV) to achieve threshold intensity and thus initiate spinning. Figure 1.6 (A) shows the ejection process as the stage is moved laterally relative to the camera, with schematic Figure 1.6 (B) and microscopy of typical direct writing outcome showing curling at the slower peripheral region.

Stage translation exerts a mechanical drawing force on the fiber in addition to the electrostatic drawing force ¹³⁹. Resolution, positioning, and alignment of nanofibers rely on stage performance. Speed plays an important factor in this deposition; the stage must decelerate and accelerate. When printing, this can cause the fibers to build up locally on the surface as a randomly non-woven mat (see upper right of Figure 1.6 (C)). Coiling effects in direct write NFES are observed in cases of jetting velocities being mismatched with stage velocity ^{140, 141}, and arise due to the impinging solid fiber at the base of the jet at the surface. Typically this is circumvented through the use of ‘waste zones’: areas where the printer can accelerate and decelerate, which are removed or screened out from the final product. Another method of eliminating these aberration effects is through the real-time control of jet velocity, proportionally adjusting this velocity with the stage velocity, by controlling the bias potential accordingly.

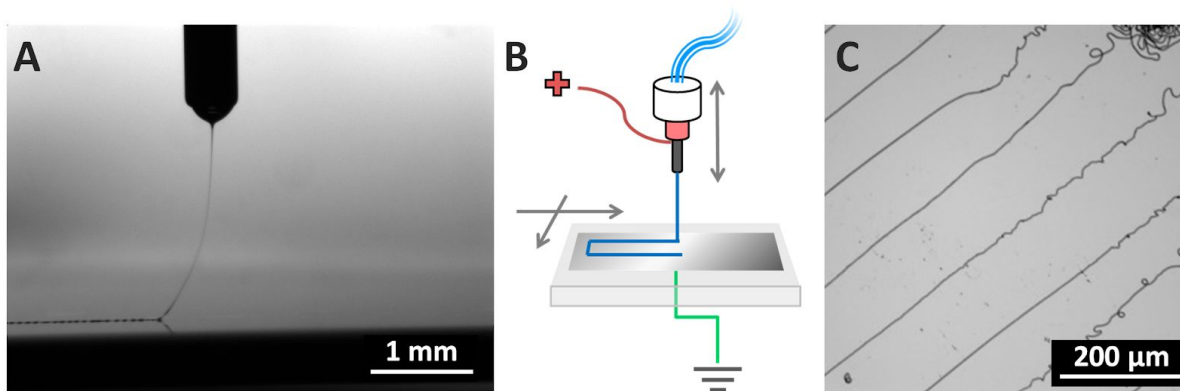


Figure 1.5. Emission process. (A) Camera image of blunt tip emitter, patterning on planar silicon wafer electrode. (B) Schematic of the NFES system. (C) Microscope image of PEO fibers on the surface of a glass slide produced by NFES.

There exist several distinguishing characteristics of NFES compared to conventional methods. Pre-emptive jet initiation can be achieved in NFES, by distorting the droplet using a very fine pointed tip. This breaks the surface tension by creating a localised electric field on the droplet's surface (e.g. using a tungsten tip ¹³⁸), or by physically breaking the surface (e.g. using a glass microprobe tip ¹⁴²).

The relative motion allows control of fiber orientation, while the geometry and material of the electrodes influence the shape of the electric field ¹¹⁶. This has been utilised to improve the outcomes of direct write NFES. For example, researchers have seen an improvement in direct write electrospinning by using a large disc electrode, surrounding an emitter outlet, compared to the typical small cylindrical tip emitter ¹⁴³. This functions to make the electric field lines flow tangentially to the surface of both emitter and collector. The emitting jet is constrained to follow these field lines, improving the writing accuracy and precision compared to conventional tip emitters, whose electric field profile conforms around the shape of the tubular emitter.

There are a number of research groups investigating means of accuracy improvement in NFES. Xu *et al.* changed the electric field lines of conventional ES by replacing the planar collecting electrode by an insulated grounded copper wire, held pointing upward beneath a collecting substrate ¹⁴⁴ (see Figure 1.7 (A)). The wire is held stationary relative to the

spinning capillary, while the stage moved the collector. In this setup field lines are focused directly beneath the tip and so highly aligned fibers were produced. The same group showed the stabilising effects of using secondary guiding electrodes to enhance NFES¹⁴⁵. Huang *et al.* using advanced stage control methods and Near-Field melt ES, were able to generate dot nodes on fibers (see Figure 1.7 (B)) by pausing the motion of the stage periodically¹³⁹.

More sophisticated methods of manipulating electrical field lines, such as electrostatic or magnetic deflectors (used in cathode ray tubes) and quadrupole ion traps (used in mass spectrometry) have the potential to allow printing of more complicated shapes¹⁴⁶ by minimising aberration effects. The sensitivity of the jet path to electric field can be seen in multiple spinneret NFES, in which charged jets deflect each other when in proximity, as shown in work by Wang *et al.*^{147–149} (see Figure 1.7 (C)). Yen *et al.* used multiple spinnerets to produce PVDF piezo effects on the surface of a Bear Cicada wing, demonstrating the energy harvesting capabilities of the piezo fibers¹⁵⁰.

More sophisticated methods of manipulating electrical fields, such as electrostatic or magnetic deflectors (cathode ray tubes) and quadrupole ion traps (mass spectrometry) have the potential to allow printing of more complicated shapes by minimising aberration effects¹⁴⁶. Early works in the area of auxiliary electrode electrospinning involved the use of lensing and plate electrodes. Deitzel *et al.* used electric lensing elements, ring electrodes, to stabilise FFES fiber jetting to control the deposition location and area¹⁵¹ (see Figure 1.7 (D)). Bellan and Craighead took this one step further, producing simple patterns through electric field manipulation by means of a focusing voltage regulated electrode disc, compartmentalized into focus and steering elements¹⁵² (see Figure 1.7 (E)). Zhu *et al.*¹⁵³ using NFES, printed sinusoidal wave patterns by applying an AC bias across two facing electrodes, placed at either side of the printing area (see Figure 1.7 (F)).

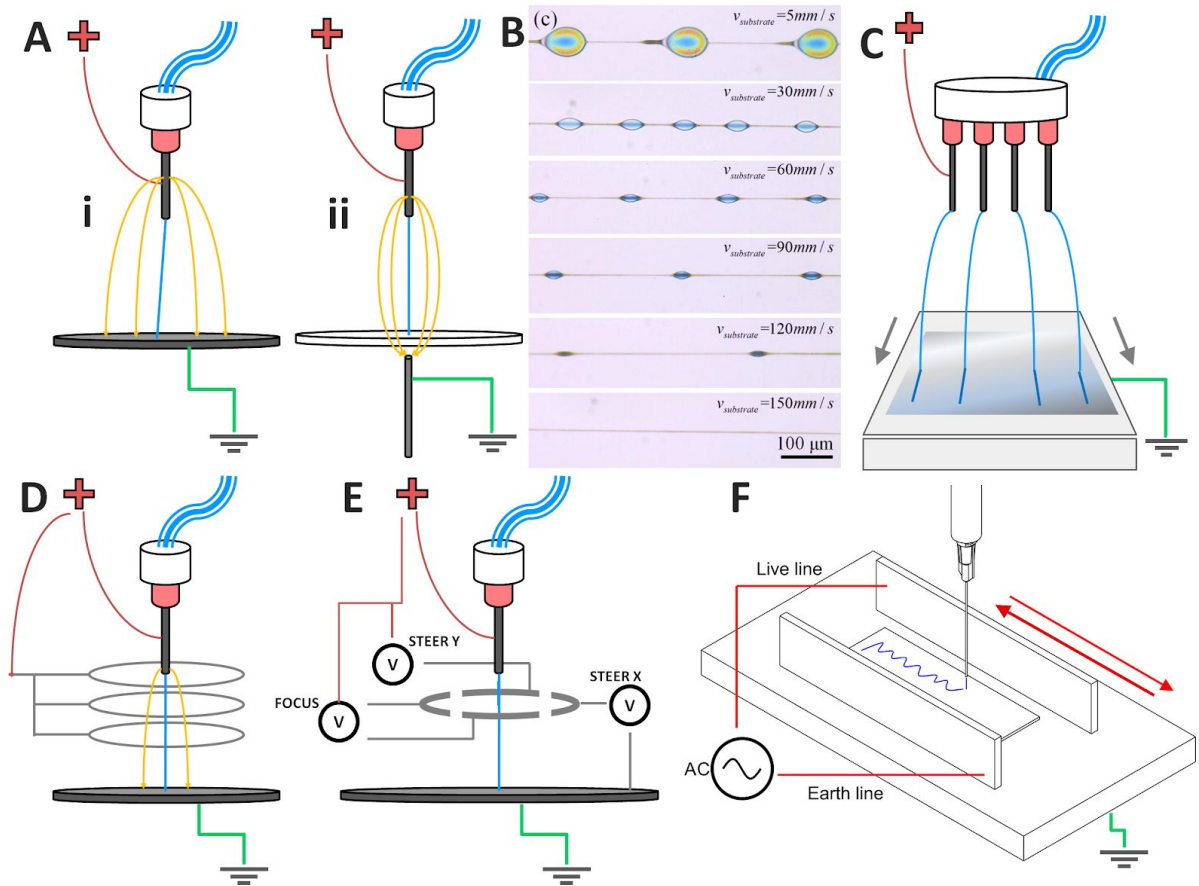


Figure 1.6. Electric field effects in novel direct write NFES. (A) i) typical stage translation electric field of NFES, ii) Non-conductive surface with single grounded point below, showing field line convergence/sharpening ¹⁴⁴. (B) Results of stage control producing dot nodes on fibers ¹³⁹. (C) Multi-spinneret NFES, showing the controlled four pronged ejection, with bowing jet due to charge repulsion ^{147–149}. (D) multi auxiliary ring electrodes positively charged to columnate the field lines of NFES ¹⁵¹. (E) AC modulation of auxiliary plates modulating the jetting angle, sinusoidally ¹⁵².

Research has shown that cells show improved behaviour, organising around fibers with sub-micron diameter fibers ^{30,37,154}. NFES allows the precise deposition of such fibers, in structures with potential application in biomedical engineering. Fuh *et al.* utilised NFES to fabricate highly aligned chitosan nanofibers, controlling the density on the collector ¹⁵⁵. This influenced the morphology and distribution of human embryonic kidney cells, providing a method to modulate cellular behaviour. In a later study Fuh *et al.* ¹⁵⁶ controlled/guided cell orientation using ultrafine alginate fibers fabricated by NFES on a conductive polypyrrole film. Decreasing the fiber interspacing led to an increase in cell alignment.

NFES presents a straightforward and cost effective method of producing nanofibers with controlled deposition. However there are a number of limitations to the process. NFES requires a difficult optimisation process, as it is easily destabilized by solution and process parameters. This constrains NFES material versatility by a material's capacity to meet solution requirements: such as viscosity, volatility, and conductivity. NFES scalability is limited, as multi capillary systems have tip-to-tip interference aberration effects ¹⁴⁷. NFES is primarily used as a rapid prototyping technique because of this restriction. In terms of resolution, NFES systems lack fine control when producing complex microscopic elements with cornering and acceleration associated aberrations and the ability to print discrete elements with precision has yet to be demonstrated.

Nanofibrous assemblies may be incorporated into hierarchically structured materials, focused on mimicking natural human extracellular tissue ⁵⁰. However, solution based NFES has until recently been best suited to 2D surface patterning, while 3D layer-by-layer patterned structures have been achieved through the more stable melt based electrospinning. However, this method has its material and output drawbacks, to be discussed in the following section. When there is a need for complete 3D spatial accuracy, other process technologies would be preferable, such as multiphoton lithography, which currently have their own material and throughput limitations. It is the aim of this research to expand the applications of solution NFES to produce 3D nanofibrous scaffolds for NTE applications.

1.5.3. NFES 3D Patterning

There exist a number of novel solutions to the objective of creating 3D electrospun nanofibrous assemblies. This section aims to give an overview of the modern methods of achieving this, with a focus on their advantages and shortcomings.

By contrast to FFES, the NFES technique is more applicable to a number of NTE applications. 3D NFES can apply stage translation to dictate fiber location, orientation and length. This allows deposition of nanofibers to achieve:

- i. The localisation of multiple motifs. For NTE this may include growth factors encapsulated with certain designated spatial gradients.
- ii. Controllable, pattern-based structural reinforcement of a greater structure ^{43,157}.
- iii. The control over bulk porosity, where NTE requires a minimum pore size for cell infiltration.
- iv. Controllably variable fiber alignments within a structure. While alignment is achievable in FFES using rotator collectors, the alignment is singular. In 3D NFES alignments can act in any number of directions ¹⁵⁸, overlapped (see Figure 1.8 (D)). In NTE fiber alignment can generate directional axon growth ^{50,130}, while other native tissues may benefit from alternating alignments, such as corneal epithelial/stroma tissue ¹⁵⁹.
- v. Strategically placed transmissive or receptive nanofibers for the purpose of electrostimulation or biosensing.
- vi. Subtractable or hollow fiber channels structures which promote fluid flow within a medium; in order to facilitate the removal of wastes and supplying of nutrients to seeded cells ¹⁶⁰.

1.5.3.1. 3D Melt Electrowriting

Melt electrowriting (MEW) uses heated melt polymer instead of solution. MEW has been used to generate a variety of scaffold designs ^{161–163} and compared to NFES, near-field MEW has had more impressive early successes in transitioning to produce 3D architectures, due to the high viscosity, and thus stability, of molten polymer. In 2011 Brown *et al.* demonstrated MEW creating PCL written walls 10 layers high (Figure 1.8 (A-D)) ¹⁶⁴. However, fiber diameter was a few micrometers because the melt viscosity needed to be high enough to slow the jet velocity. PCL scaffolds were fabricated by MEW in work by Farrugia *et al.* ¹⁶⁵, achieving dermal fibroblast infiltration of the mesh (Figure 1.8 (E)). Ristovski *et al.* ¹⁶⁶ increased the number of achievable layers (up to 200 layers high, 2 mm thick) in MEW, applying a positive and negative voltage difference at each electrode. They examined murine calvarial cell seeded on the lattice scaffolds produced, achieving attachment and spreading.

In 2015, Visser *et al.* generated microfiber-reinforced GelMa scaffolds ⁴⁰. To achieve this they applied MEW to generate microfiber grid structures of PCL, 2mm high. They then

placed ~10 of these grids in a cylindrical mould and enveloped the scaffolds within a Gelatin methacrylate (GelMa) matrix (Figure 1.8 (F)). Later in 2015, Hochleitner *et al.* produced submicron fiber grids, 50 fibers high, using MEW, and performed cell adhesion studies using human mesenchymal stromal cells, achieving long term cell culture (Figure 1.8 (G-H))¹⁶⁷. Further optimisation and increased precision of the process has been achieved by Hrynevich *et al.* who used direct MEW, manipulating speed and pneumatic force, to effectively modulate poly(ϵ -caprolactone) (PCL) fiber diameter¹⁵⁸. More complex structures were achieved by McColl *et al.* who used direct MEW on the surface of a rotating tube, achieving tubular scaffolds of PCL¹⁶⁸.

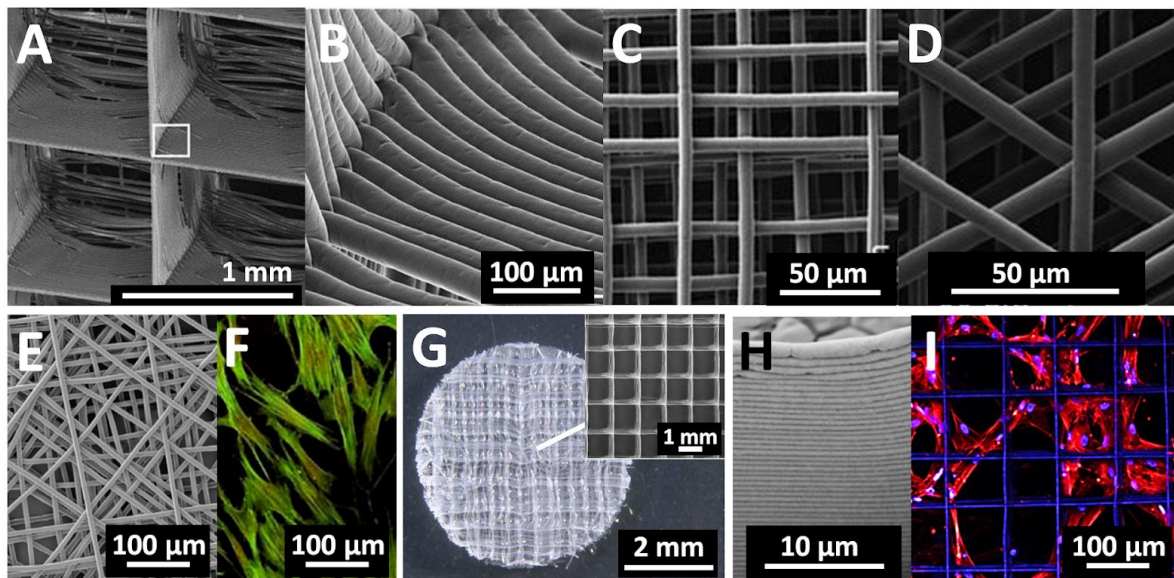


Figure 1.7. MEW scaffolding. (A-D) Microfiber PCL structures generated by MEW in work by Brown *et al.*¹⁶⁴. (A) Stacking and (B) zoom view interweaving of fibers to form an array of 1 mm³ boxes. (C) 90° and (D) 60° oriented overlapping scaffold layers. (E) Fibrous lattice mesh with fine control of structural alignment¹⁶⁵, with (F) fluorescence image of dermal fibroblast infiltration. (G) Gelma hydrogel with encapsulated fiber lattice structure⁴⁰. (H) Work by Hochleitner *et al.* showing many layered microfibers with (I) fluorescence microscopy showing attached mesenchymal stromal cells¹⁶⁷.

The main weakness of MEW is that the list of viable materials for use is limited, as only a small number of polymers can withstand the degrading temperatures used in the melting process. There is a much wider variety of viable and tested polymers in solution based ES.

Additionally, when it comes to solution NFES, there are some more novel approaches to generating 3D nanostructures.

1.5.3.2. Novel 3D NFES

A number of atypical NFES methods have found means by which to manipulate the electric field for the generation of 3D structures. The electrospun jet can be induced to coil more controllably, and this is demonstrated by Kim *et al.* in the generation of hollow coiled ‘nanopottery’ on the surface of a needle apex ¹⁶⁹ (See Figure 1.9 (A)). This PEO nanofibrous structure was formed due to a coiling phenomenon arising from electric field lines centred on the needle tip.

This point electrode geometry has also been used to achieve heightened focusing of the NFES direct write jet. Lee *et al.* incorporated a large hollow cylindrical electrode around the emitter, as well as a sharp pin ground electrode, to focus the jet, creating planar written microstructures ¹⁷⁰. Xu *et al.* used a similar method in their work, generating nanofibers via NFES, using a single electrode point, to focus the electric field and the jet ¹⁴⁴.

Linear collector electrodes operate to localise and focus the electric field, guiding the electrospun jet to whip along the linear path. In 2014, Lee *et al.* placed a thin conductive line on a non-conductive surface and allowed the jetting fiber to whip across this line in a periodic, pendulous motion ¹⁴⁶ (See Figure 1.9 (B)). The electric field lines converge at the surface of the line and so draw fibers to align in-plane. This allowed multiple layers of fiber to be generated, creating free standing nanowalls up to 300 fibers high. One major problem of this layered fibrous electrospinning is the diminishing force of drawing to the collector due to the accumulation of residual charge and insulating polymer.

In 2015, Luo *et al.* produced aligned structurally stable, out-of-plane, layered fiber structures from PVDF, in a similar manner to Lee *et al.*, but without a predesigned ground template ¹⁷¹, see Figure 1.9 (C-E). To achieve this they used NFES to directly spin onto a plain printing paper substrate, sitting atop a heavily doped silicon wafer was grounded plate electrode. As the fibers were laid out on the surface of the paper, solvent was absorbed into the material.

The infiltration of residual solvent into the paper substrate caused the resistance of the paper underneath the deposited fiber to decrease dramatically, enhancing charge transfer through the fibrous network within the paper, between the electrode and the fibers. This causes the fibers, in their initial pattern, to become grounded. Subsequent fibers then deposit in an aligned manner on top of these grounded fibers, forming microscale assemblies. In Figure 1.9 (D) we see a similar coiled nanopottery structure as in Figure 1.9 (A), but much larger in size.

Advances in direct write solution NFES can allow 3D lattice layer-by-layer structuring as seen in MEW results. He *et al.*¹⁷² used solution NFES direct write to generate 3D walled lattice microstructures from fibers of PEO/PCL mixed with multiwalled carbon nanotubes. They studied the proliferation of rat myocardial cells on these structures, showing cell elongation and alignment with the microfiber structure.

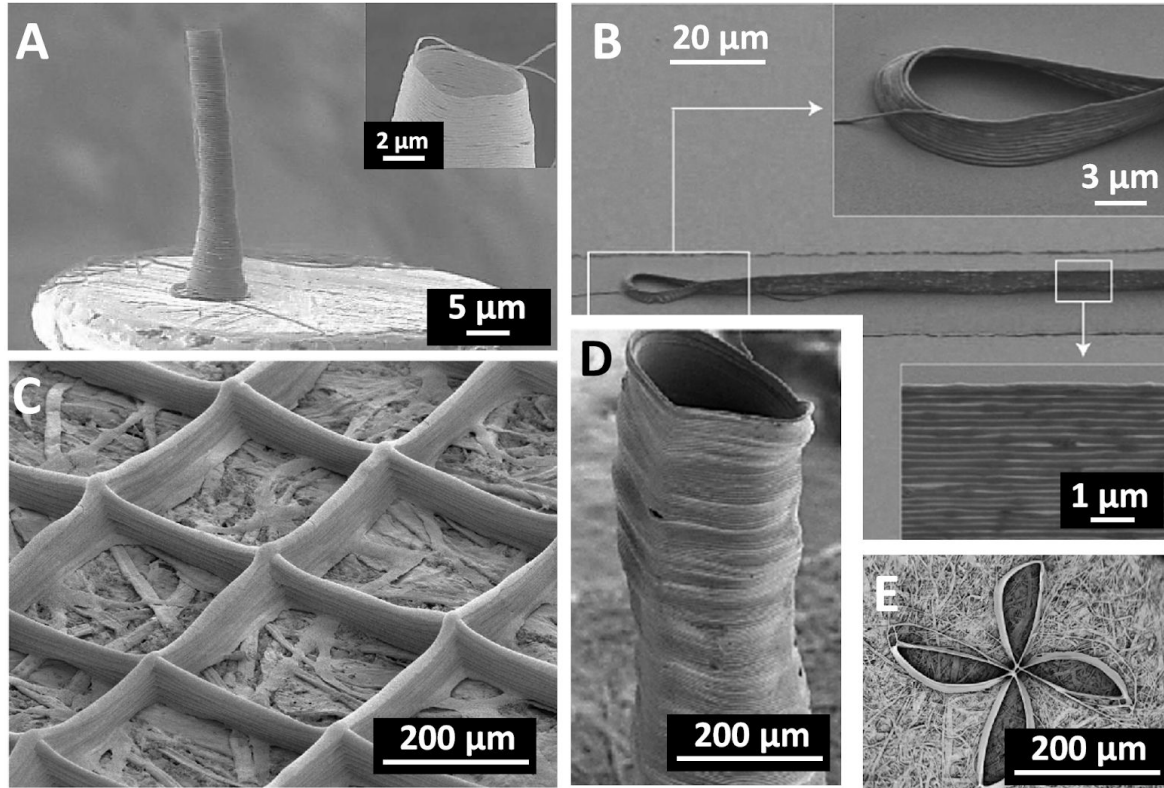


Figure 1.8. Novel NFES methods. Nanopottery tube generated on the top of a blunt pin ¹⁶⁹. (B) Nanowalls using single line electrode ¹⁴⁶. (C-E) Images of structures generated using paper as a substrate ¹⁷¹. (C) Lattice walled microstructure on paper substrate. (D) Tubular structure patterned on the surface of paper. (E) Pinwheel microwall structure demonstrating the versatility of the paper substrate in the NFES process.

1.5.4. 3D Suspension Electrospinning Techniques

Researchers have developed a number of novel solutions to the objective of creating 3D electrospun nanofibrous structures by suspension, using both conventional FFES and NFES. Large dumbbell shaped rotating collectors were developed by Zhu *et al.* generating large nanofiber meshes using FFES with controllable folding of the mesh between the discs of the dumbbell ¹⁷³. Using compressed air assisted FFES Liang *et al.* utilised a four-pronged rotating mandrel collector to generate large scale ultrafine fiber mesh structures, suspended between the arms of the mandrel, forming umbrella-like folding between the mandrel ¹⁷⁴.

More complex rotating structures have been used to suspend nanofiber mesh structures controllably. Tokarev *et al.* modified the rotating drum collector technique, adding spiked

bristles, and this allowed the collection of large volume suspended fibrous meshes ¹⁷⁵. Using a configurable needle array structure on a connective stripboard, Zhang *et al.* used FFES to suspend poly(L-lactic acid) (PLA) hierarchical fibrous meshes ¹⁷⁶. The randomly oriented meshes highlight one issue of previous research, which sees the majority of suspension electrospinning investigation apply conventional working distances ^{47,176–179}.

Another method to suspend aligned fibers, uses two conductive plates to promote alignment in the space between plates ^{180–182}, due to parallel electric field lines in this gap. Fibers are directed to orient across the space by the field alignment. Compared to rotational collection, this method is limited in the total mass of fiber that can be suspended. An example of this technique is shown in Figure 1.10 (A), illustrating work by Fuh *et al.* ¹⁸¹ who used NFES to generate aligned fibers in the regions between gold covered electrode plates. Liu and Dzenis investigated the parameters surrounding the parallel plate technique in the pursuit of alignment optimisation ¹⁸². Baker *et al.* worked using a similar method, achieving analysis by AFM of the suspended poly-ε-caprolactone (PCL) fibers ¹⁸³. Taking the parallel plate principle outlined in work by Li *et al.* ¹⁸⁰, Beachley *et al.* ¹⁸⁴ advanced this technique by introducing parallel automated collecting tracks, continuously producing aligned suspended fiber arrays.

Purely linear electrodes were employed by Teo *et al.*, generating suspended electrospun fiber bundles of aligned nanofibers over two fixed points in the space between two upright aligned razor blades ⁴⁷ (shown in Figure 1.10 (B)). Kriebel *et al.* produced suspended parallel oriented PCL fibers by FFES on 3D staircase electrodes, suspending the fibers within a collagen gel through embedding and casting ¹⁷⁹. This construct promoted schwann cells migration and sensory neuron axonal regeneration. Bisht *et al.* demonstrated a high precision direct write suspension NFES process, by directly suspending nanofiber across microscopic carbon electrode arrays (see Figure 1.10 (C))¹⁴².

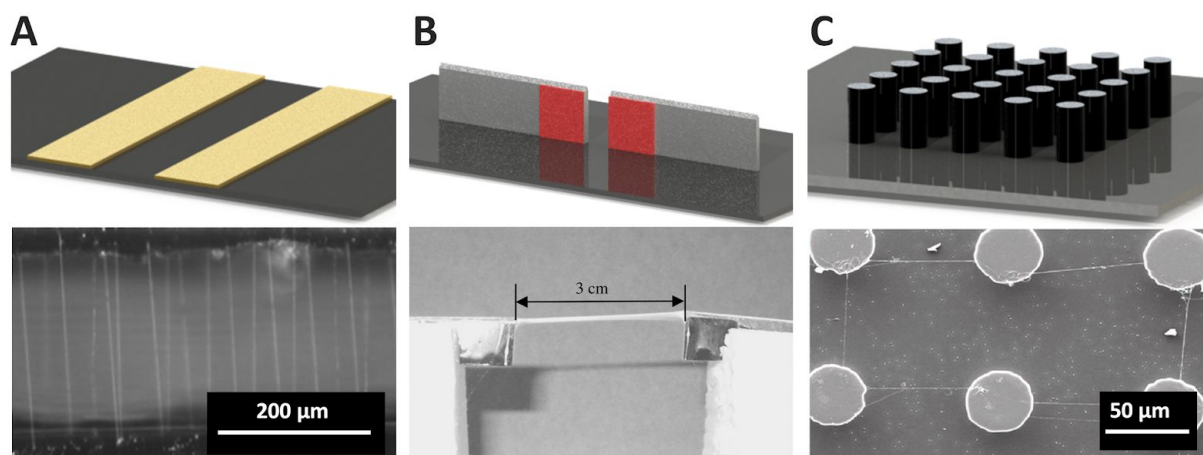


Figure 1.9. Suspension ES techniques. (A) Razor blade electrodes, with insulating tape (marked red) covering the sides in the working region ^{47,173}; (B) Planar gold plated electrodes ¹⁸¹ (C) Array of carbon posts with high magnification SEM image, produced by Bisht *et al.* ¹⁴².

Table 1.3 and table 1.4 list a number of experimental reports, including those discussed, which use novel collector geometries and/or translation to achieve aligned, suspended and 3D ultrafine fibrous structures.

Table 1.3. Linear and Planar Electrode Suspension Electrospinning

Electrode	Fiber Structure	Material	Method	Application	Year	Author
Linear Electrode						
Razor blades	Suspended aligned fiber bundles suspended between blades	PCL	FFES	Composites	2005	Teo <i>et al.</i> ⁴⁷
Planar Electrodes						
Plate electrodes, equally spaced	Aligned, suspended over gap	Carbon, SnO ₂ , TiO ₂ /PVP, TiO ₂	FFES	Electronic	2003	Li <i>et al.</i> ¹⁷⁷
Plate electrodes, equally spaced	Aligned over interspacing of planar plate electrodes using NFES	Pd doped PANI	NFES	Electronic	2011	Chen <i>et al.</i> ¹⁷⁸
Plate electrodes, equally spaced	Aligned, suspended over gap	PEO	NFES	Microfluidics	2007	Sanghoon <i>et al.</i> ¹⁶⁰
Aluminium electrodes on glass	Aligned, suspended over gap	PVDF	NFES	Piezoelectric	2010	Pu <i>et al.</i> ¹⁸⁵
Suspended post-fabrication in culture media	Mesh	PLGA	FFES	Tissue Engineering	2015	Ru <i>et al.</i> ⁵¹
Plate electrodes, equally spaced	Aligned, suspended over gap	PVDF	NFES	Piezoelectric	2013	Fuh <i>et al.</i> ¹⁸¹

Table 1.4. 3D Electrode Suspension Electrospinning.

Electrode	Fiber Structure	Material	Method	Application	Year	Author
Dual collection rings	Suspended fibers	PCL	FFES	Tissue Engineering	2005	Dalton <i>et al.</i> ¹⁸⁶
Micropillar electrode array	Suspended fibers	PEO	NFES	Various	2011	Bisht <i>et al.</i> ¹⁴²
Selectively charged needle array	Suspended unaligned fibers	PLLA	FFES	Tissue Engineering	2009	Kai <i>et al.</i> ¹⁷⁶
A series of triangular ridges	Suspended dry fibers	Hyaluronic acid	FFES	Tissue Engineering	2011	Liu <i>et al.</i> ¹⁸⁷
Rotating spiked roller (i.e. cylindrical brush)	Suspended unaligned fibers	PEO	FFES	Tissue Engineering	2015	Tokarev <i>et al.</i> ¹⁷⁵
Dumbbell shape	Suspended Mesh	PVDF	FFES	Tissue Engineering	2016	Zhu <i>et al.</i> ¹⁷³

1.6. Thesis Aims

A major goal in tissue engineering is to mimic the native nanofibrous protein architectures found in the extracellular matrix (ECM). Cell culture research has found that 2D culture is insufficient to emulate what cells experience *in vivo*, and so TE aims to produce 3D architectures, at various hierarchical scales.

Near-Field Electrospinning (NFES) is a versatile nanofiber patterning technique, which has recently advanced to utilise the layer-by-layer method to create microstructures, designed to mimic these ECM architectures. However, the layer-by-layer method generates disconnected pores, and high volume can be difficult to achieve due to inhibition of the ejection process by layer build-up. Given this technique currently cannot effectively provide the

volumes/structures valuable for TE, this research aims to generate 3D suspended polymer nanofibers, through the use of novel collectors, and a new suspension NFES technique. This technique compared to previous suspension techniques will operate to directly write the suspended fibers on the collector, to achieve greater control and alignment,

We aim to devise a near-field electrospinning technique, incorporating selective laser melt manufactured titanium electrodes, in order to fabricate large volume 3D polymer nanoarrays. Nanoarrays can be measured, analysed for their relative isotropy, alignment and diameter homogeneity. It will be necessary to optimise the technique by a number of orthogonal parametric studies and investigate pattern variation, as well as the technique's capacity for repeated patterning.

Finally the system produced can be implemented within a biocompatible hydrogel matrix to examine its effects and to allow further investigations in its effectiveness for neural tissue engineering. To this end, once developed, these arrays shall be incorporated into a biocompatible hydrogel matrix, to provide a complete hierarchical MTC for NTE.

To achieve these goals, the following specific aims are pursued:

Aim 1: To develop an NFES direct write platform, through the use of software programming and system engineering, and demonstrate 3D suspension NFES.

Aim 2: To generate 3D polymer nanoarray structures using 3D electrode collectors and to investigate the effects of different process parameters.

Aim 3: To integrate suspended fibrous arrays into a biocompatible hydrogel matrix.

1.6.1. Thesis Structure

1.6.1.1. Chapter 2.

A Direct 3D Suspension Near-Field Electrospinning Technique for the Fabrication of Polymer Nanoarrays. This chapter details the development of a NFES platform, tests 2D

NFES patterning, and details the first production of directly written suspended nanofiber arrays on four-pillar electrodes.¹

1.6.1.2. Chapter 3.

Patterning and Process Parameter Effects in 3D Suspension Near-Field Electrospinning of Nanoarrays. This chapter describes the production of suspended polymer nanoarrays and the results of experiments conducted varying working parameters of SNFES. The results of multiple studies are investigated and discussed in terms of the fiber array orientation, homogeneity and diameter distribution.

1.6.1.3. Chapter 4.

Suspended 3D Polycaprolactone Nanofibers Encapsulated within a Gellan Gum Methacrylate Hydrogel for Neural Tissue Engineering. This chapter describes the construction of hybrid hydrogel/fiber array structures, and discusses the results of investigations of the effects of parameter and electrode variation on final construct mechanical and structural outcomes.

1.6.1.4. Chapter 5.

Conclusions and Future Perspectives. This chapter summarises the results of the studies conducted, examining the failures of the research, and discussing future research concepts and hypotheses.

Chapters 2, 3 and 4 are presented as they were published or submitted.

1.7. Supplementary Section

Table 1.5. Electrospinning Timeline

Electrospinning Timeline			
Year	Name	Description	Class
1600	William Gilbert	Electrospraying Description	Theory
1749	Jean-Antoine Nollet	Electrospraying Development	Theory
1897	Baron Rayleigh	Observed Electrospinning	Theory
1902	John F. Cooley	First Electrospinning Patent	Patent
1902	William J. Morton	Electrospinning Patent	Patent
1914	Baron Rayleigh	Related study	Theory
1917	John Zeleny ¹³³	Electrified liquid surfaces	Theory
1934	Antonin Formals	Solution Electrospinning Patents	Patent
1936	Charles L. Norton	Melt-Electrospinning	Advance/Patent
1939	I. Petryanov-Sokolov ¹⁸⁸	Petryanov filters	First Application
1964-69	Geoffrey Taylor ¹³⁴	Taylor Cone Theory	Theory
1971	Baumgarten P.K. ¹³⁵	Solution viscosity dependence	Theory
1978	Annis and Bornat ¹⁸⁹	Vascular prosthesis using ES mats	TE Application
1981	Larrondo and Manley ¹⁹⁰	Polymer melts	Advance
1985	Annis and Fisher ¹⁹¹	In vivo arterial prosthesis	TE Application
1995	Darren H. Reneker ¹³⁶	Whipping observation	Theory

Chapter 2. A Direct 3D Suspension Near-Field Electrospinning Technique for the Fabrication of Polymer Nanoarrays.

This chapter has been adapted, with the author's permission, from the article - 'A Direct 3D Suspension Near-Field Electrospinning Technique for the Fabrication of Polymer Nanoarrays.' published in IOP Nanotechnology ¹.

Published 25th February 2019. Nanotechnology, Volume 30, Issue 19, pages 195301-11.

<https://doi.org/10.1088/1361-6528/ab011b>

Alexander R. Nagle ^{a†}, Cormac D. Fay ^{a†}, Zhigang Xie^b, Gordon G. Wallace ^a, Xungai Wang ^{b*}, and Michael J. Higgins ^{a*}

^a ARC Centre of Excellence for Electromaterials Science, University of Wollongong, Innovation Campus, AIIM Facility, Squires Way, North Wollongong, New South Wales 2500, Australia.

^b Institute for Frontier Materials, Deakin University, Geelong, Victoria 3216, Australia.

*Corresponding Authors

[†]Contributed equally to the study

Author Statement:

The study detailed in this chapter could not have been made without the work of i) Dr. Cormac D. Fay, who produced the NFES platform control software. ii) Mr. Grant Barnsley who acted as fabrication technician of selective laser melt manufacture of collector electrode arrays. iii) Mr. Benjamin Filippi for his work in the fabrication of the automated cleaning device, to which the author contributed manual and intellectual assistance. Testing of this system, development of python coded control software, and revisions to the final integrated software code were completed by the author, Alexander R. Nagle, as well as all experiments and data analysis presented in this chapter.

2.1. Abstract

Near-field electrospinning (NFES) is widely recognized as a versatile nanofabrication method, one suitable for applications in tissue engineering. Rapid developments in this field have given rise to layered nanofibrous scaffolds. However, this electrostatic fabrication process is limited by the electric field inhibitory effects of polymer deposition. This leads to a major challenge: how to surpass this limitation on planar/layered constructs. While the current focus in this area largely lies with the investigation of new materials, techniques and increasing precision of NFES systems and patterning, exploration of complex collector substrates is often restricted by (i) available technology and (ii) access to complex electrode manufacturing tools. To achieve nanofiber arrays suspended in free space, this paper documents both the development of an integrated NFES system and the potential of standing electrodes manufactured via selective laser melting. This system was first tested by 2D patterning on planar silicon, using polyethylene oxide polymer solution. To demonstrate suspension NFES, two patterns operating within and around the standing electrodes produced high volume suspended nanoarrays. Image analysis of the arrays allowed for the assessment of fiber directionality and isotropy. By scanning electron microscopy, it was found that a mean fiber diameter of 310 nm of the arrays was achieved. Effectively manoeuvring between the electrode pillars required a precision automated system (unavailable off-the-shelf), developed in-house. This technique can be applied to the fabrication of nanofiber structures of sufficient volume for tissue engineering.

Keywords: electrospinning, suspension, near-field, nanofiber, electrode, nanoarray

2.2. Introduction

Tissue engineering (TE) applies synthetic and biomaterials to the pursuit of reciprocating natural cellular environments. To achieve this, TE employs additive manufacturing processes to produce, supplement and support microtissue constructs. Native extracellular matrices are composed of nanofibrous protein networks, which provide cells with mechanical, structural and signalling cues, acting as a substrate for cell adhesion and growth. To imitate this matrix, fabrication processes must operate at all levels of resolution, from the macro to the nanoscale.

Following research showing the advantages of ultrafine fibers in cell viability and behavioural studies, nanofabrication has received growing attention for use in TE. Cells are capable of sensing individual polymer fibers with diameters as low as several nanometers⁴⁶, while sub-micron diameter fibers have exhibited improved cytocompatibility^{30,37}. Of the current nanofiber fabrication techniques, solution electrospinning is one of the most extensively applied due to its ease of use, low-cost set-up, variety of material choice, and its ability to deposit at room temperature^{113,116,192}.

In the last decade, electrospinning techniques have been developed that allow for the controlled patterning of nanofibers. Reducing the working distance, as well as the applied voltage, prevents the jetting instability inherent to conventional electrospinning. In this Near-Field Electrospinning (NFES) regime, accurate motion of a planar electrode relative to the emitting tip allows for the control of fiber placement and morphology^{139,193}. Recently, NFES has transitioned from writing 2D patterns to producing 3D ordered structures by direct layer-by-layer deposition^{40,146,167,171,172,194}. This has greatly extended electrospinning capabilities, which has allowed researchers to develop 3D microfiber scaffolds for cell culture research^{40,156,167,195}.

Despite the success of this layer-by-layer NFES process, there are inherent limitations to this technique. Insulating polymer suppresses the electric field, inhibiting deposition and limiting the number of layers achievable. This is problematic when considering that an ideal *in vitro* 3D culture working volume is on the order of 0.1 cm³^{26,40}. One method to resolve this volume limitation has been achieved by Visser et al.⁴⁰, i.e. by delaminating and stacking two 1 mm

high microfibrinous scaffolds, generating an assembly sufficiently large enough for 3D cell culture. However, this method created microfibers, which is impractical for delicate or complex non-planar structures, in addition to being difficult to delaminate and assemble without fragmentation.

An alternative approach is necessary to reach high volume nanofibrous constructs. Electrospun nanofibers can be suspended between electrodes, bridging macroscale distances. Razor blade electrodes ^{47,173}, standing electrode pin arrays ^{142,176}, among other novel electrode collection devices, guide the electrospun jet by electric field localisation. However, in previous research involving suspension electrospinning, the majority apply conventional working distances ^{47,176–178}, which results in the production of chaotically placed fibers. Those which apply a near-field regime achieve low volume structures ^{142,160,178}, which do not meet ideal microtissue construct volume considerations.

In this paper we discuss the development of a NFES system, designed to implement a novel suspension NFES technique, which directly suspends nanofibers interdigitally between pillar electrodes. This technique patterns across these electrodes to achieve nanofibrous arrays large enough for 3D cell culture. These electrode pillars direct the electrospun polymer jet, as well as support suspended 3D nanofiber structures within the interstitial space. Current commercial systems fail to meet precision standards necessary and remain generalised, lacking specific design elements and functionality to examine this concept. Thus it was necessary to develop a system in-house, as what is currently available does not allow for specific modular components, or have a high precision. To best achieve the accuracy required for this study, computerized automation methods were employed, using a number of incorporated automatic elements and software systems. Selective Laser Melting (SLM) manufacturing allowed for the tailored fabrication of the 3D electrodes. Using these electrodes we demonstrate the patterning of uniaxially aligned nanofibrous meshes.

2.3. Materials and Methods

2.3.1. Materials

Polyethylene oxide (PEO) powder (Average Mw ~200,000) was purchased from Sigma-Aldrich Co. (Sydney, Australia). PEO (14 wt%) was mixed with water/ethanol (3:2) using a magnetic stirring bar for 1 hr to reach homogeneity. Titanium Grade 5 (Ti 6Al-4V) powder with spherical particle size < 63 μm , was purchased from TLS Technik GmbH (Bitterfeld, Germany).

2.3.2. NFES Device

2.3.2.1. Instrumentation

A custom NFES device was designed, developed and assembled for the requirements of this study. It consisted of a platform mounted on the X-Y stage, a high voltage supply, a syringe pump mounted on the Z-stage, a camera and an enclosure (see Figure 2.1). Three linear motorised stages were sourced (A-LSQ150B, Zaber), which met the desirable features for this study: a high unidirectional accuracy (15 μm), a maximum speed of 280 mm.s⁻¹, and the capacity for control via an RS232 serial interface. Figure 2.1 (A-I) presents the schematic of the instrument assembly. Two stages were overlaid perpendicular to each other, allowing for movement in the X and Y directions, with a tertiary Z-stage holding a syringe pump (UMP3, World Precision Instruments Inc.). Each stage had a step resolution of 0.5 μm and a repeatability of < 2.5 μm .

On the X stage, an acrylic laser cut platform was attached to position the collecting electrodes. A syringe, with a blunt tipped stainless steel needle (25 G, 0.25 mm inner diameter), was mounted on the programmable syringe pump. This pump drove the syringe plunger using a linear force threaded shaft with a step resolution of 3.2 μm . The needle was positioned and held in a vertical orientation by a small stainless steel drill chuck, located by positioning screws. The needle was connected to ground via the high voltage power supply (ES30, Gamma HV), by crocodile clip connectors and conductive cabling. An automatic

cleaning device (ACD) was positioned beneath the tip (see supplementary Section S1 and Figure 2.7).

An enclosure was built from heat formed laser cut transparent acrylic to house the system. A front hatch was built to allow for access to the system and separate the system from the outside environment for a more controlled operation. Dehumidified air was fed into the case from a compressor source through a pressure regulator (AR40-04H) passing into the case to a terminal pneumatic silencer. The air was fed into the closed case to reduce the humidity to approximately 19% RH, measured using a temperature and humidity data logger (XC0424).

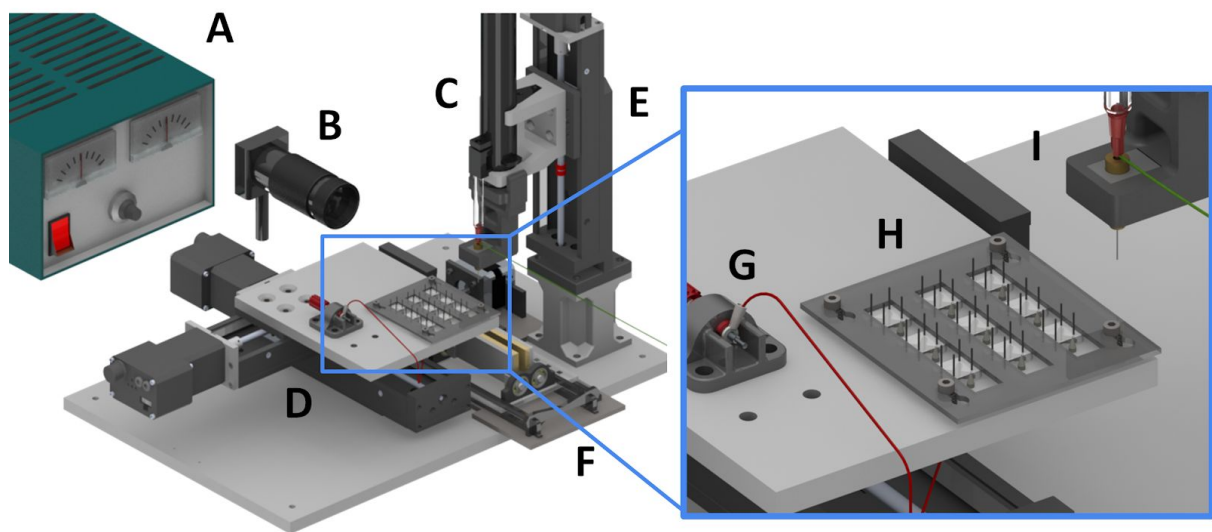


Figure 2.1. Design of the NFES system. (A) High Voltage Power Supply; (B) Camera; (C) Syringe pump; (D) X-Y Stage; (E) Z Stage; (F) Automatic Cleaning Device; (G) Positive bias contact point; (H) 3x3 grid array of electrodes embedded in the acrylic platform (I) Blunt tipped Needle, held by drill chuck, connected to ground.

2.3.2.2. Software Design

The stages, the syringe pump and the high voltage power supply were controlled by in-house developed software. For real-time control, along with desirable stability, the program was written in the C++ programming language using the Qt Framework (The Qt Company Ltd.). The graphical user interface (GUI) was composed of three rows; with the stages, syringe pump, and power supply controls arranged from top to bottom, respectively (see

supplementary Figure 2.8). Each row was separated into four compartments left to right: (1) variable control, (2) information (status), (3) action control (i.e. script), and (4) communications control, respectively.

The development of each peripheral control and sub-system took place in a progressive manner to ensure that all operations were successfully implemented via hard-coding. Once achieved, the GUI allowed for easy manual control of the individual instruments of the system. With all operations and features fully functional, automotive systems were subsequently developed. To allow for repeatable experiment operations and compatibility with 3D slicer programs, the automotive stage system was standardised operate using G-Code. This was achieved by implementing a script loading interface, parsing G-code input script and translating this to the native serial commands of the stages. This development enabled the user to carry out rapid 3D stage motion according to G-code program scripts.

G-code program scripts were output using an online spreadsheet program written in Google Sheets. Patterns were written by formatting the speed, X, Y and Z values to G-code format. Before each operation a series of calibrations were performed in order to mitigate error in positioning. First, a single pin electrode was moved beneath the emitting tip as a coordinate set point. Additional calibrations were performed for proceeding electrodes using a simple calibration script, which moves the pins of each electrode beneath the extrusion needle tip. Visual alignment took place using the magnified view via the camera.

2.3.3. Accuracy Validation

2.3.3.1. Planar NFES Dimensional Accuracy and Precision

To evaluate the effective dimensional accuracy of the stage, in addition to comparing the conventional NFES patterning to the novel 3D patterning technique, 2D patterns of PEO polymer nanofibers were written on doped silicon wafers. The script translated the platform in two stages; (a) stabilisation, followed by (b) nine square wave patterns in a 3x3 grid. The stabilisation pattern consisted of 5 mm long parallel lines with an interspacing of 0.1 mm. The square-wave patterns consisted of ten lines of 7 mm long parallel fibers, interspaced by 0.5 mm. Each row of the 3x3 grid was assigned a stage maximum speed value: 50, 150, and 250

mm.s⁻¹. Each 3x3 grid was repeated with varied working distances between 0.5-10 mm at an increment of 0.5mm. The following process variables were kept constant: the PEO solution concentration (14 wt%), flow rate (3 nl.s⁻¹), needle gauge (0.25 mm inner diameter), and applied voltage (1.6 kV).

PEO solution was loaded in a 1 ml syringe and mounted on the syringe pump. A monochrome camera (Chameleon, PTGrey) was used to calibrate the relative Z-axis position of the blunt needle tip with respect to the electrode surface and to observe the ejection process. The needle tip was held at the 1 mm working distance and a droplet of the solution was formed at the outlet. The voltage was applied and the droplet was manually initiated by breaking the droplet surface using a fine metal tip. After several seconds the patterning was initiated. Upon pattern completion, the voltage was switched off and the needle was withdrawn. Each sample was reproduced in triplicate.

2.3.4. Suspended Nanofiber Fabrication

2.3.4.1. Electrode Fabrication and Mounting

Electrodes were produced using a SLM 3D Printer (SLM-50, Realiser) from grade 5 titanium powder. The electrodes were designed using 3D computer aided design (CAD) software (Solidworks 2016, Dassault Systèmes Solidworks Corp.) and consisted of four pins (0.7 mm diameter, 10 mm tall), standing vertically on an x-shaped base, with two connection pins beneath the base (see Figure 2.2 A), which functioned to stabilise, position and connect the electrode. For SLM fabrication the design was saved in the stereolithography (.stl) file format. Using slicing software Magics (Materialise®), the file was sliced, and support structures were generated for printing. This sliced file was then interpreted into system specific commands by SLM proprietary software (R-Operator, Realiser). Grade 5 titanium powder was layered on the build platform. Each slice was welded by laser, with a layer resolution of approximately 25 µm. Once the electrodes were formed, the platform was removed and the electrodes cut from the surface using side cutters.

To mount the electrodes on the NFES stage, acrylic platforms were laser cut (PLS6MW, ULS inc.) with an exit opening to allow for ground connection to the pins from below. X-shaped grooves (~ 3 mm deep) were laser etched into the acrylic surface to allow for a press-fit

insertion of the electrodes into the platform. This mount was attached to the X-Y platform (by M3 screws) and the electrodes were securely fit within the formed grooves. Acrylic covers were attached over the base of the electrodes to electrically insulate the base from the syringe tip.

2.4.2 Near-field electrospinning onto 3D electrodes

A square wave (SW), inter-pin pattern was selected to generate ordered nanofibrous arrays in the region between two vertical pins. The working distance was defined as the minimum distance between the cylindrical surfaces of the tip and target pins. The upright pattern working plane was located at a certain working distance from two pins and parallel to the plane created by the pins (see Figure 2.2 B). Within the working plane the tip was rastered horizontally, raised with interspacings of 0.1 mm in the Z-axis. This formed the 7 mm wide SW pattern, with a total height of 5 mm. There were two planes for each four pin electrode, parallel to one another (see supplementary video 1 for a demonstration of the process).

To calibrate the position of the syringe tip to the pins, the stage was moved to align one pin below the tip, and the tip was lowered until contact with the pin apex was achieved. A second calibration was performed to align the tip to the initiating pin. The G-code script was then adjusted by these calibrations. The SW pattern was preceded by an initiation procedure in which the solution droplet was contacted upon a fine point stainless steel tip. The SW pattern then followed its path as previously described. The initiation procedure disrupts the surface tension of the droplet allowing the emission process to commence more effectively.

A second pattern was selected to demonstrate the effective repeatability of the suspension NFES technique. This pattern was composed of a square path moving around all four pins in a clockwise fashion outside its perimeter at a minimum working distance of 1 mm (see Figure 2.2 C). This clockwise path performed 15 laps at a single height and was then raised 0.1 mm, and repeated this process. This sequence was repeated for a further nineteen Z axis positions, moving a total height of 1.9 mm (see supplementary video 2). This entire process was repeated a further nine times, effectively patterning at each position 150 times in total. This

pattern demonstrates the systems can capably repeat the NFES technique in order to fabricate nanofibrous structures of comparatively high density.

This square iterative pattern (SI) was performed with preceding and interspersed cleaning manoeuvres in addition to initiation procedures. These procedures were necessary as the emission over time becomes destabilised due to surface tension, or contaminant particles disrupting the emission. Regular cleaning and initiation procedures mitigate these disruptions. The following process variables were kept constant for both patterns: the PEO solution concentration (14 wt%), extrusion rate (3 nl.s⁻¹), needle inner diameter (0.25 mm), maximum speed (250 mm.s⁻¹) and working distance (1 mm).

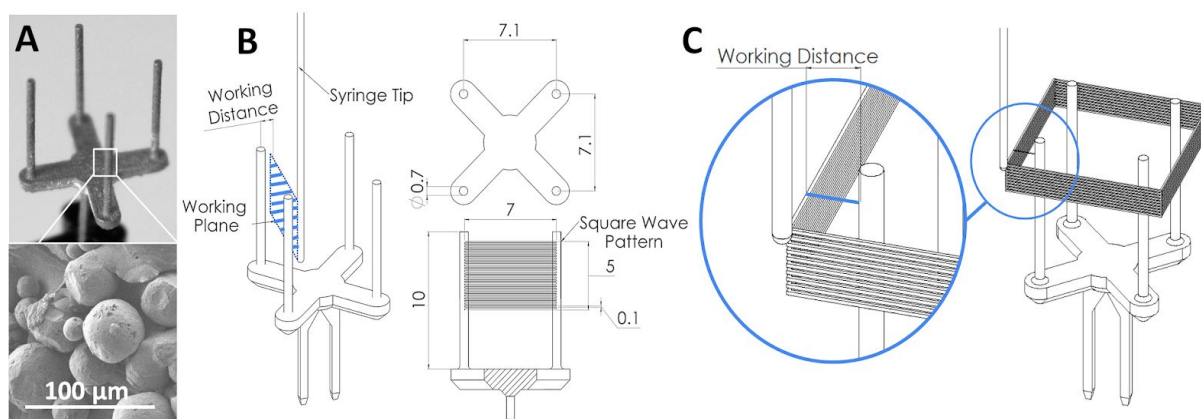


Figure 2.2. Electrode and Pattern Design. (A) Photograph of four pillar electrode with inset showing SEM of microparticle structure of semi-fused titanium. (B) Electrode schematic views (units in millimetres) showing a syringe tip movement working plane in blue; the dimensions of the electrode array, and the 0.1mm interspaced square wave pattern dimensions between the two pins. (C) Pattern schematic of the square iteration (SI) pattern surrounding the four pin electrode, with magnified inset showing working distance.

2.3.5. Characterisation

2.3.5.1. Light Microscopy

2D and 3D fiber arrays were imaged by light microscopy (M205A, Leica Microsystems). To achieve reproducible imaging of 3D suspended arrays the pins were held by their connection pins using bulldog clips mounted on 3D printed bases. Magnification was kept constant at

25× to enable comparative image analysis. Images of samples were semi-automatically analysed using ImageJ software (National Institutes of Health, USA). Images were first cropped then prepared using a variety of contrast enhancements and thresholding written as an automatic macro for ImageJ. The binary segmented images produced were then analysed using ImageJ plugin ‘Diameter J’, which applies the OrientationJ module to determine the orientation distribution (OD) of the fibers.

2.3.5.2. Scanning Electron Microscopy (SEM)

Prior to SEM imaging, silicon wafers and pin electrodes were attached to stainless steel stubs using carbon tape. Electrical contact between the electrodes and the base was ensured by using conductive silver paint. Note: the fibers were not coated with any conductive metal. This avoided the potentially destructive sputter coating process as well as allows SEM acquisition of fibers due to the higher contrast as a consequence of charge build up on fiber surface. SEM was performed using a JEOL 7500 operating at 10 kV, and 5 mA. From the SEM micrographs the diameters of the fibers were measured. An excess of 10 measurements per SEM micrograph were performed, with a minimum of four micrographs per sample. From these measurements the average fiber diameter and standard deviation were calculated.

2.4. Results and Discussion

2.4.1. Accuracy Validation by Planar Nanofiber Patterning

To evaluate 2D nanofiber patterning capabilities, a 3x3 grid of patterned lines was produced with three subgroups, varying maximum speed for each row. Bare planar silicon electrodes were chosen as a substrate to minimize surface artefact interference in both NFES patterning and imaging. The range of working distances was chosen given the typical working range for NFES is ca. 0.5-10mm, with previous findings showing an improved patterning precision working at the lower end of this range. From an examination of working distances between 0.5-10 mm (at an increment of 0.5 mm); 6 mm to 8 mm were found to produce the most accurate patterns (see supplementary section Figure 2.9). Arcing occurred at 0.5 mm WD, inhibiting stable emission, while working between 8.5-10 mm electrospinning could only be briefly maintained using 1.6 kV. No significant effect in patterning at the macroscale was found between the maximum speeds applied (50, 150 and 250 mm/s). The reproducibility of these outcomes demonstrate the system's control over working events and conditions

Figure 2.3 A-C illustrates an increase in writing fidelity as the working distance is increased from 1-2 mm. The jetting regime changes from multiple splaying jets (1 mm), to fewer jets (1.5 mm), to a single coherent jet (2 mm) as the working distance is increased. For working distance from 1.5 - 5 mm finite regions of inhomogeneous deposition to the left and right extremes of the arrays can be observed (see Figure 2.3 (B-D)). This inhomogeneity is not due to the onset of electric bending instabilities, rather it is caused by the stage drawing the fiber away from the origin, causing angular deflection of the jet ^{139,146}. The force of drawing is lower on the jet, meaning its direction does not change as quickly as in 1 mm samples, leading to pooling of the jet at one point, due to the latency in drawing force.

Patterning accuracy becomes ideal between 5 and 6 mm (fig. 3 (D-E)) as a result of effective drying of the solution, which inhibits such fluid flow effects. A similar transition can be seen between 1 and 1.5 mm, with multiple smaller jets drying at a faster rate, due to the increased surface area. Figure 2.3 F, shows the normalised OD for the arrays (Fig. 3 A-E), with the inset showing a 80-100° region visually demonstrating an ideal raster pattern for Figure 2.3 A and E.

It was practical to establish a 2D NFES technique using this platform in order to validate the platform writing operation, and to establish a working parameter domain as a starting point for 3D suspension NFES. Finally, this allowed a comparison to take place in order to explore differences between techniques, in terms of outcome and jetting behaviours. Parameter conditions are equivalent between the two techniques of 2D patterning and 3D suspension. The distinguishing characteristics between the techniques were defined by their respective substrates and applied patterns. In 2D NFES, working distance does not vary, producing a fixed electric field with respect to the emitter. In 3D NFES the angle of the jet is not aligned with the emitter, and the electric field varies as the electrodes move relative to one another.

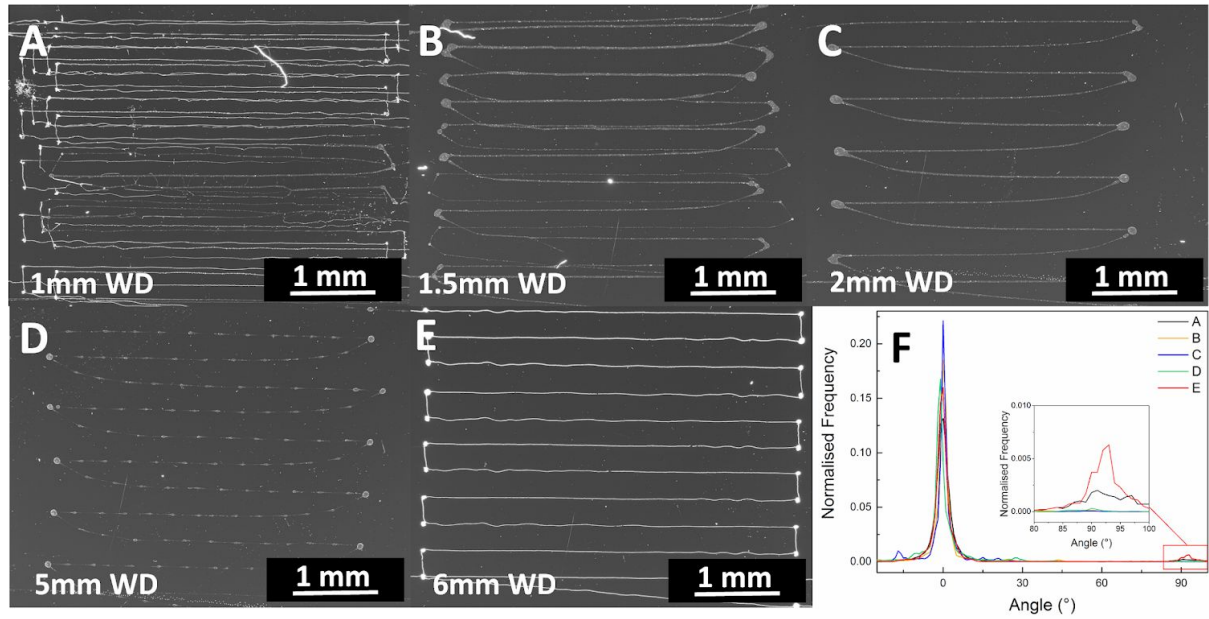


Figure 2.3. Planar Nanofiber Patterning. (A-E) Microscopy images of PEO fibers on silicon wafers at different working distances. (F) The OD for images A-E, with inset showing region of interest in the 80-100° range.

2.4.2. 3D Suspended Nanofiber Array Fabrication

2.4.2.1. Nanofiber Suspension by Square Wave pattern

Two 3D patterns were demonstrated, SW and SI, producing suspended nanofibrous arrays upon 3D electrodes. The optimal product of the SW pattern is to generate homogenous axially aligned nanofibers, 90° relative to the pins, and spaced by 0.1 mm over a height of 5 mm. The

arrays were characterised by these ideal standards in terms of orientation distribution, and fiber diameter.

Figure 2.4 (A) shows microscopy of the nanofibers spanning the region between pin electrodes. Fiber arrays were assessed for their order and this was quantified in terms of their normalised OD. Figure 2.4 (B) shows an SW array in the interspacing of electrodes, with a segmented overlay generated using ImageJ processing. The OD of this segment is shown in Figure 2.4 (C), with a centrepoint of approximately 90° by Lorentz fitting, which in general showed improved fitting compared with Gaussian fitting. Bowing during SNFES can cause chaotic interactions with previously deposited fibers, resulting in entanglement as well as disruption to the continuing deposition. To achieve tautly suspended nanofibers, the move between pins must occur such that the fiber is not drawn beyond breaking point while minimizing the bowing of the fiber by maximising the speed of drawing.

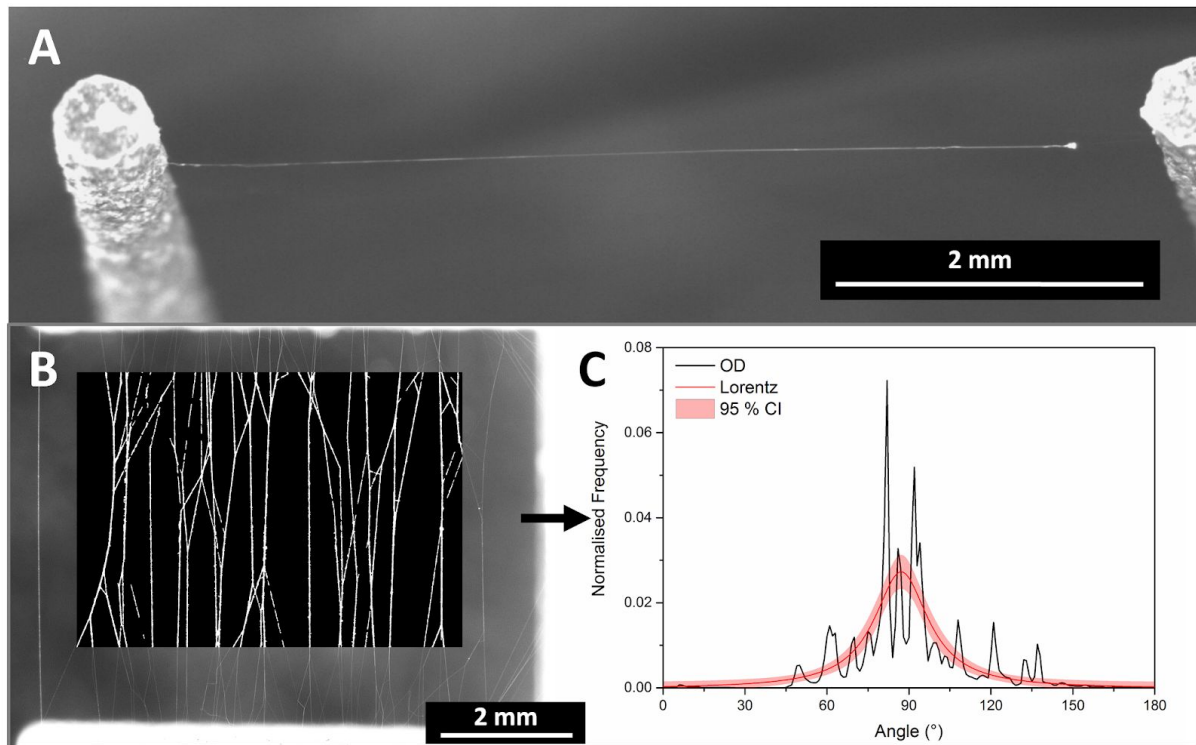


Figure 2.4. Microscopy and analysis of suspended nanofiber arrays. (A) Microscopy image of PEO fibers spanning the region between two electrodes (B) Fiber array with overlay showing a segmented view of the fibers. (C) The OD for image A, with Lorentz fitting centre point of $87.17^\circ \pm 0.83$ SE.

2.4.3. Nanofiber Suspension by Square Iteration Pattern

A second pattern, SI, was applied to demonstrate the effectiveness of the automatic systems. Figure 2.5 (A) shows a photograph of the nanofibers on the electrode. Figure 2.5 (B) shows a top down microscope image of the suspended array at 25x magnification, illustrating the inter-pin fiber alignment. A higher magnification in Figure 2.5 (C), shows the fibres tautly suspended, with polymer build-up at the corner of the pillar. The nanofibers spanning the electrodes from a side view as shown in Figure 2.5 (D), and magnified in Figure 2.5 (E), exemplify the increase in fibre density compared with the SW patterning. This also shows the clear restriction of the disposition to approximately a 2mm region, as determined by the SI pattern parameters.

The repeated SI pattern was the most simple to implement while demonstrating the automatic systems. It can be processed in any sequence as the toolpath never passes through the plane of deposited fibers (see supplementary video 3 for magnified observation of the SI pattern process).

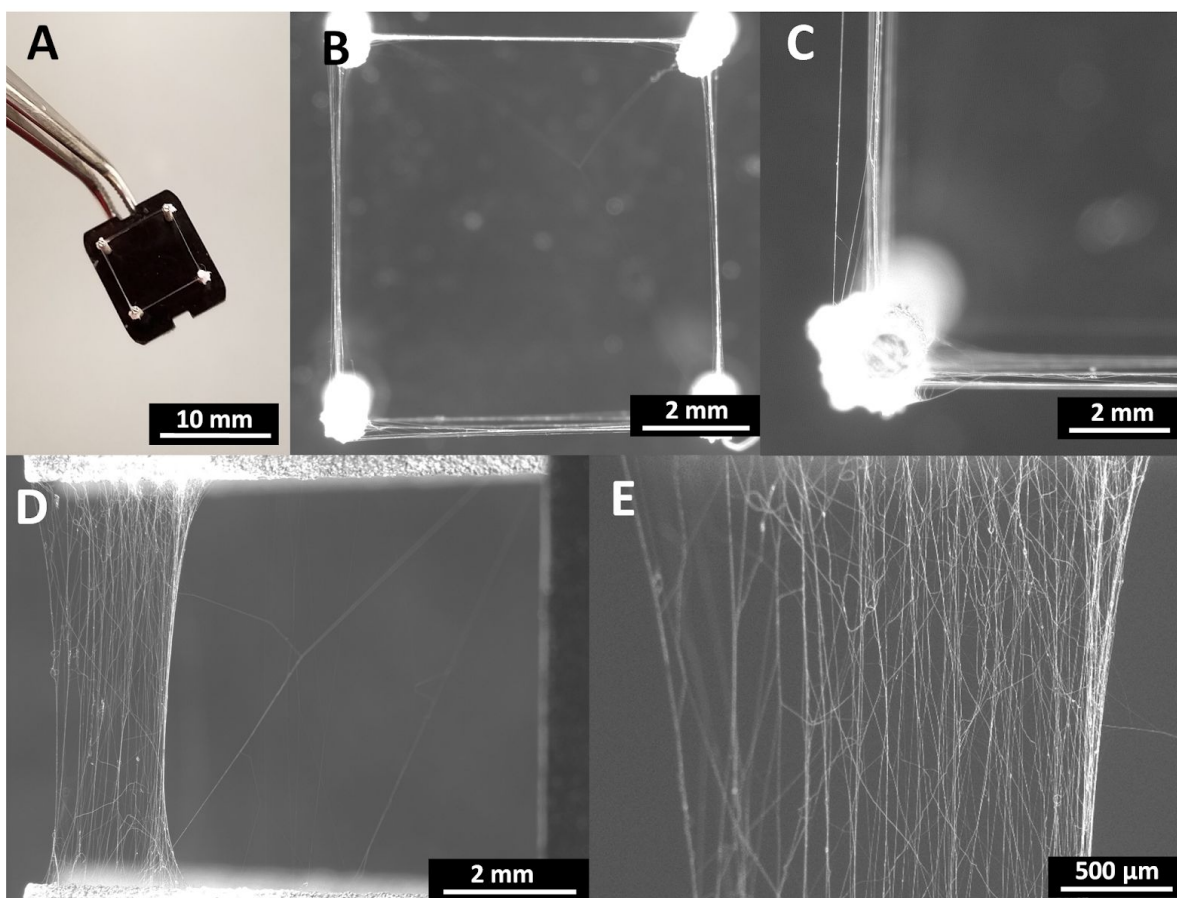


Figure 2.5. Square pattern generation of suspended nanofiber arrays. (A) Photograph of electrode supporting fibrous arrays. (B) Top down view of the fibrous array. (C) High magnification of the top of an electrode pin. (D) Side view microscopy image of mesh nanofibrous array. (E) Increased magnification of image D.

2.4.3.1. Characterizing Fiber Diameter

Fiber diameter and morphology was assessed using SEM. An example of a fiber array generated using SI patterning is shown in Figure 2.6 (A). Beneath the fibres is the carbon tape used for fixing the sample, with a pocketed surface. The fiber array is seen to splay from the electrode pillars as well as entangle and overlap. The diameter distribution histogram of this sample in Figure 2.6 (B) shows a typical sub-micron average diameter reading with mean diameter of ca. 300 nm. Figure 2.6 (C-E) shows the morphology of the fibers from several samples, exemplifying several conditions of (C) overlap, (D) smooth topography, and (E) entangled. The average diameter of each fiber is indicated showing the effect of entanglement on the overall diameter. Deposition was effective, however there remains many confounding

parameters which influence fiber morphology including residual static charge on the fiber, leading to inter-fiber attraction and entanglement. Figure 2.6 (F) shows the surface of the pillar electrode, with a considerable build-up of nanofibrous mesh layers to the right of the pillar as a consequence of 150 repeated pattern passes at multiple heights along the pillar.

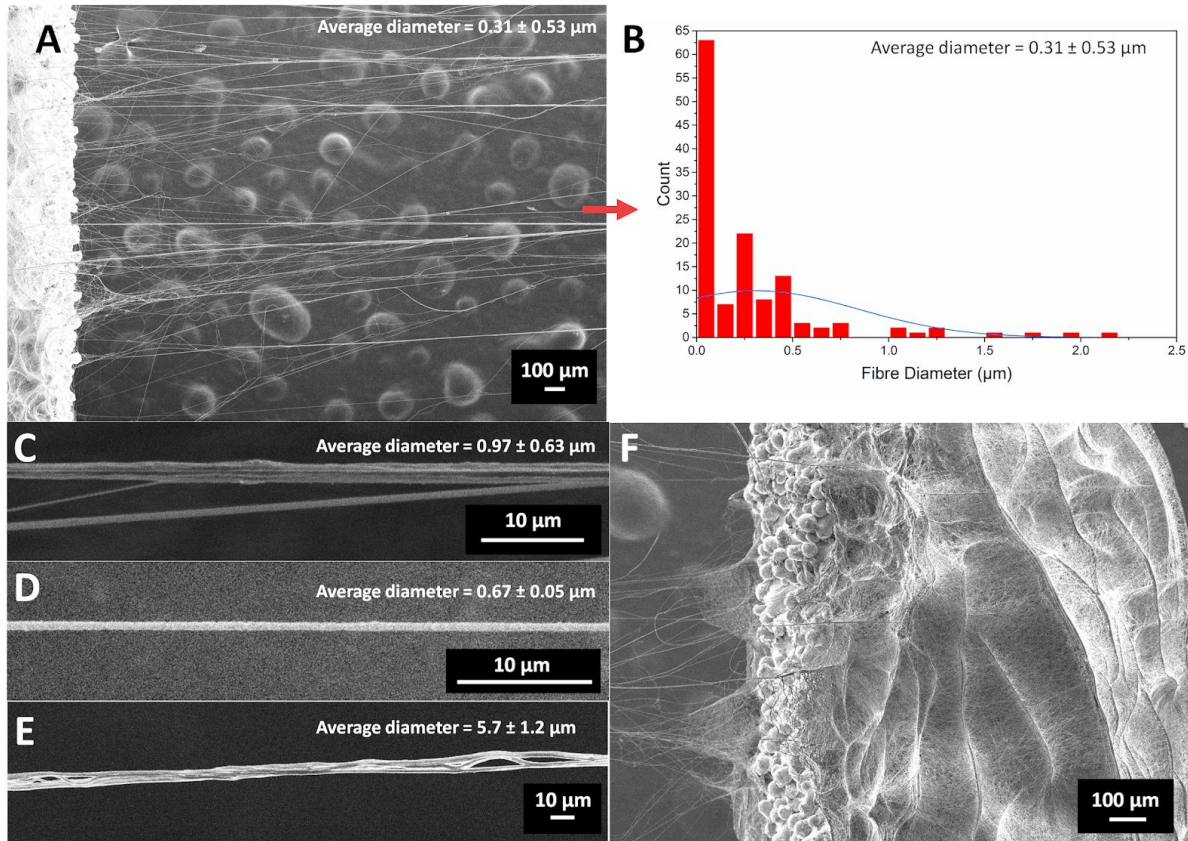


Figure 2.6. SEM and Diameter distributions. (A) Representative high magnification SEM micrograph of PEO nanofiber mesh, generated using iterated square pattern. (B) Diameter histogram of for sample A. (C-E) High magnification SEM of PEO fibers. (C) Showing crossover intertwining for sample shown in A generated using Square iteration pattern. (D) Example of desirable fiber morphology with average diameter of $0.67 \pm 0.05 \mu\text{m}$ generated using SW pattern. (E) Showing intertwined fibers generating bundle with average diameter of $5.7 \pm 1.2 \mu\text{m}$ generated using SW pattern (F) Morphology of nanofibrous build-up on a single electrode.

2.4.3.2. Discussion of Technique and Outlook

The enclosure and control of humidity had a significant effect on the outcomes of the patterning process. Humidity was found to have a dramatic effect on the success rate of fiber deposition. We define success as: observation of suspended fibers, excluding fibers connected to the electrode base. A 76% (26 out of 34 samples) success rate was found for a working distance of 1 mm within an environment with a humidity level between 30-50% RH, whereas no attempts were successful at higher humidities of 50-62% RH. This may be caused by a discrepancy in fiber drying rate. In a lower humidity environment (i.e. lower vapour pressure) the drive for water to evaporate is greater than at higher humidity. At high humidity levels fibers would remain partially in solution as they form, leading to discontinuity in jetting as well as failure to support suspension.

The mounting of the syringe pump directly onto the Z-axis reduced issues of dead volume and fluid response delay, which are associated with extended tubing passing any highly viscous polymer solution. This can be particularly important when working with high cost per weight materials, such as collagen, or hexafluoroisopropanol, a common electrospinning solvent.

NFES technical development has progressed in terms of stage precision, system automation, initiation ¹⁹⁶, high speed camera observation ⁷⁵, and through machine vision ^{197,198}. However, NFES research has rarely focused on electrode geometry, despite this being a relatively common field of investigation in conventional electrospinning research. Suspended 3D fibre mesh macrostructures have been achieved using far-field electrospinning using dumbbell ¹⁷³, mandrel ¹⁷⁴, staircase ¹⁷⁹, tracks ¹⁸⁴, and pin array ¹⁷⁶ electrode collectors. These techniques used large working distances, allowing the fibres to whip according to the principle of electrostatic equilibrium. They build layers of fibre on the collector forming macroscopic fibrous meshes, which bow due to the mechanism of deposition. In contrast, the suspension NFES technique achieves control over fibre placement in Z space via direct inter-pin deposition by working in the near-field domain (below ~10 mm).

Suspension NFES has generated nano-arrays for a number of applications^{142,160,178,181,185,199}, including sensors¹⁷⁸, microfluidics¹⁶⁰ and flexible electronics^{181,200}. Bisht et al. demonstrated the precision and accuracy of low voltage NFES by suspending nanofiber across carbon posts with diameter of 30 μm and an interspacing of 100 μm ¹⁴². However, in each case, the suspension is limited to 2D, i.e. these examples do not produce fibres beyond the platform created by their substrate, working only in a single Z plane. Liu et al. investigated another example of 3D collector use with NFES, which produced highly aligned 3D fibres upon a rotating cylindrical collector²⁰¹. However, the pattern itself does not control the structure beyond the curved surface of the collector, i.e. it cannot increase fibre density within the volume of the collector. In comparison, the technique presented here directly controls fibre spatial placement and density, by both the electrode structure and the pattern applied.

The electrodes produced for this study applied a pillar array structure to both support and draw the jetting nanofiber. With these considerations, 4-pillar electrodes could have been produced by traditional manufacturing. However, SLM achieves this production in a single part at a speed far greater than multiple element assembly. SLM allows control over all features of electrode design, reproducibly achieving feature sizes as small as 20 μm . Titanium was chosen as a robust electrode material that could remain rigid despite this small cross section. The single element electrodes' compact size allowed portability and complete analysis by SEM.

This is the first time such a technology has been applied in NFES methodology. The 4-pillar design keeps pillars at a fixed distance from one another and allows for simple and secure connection. The potential for customisation allows for variance of pin electrode configurations in terms of number, distribution, size and orientation. Future work will introduce multiple electrode design configurations which will take advantage of the rapid prototyping capabilities of SLM, producing more complex electrode structures for use in this suspension NFES technique. This process allows for the exploration of higher complexity patterning techniques using the capabilities of SLM for substrate generation to achieve greater control over fiber array structure and density. As explorations into tissue engineering constructs inexorably become more complex, the scope that SLM offers in terms of customisation and rapid manufacturability can have a positive impact upon research in this

area. Initial investigations of its use begins with controlled designs and setups, as explored in this study.

As a device, NFES is relatively contemporary, commonly with fixed functionalities, and with very few commercial devices available ²⁰². Current commercial systems lacked key features for this study and this necessitated the development of a NFES system in-house to demonstrate a new suspension NFES technique. This was achieved through instrument assembly and through software written in the high speed language C++, allowing instruments to work in concert following g-code script. The g-code writing program allowed for calibration of each pillar electrode, and each initialising pin. This was done by translating pattern values and calibration inputs into G-code sequences with interspersed cleaning routines. This allows for semi-automatic patterning, which can operate for any length of time, and once initiated it can be made more accurate with calibration routines to accommodate minor electrode differences.

The ultimate use of these suspended nanoarrays is within engineered microtissue constructs. Tissue engineering depends upon 3D architectures, and encapsulation of 3D fibrous structures has been successful in achieving a positive cellular response in many cases ^{43,203,204}. Future work will investigate the encapsulation of these fibrous arrays in gel systems such as collagen and synthetic hydrogels to achieve the interconnected porosity as well as the fibrous network structure of the ECM. Greater volume nanoarray fabrication is expected to resolve the challenges of producing hierarchical tissue constructs in 3D. The findings of this study are significant as it creates, for the first time, a suspended nanoarray in a directed manner which can be extended across multiple working planes in situ. This work highlights the potential of this new approach as a means of developing 3D scaffold nanostructures large enough for use in microtissue constructs for the medical research sector.

2.5. Conclusions

There remain challenges in redefining fabrication techniques to achieve complex 3D, hierarchical structures, while retaining nanoscale features. The layer-by-layer NFES method has several limitations when addressing these challenges, and so a suspension-based NFES

technique was developed. A semi-automated NFES system was purpose built and used to electrospin onto (a) planar silicon and (b) 3D titanium electrodes. The suspended nanofibrous arrays produced were analysed for their orientation distribution and diameter. Microscopy showed orientation of fibers to align with patterning toolpaths, which achieved an average fiber diameters below one micron.

This established the principles of this technique in demonstrating the directed 3D suspension of nanofibers. A major goal of this technique was the direct patterning in an accurate and reproducible manner. Construction of consistent nanofibrous arrays will facilitate future cell culture studies examining the effects of nanofiber arrays distribution in 3D. To achieve greater precision, further optimisation of this new technique is required, in terms of parameter and electrode variation studies. With this 3D nanofabrication technique and SLM manufactured electrodes, novel high volume nanofibrous architectures can be generated, bridging the gap of additive nanofabrication. While this study explored initial geometries, it is a necessary first step towards the exploration of complex topologies that can pave the way for generating higher order systems to match the demands of tissue engineering.

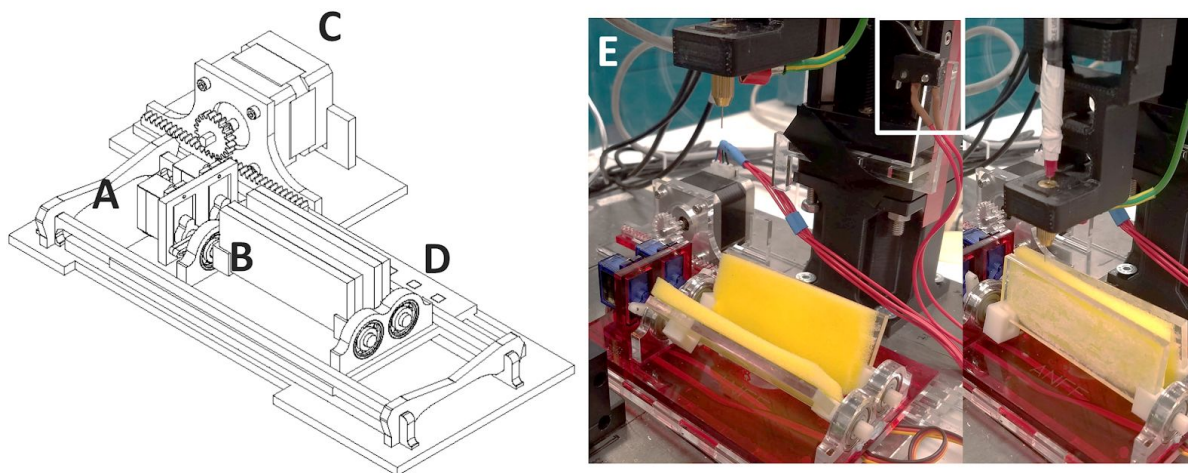
2.5.1. Acknowledgements

The authors acknowledge the financial support of the Australian Research Council (ARC) Centre of Excellence Scheme (Project CE 140100012). The ARC had no involvement in the studies design; in the collection, analysis or interpretation of data; in the writing of the report; or in the decision to submit the article for publication. The authors make no declarations of interest. The authors thank the Australian National Fabrication Facility (ANFF) for providing facilities for the fabrication of the NFES system components. The authors thank the University of Wollongong Electron Microscopy Centre (EMC) for providing SEM facilities. The authors thank Mr. Grant Barnsley for his support in the fabrication of collector electrode arrays, and thank Mr. Benjamin Filippi for his assistance in device manufacturing.

2.6. Supplementary

Section S1.

The ACD was comprised of an acrylic bed holding two servo motors rotating two paddles. These paddles were covered in polyester sponge and supported by circular bearings. When the Z-stage is lowered to a certain height it triggers an electronic switch, mounted on the stage. The switch initiates a servo driven compression motion of the paddles around the emitter tip. The tip is then retracted and cleaned by the drawing motion of the sponge. The ACD then resets the servos and moves the bed 1 mm in the Y direction. This allows an uncontaminated region of the paddles to be used in the following clean procedure. This 1 mm move is achieved by signalling a stepper motor to rotate a gear attached to a rack and pinion embedded in the ACD bed. The servos, switch and stepper motor were controlled using a microcontroller board (Arduino Mega 2560) connected to a PCB (Ultimaker v1.5.7).



Supplementary Figure 2.7. Automatic Cleaning Device. (A) Servos, (B) Paddles, (C) Stepper motor, (D) Bearings. (E) Three part cleaning routine, with switch mounted on the Z axis highlighted.

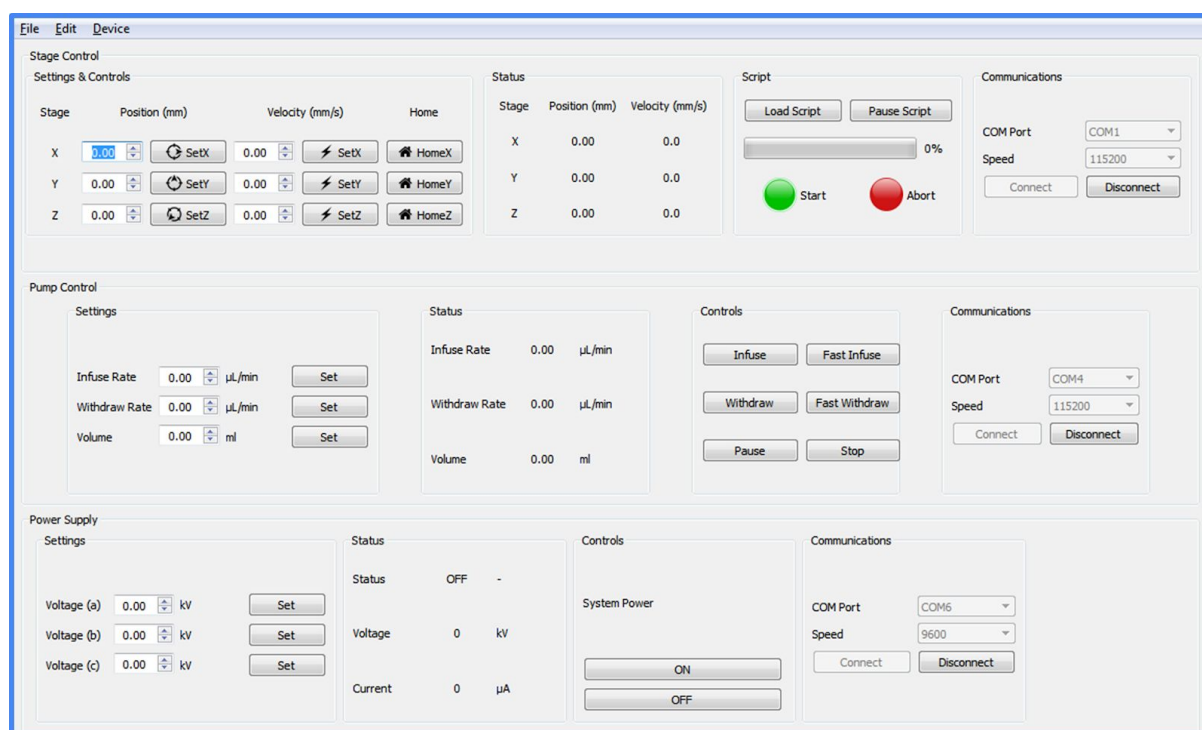


Figure 2.8. Graphic User Interface.

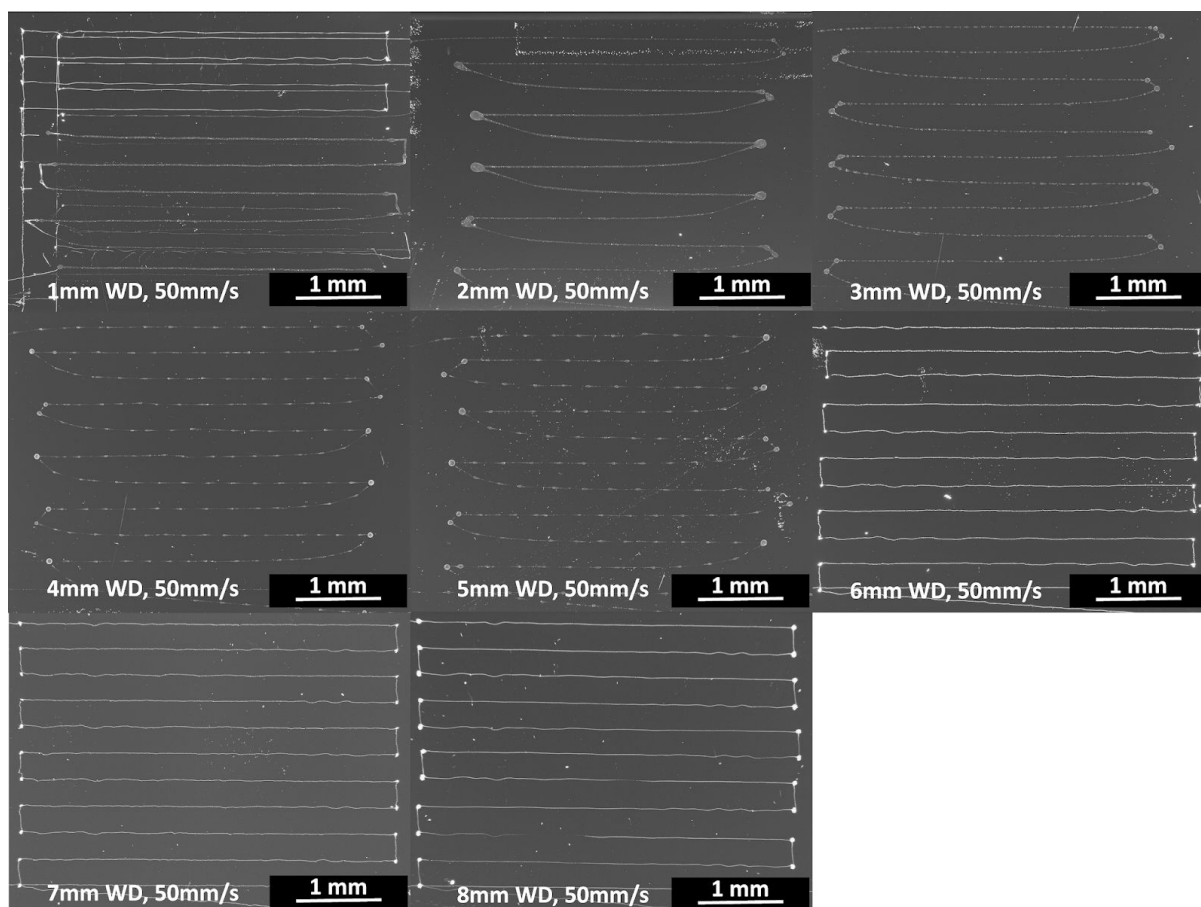


Figure 2.9. Microscopy images of 2D patterned nanofibers on silicon substrate using varied working distances.

Supplementary video 2.1. Raster pattern operation.

Supplementary video 2.2. Square iteration pattern operation.

Please find all videos at the publishers website:

<http://stacks.iop.org/NANO/30/195301/mmedia>

Chapter 3. Patterning and Process Parameter Effects in 3D Suspension Near-Field Electrospinning of Nanoarrays

This chapter has been adapted, with the author's permission, from the article - 'Patterning and Process Parameter Effects in 3D Suspension Near-Field Electrospinning of Nanoarrays', published in IOP Nanotechnology ².

Published 23rd September 2019, Volume 30, Issue 49 pages 495301-14
<https://doi.org/10.1088/1361-6528/ab3c87>

Alexander R. Nagle ^{a†}, Cormac D. Fay ^{a†}, Zhigang Xie^b, Gordon G. Wallace ^a, Xungai Wang ^{b*}, and Michael J. Higgins ^{a*}

^a ARC Centre of Excellence for Electromaterials Science, University of Wollongong, Innovation Campus, AIIM Facility, Squires Way, North Wollongong, New South Wales 2500, Australia.

^b Institute for Frontier Materials, Deakin University, Geelong, Victoria 3216, Australia.

*Corresponding Authors

[†]Contributed equally to the study

Email: mhiggins@uow.edu.au (Professor M. J. Higgins*)

Author Statement:

The work in this chapter was performed with the assistance of Dr. Cormac D. Fay, who gave editorial as well as intellectual support. All experiments and data analysis presented in this chapter were completed by the author, Alexander R. Nagle.

3.1. Abstract

The extracellular matrix (ECM) contains nanofibrous proteins and proteoglycans. Nanofabrication methods have received growing interest in recent years as means of recapitulating these elements within the ECM. Near-Field Electrospinning (NFES) is a versatile fibre deposition method, capable of layer-by-layer nano-fabrication. The maximum layer height is generally limited in layer-by-layer NFES as a consequence of electrostatic effects of the polymer at the surface, due to residual charge and polymer dielectric properties. This restricts the total volume achievable by layer-by-layer techniques. This restriction presents a complex challenge, leading to research innovations aimed at increasing patterning precision, and achieving a translation from 2D to 3D additive nanofabrication.

Here we investigated a means of achieving this translation through the use of 3D electrode substrates. This was addressed by in-house developed technology in which selective laser melt (SLM) manufactured standing pillar electrodes were combined with a direct Suspension Near-Field Electrospinning (SNFES) technique, which implements an automated platform to manoeuvre the pillar electrodes around the emitter in order to suspend fibers in the free space between the electrode support structures. In this study SNFES was used in multiple operation modes, investigating the effects of varying process parameters, as well as pattern variations, on the suspended nanoarrays. Image analysis of the nanoarrays allowed for the assessment of fiber directionality, isotropy, and diameter; identifying optimal settings to generate fibers for tissue engineering applications.

Keywords: near-field electrospinning, suspension, 3D electrode, nanoarray, nanofiber

3.2. Introduction

With recent advances in tissue engineering, the possibility of successfully regenerating irreparably damaged tissue has become viable. Microtissue constructs (MTCs) operate as tissue substitutes for biomedical interventions such as tissue reconstruction ²⁰⁵ as well as *in*

vitro models to study cellular behaviour under treatment^{206,207}. To develop MTCs, researchers have focused on imitating biological tissue structures, bioactivity, media flux and electrophysiology, which when combined promote the natural development of cells²⁰⁸. The native extracellular matrix (ECM) in human tissue is an amorphous 3D tissue embedded with fibrous networks of collagens, proteoglycans, fibronectin, laminin and peptides^{209–212}.

The interconnective porosity of the ECM allows for the mobility of cells, nutrients and waste. The fibrous network component of the ECM, imparts physical and biochemical cues necessary for cell attachment, survival and development²⁰⁹. To mimic this tissue structure, MTC scaffold porosity, pore size, and interconnectivity must be controllably fabricated in 3D. A number of research findings have demonstrated that the structure and dimension of the environment dramatically affects cellular behaviour^{210,28,213}. 3D cell culture mimics the physiological environment more effectively, resulting in improved cell survival and motility^{28,213} compared to 2D environments. Improved cytocompatibility^{30,37} and behavioral change⁴⁶ has been shown in cell culture studies comparing submicron to super-micron fibers. In the case of neural ECMs, fiber orientation has been shown to guide neurite and neural cell alignment^{214 215,216} and migration along fibers through contact guidance *in vitro*^{47–50} as well as improve neural recovery *in vivo*²¹⁷. These findings support the use of 3D structured nanofibrous components in MTCs.

To emulate the protein/proteoglycan networks, nanofabrication techniques have received extensive technological investment and research. Solution based far-field electrospinning (FFES) is a technique capable of producing ultrafine polymer fibrous meshes, both aligned and randomly oriented. FFES can work using a wide variety of materials, has a simple set-up and can operate at room temperature^{113,116,192}. Due to its similarity to the native tissue networks, the fibrous meshes produced by FFES have been investigated as an ECM mimicking structure through cell viability experiments^{30,38,218–223}. However, conventional FFES lacks fine control of fiber deposition, where electrostatically driven bending instabilities lead FFES to produce disordered fibrous layers¹³⁶. This lack of spatial control produces meshes with bulk pore sizes that are too narrow to allow for cell infiltration⁴⁸.

Within the last ten years, electrospinning technology has advanced, allowing for the direct patterning of nanofibers. Typically termed near-field electrospinning (NFES) or electrohydrodynamic direct writing ²²⁴, these technologies have allowed directly written nanofibrous structures to be generated in designed patterns. This is achieved by reducing the working distance and applied voltage, precluding the jetting instability inherent to FFES. In this regime the control of fiber placement and morphology is achieved ¹³⁹. NFES can generate 3D structures by direct layer-by-layer deposition ^{40,146,167,171,172,194} and this technique has allowed for the fabrication of 3D microfiber scaffolds for cell culture research in a number of studies ^{40,156,167}.

In our previous work, we developed a suspension near-field electrospinning (SNFES) instrument, which enabled fabrication of suspended fibrous nanoarrays between the pillars of 3D electrodes ¹. In this study, we investigate the effects of varying process parameters, such as speed, working distance, tip voltage, iteration and pattern variation, on 3D fiber arrays produced by the SNFES. The outcomes were measured by a number of metrics, for example, fiber array orientation and diameter distribution. In particular, the patterning results show that the SNFES method is effective in the production of multiple array patterns.

3.3. Materials and Methods

3.3.1. Materials

3.3.1.1. Materials

Titanium Grade 5 (Ti 6Al-4V) powder (spherical particle size $< 63\ \mu\text{m}$) was purchased from TLS Technik GmbH (Bitterfeld, Germany). Poly(ethylene oxide) (PEO) powder (average M_v : 200,000) was purchased from Sigma-Aldrich Co. (Sydney, Australia). PEO was dissolved at various concentrations (8, 11, 14, 17, 20 wt%) in water/ethanol (3:2) using a magnetic stirring bar for 1 hr to reach homogeneity.

3.3.1.2. Apparatus

Figure 3.1 (A-I) presents the schematic of the instrument assembly. Two linear motorised stages (A-LSQ150B, Zaber) were overlaid perpendicular to each other (Figure 3.1 (B), (D)) to enable X-Y directional movement of the platform. A third stage (Figure 3.1 (G)) held a syringe pump (UMP3, World Precision Instruments Inc.) (Figure 3.1 (F)) above the working area, moving vertically in the Z-axis. The stages, the syringe pump and the high voltage power supply were controlled by in-house developed software using the Qt software development kit (The Qt Company, Norway), written in C++ for high speed command execution. To allow for repeatable experiment operations and compatibility with 3D slicer programs, the stage system command line interface was programmed with an inline translator to enable the use of standard G-code. This system is described in greater detail in previous work¹.

A 1 mL syringe was mounted on the syringe pump, with a blunt tipped stainless steel needle (0.25 mm inner diameter, Gauge 25). The needle was locked in place by a drill chuck, and grounded via ring connector. An in-house developed automatic cleaning device was placed beneath the tip. In the event of the tip moving within range of the cleaning paddles, a limit switch is triggered by the Z stage, and two servos compress the paddles on the tip. The tip is then retracted, drawing any residue from the emitter. Prolonged operation was achieved by periodic cleaning, preventing solution drying at the outlet and allowed the enclosure to remain closed during operation. The NFES system was placed within a transparent acrylic

enclosure for safety as well as to enable humidity control via a dehumidified compressed air line. All experiments were conducted at low humidity (ca. 19 %RH), to prevent instabilities in NFES deposition. Humidity was measured using a temperature and humidity data logger (XC0424).

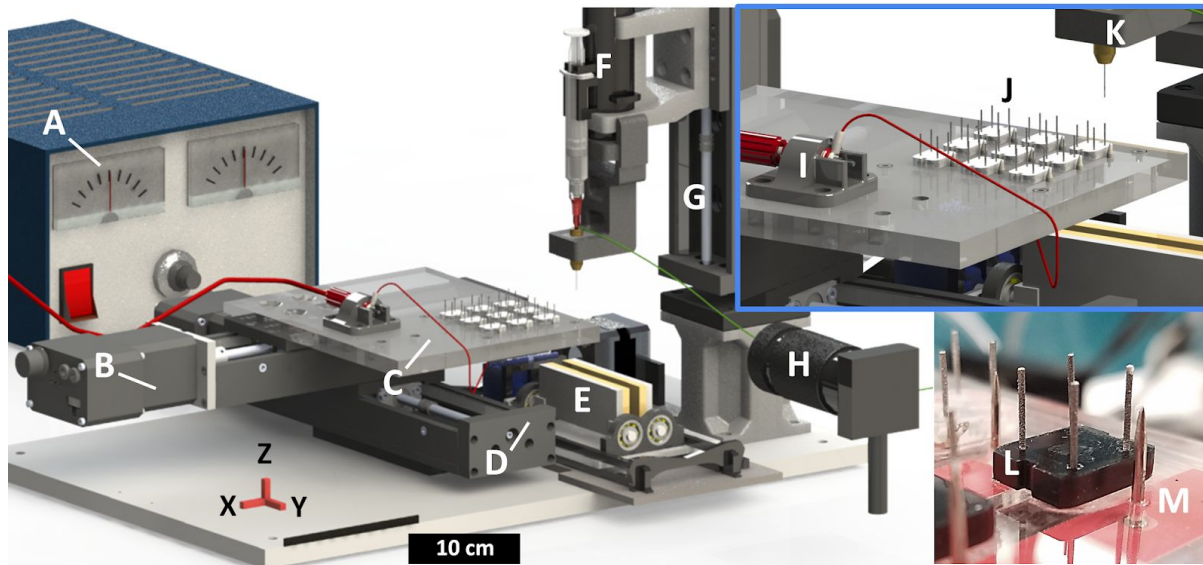


Figure 3.1. System Schematic. (A) High Voltage Power Supply; (B) X-Stage; (C) Platform; (D) Y- Stage; (E) Automatic Cleaning Device; (F) Syringe pump; (G) Z-Stage; (H) Camera; (I) High voltage connection point; (J) Electrode array; (K) Blunt tipped Needle. (L) 4-pillar electrode with black cap mounted in the platform. (M) Initiation pin.

3.3.1.3. Electrode Fabrication and Mounting

The titanium electrodes were manufactured using a SLM-50 (Realiser) from grade 5 titanium powder (Ti 6Al-4V). Figure 3.1 (L) shows the 4 pillar electrode embedded in the system platform. Electrode pillars were 7.07 mm separated along the horizontal/vertical and 10 mm along the diagonal. Insulating acrylic covers were attached over the base of the electrodes to ensure that the electric field lines emanated purely from electrode pillars to the syringe tip (Figure 3.1 (L)). The electrode design consisted of four vertical pillars, 700 μm in diameter, 10 mm tall on an x-shaped base, with two connection pins beneath the base (see Figure 3.2 (a)). On the X stage, an acrylic platform was attached to position the collecting electrodes (Figure 3.1 (C, J)). The connection pins were plugged into three female 40 way IDC line

socket connectors, firmly positioning the electrodes in place. The PCB header was connected to a high voltage connection point (Figure 3.1 (I)), which led to a positive bias high voltage power supply (ES30, Gamma HV) (Figure 3.1 (A)).

3.3.2. Suspended Nanoarray Fabrication

3.3.2.1. Parameter Variation Study

PEO was chosen to test this suspension NFES method as this polymer has been extensively used in testing novel electrospinning methods, due to its simple water solubility. This eliminates the requirement of more volatile solvents typically applied with other polymers, reducing the risk of chemical burn to the user, and simplifying the procedure. When using highly volatile solvents the evaporation rate must be decreased by adding a co-solvent to avoid excessive drying. This solution's relatively low evaporation rate allows for greater timeframes in which to operate before nozzle tip obstruction by dried polymer. This is beneficial to NFES operation, particularly in the iteration studies conducted herein.

To investigate the effects of process parameters on fibre arrays, a raster (*R*) inter-pin pattern was selected. The two upright working planes were parallel to the plane created by the pillars (see Figure 3.2) at a working distance (*WD*), defined as the minimum distance between the emitter tip surface and the surface of the target pillars. Within the working planes, the tip was raised in steps of 100 μm in the *Z*-axis for each horizontal move across the *X-Y* plane, creating a programmed raster pattern 7 mm wide, with a total height of 5 mm.

To calibrate the position of the syringe tip to the pillars, the stage was moved to align one pillar below the tip, and the tip was lowered until contact with the pillar's apex. G-code script was then generated from this calibration using a spreadsheet program (Google Sheets). The solution extrusion rate was held constant 3 nl.s^{-1} to maintain the solution droplet. To better understand the patterning process, readers may refer to the Video 1 in the supplementary section which is available online.

Electrospinning requires that the jet be initiated, and this can be done in two established ways. The first applies a critical voltage, exerting a high electrostatic force on the droplet surface,

which overcomes its surface tension. The second method exerts a mechanical initiation by means of disruption of the droplet surface ^{138,145}. Mechanical initiation was used in this study, as there is a greater risk of arcing at the low *WD* applied. In this technique, initiation involved contacting the solution droplet on the apex of a sharp pointed stainless steel tip, embedded in the surface of the platform (see Figure 3.1 M), immediately followed by the intended pattern. This was achieved automatically, following an initial manually handled calibration.

In order to determine the optimal parameters for PEO in SNFES, two orthogonal experiment groups were examined, investigating four treatment parameters. In the first group (T1) maximum speed (S_{max}) was varied while *WD* was varied as described in table 3.1. In this orthogonal group, 1.6 kV was applied using a 14 wt% PEO solution. In the second group (T2) the applied voltage and PEO solution concentration were varied as described in table 3.2. A constant S_{max} of 50 mm.s⁻¹ and a *WD* of 1 mm were applied. For each unique setting, samples were reproduced three times or until a suitable number of successful samples were generated ($n \geq 4$).

Table 3.1. Orthogonal sample grouping T1. Constants 1.6kV and 14 wt% PEO.

S_{max}	50	150	250	50	150	250	50	150	250
<i>WD</i>	1			1.5			2		

Table 3.2. Orthogonal sample grouping T2. Constants S_{max} of 50mm.s⁻¹ and *WD* of 1 mm

Voltage	1.2	1.6	2	1.6	1.2	1.4	1.6	1.8	2	1.6	1.2	1.6	2
Concentration	8			11	14					17	20		

3.3.2.2. Iteration Study

To investigate the effects of multiple repeated patterning, a square iteration (S_i) pattern was applied (see Figure 3.2 (b-c)). This follows a square path around the four pillars for a certain number of laps, followed by a move upwards along the Z-axis. A total of nineteen sequential Z-axis positions were used, each separated by 0.1 mm, resulting in a total height of 1.9 mm.

In addition, this study acts to stress test the technique, to ensure optimal automation over an extended time period. To achieve reproducibility, a semi-automatic process was necessary. This process involved a looping sequence of cleaning, to mitigate discontinuity of ejection from the droplet, which can be caused by the solution drying at the outlet as well as contamination of the tip by particulate accumulation (among other interruptive events). The cleaning process was followed by mechanical initiation and *Si* patterning. This cleaning sequence was performed at regular intervals, multiple times proportional to the pattern iteration value. An example of the patterning operation is shown in Video 1

The number of pattern iterations (i.e. laps, circuits) performed for every *Z* position was varied as a group of independent samples: of 1, 15, 60, 105 and 150 iterations. The applied voltage (1.6 kV), and PEO concentration (14 wt%) were held constant in these experiments. The solution extrusion rate was kept constant, i.e. 3 nl.s⁻¹. The *WD* was varied at 1 and 1.5 mm, and samples were generated in quadruplicate for each unique setting (*n* = 4).

3.3.2.3. Patterning Variation

Fibers of PEO were suspended between electrode pillars using a variety of pattern types to investigate the versatility of the technique, and test the effect of these patterns on the array alignment, fibre density, diameter and morphology. Figure 3.2 (b) illustrates the toolpaths of these patterns. The first pattern is the previously described *Si* pattern. The second pattern denoted: \, creates a circuit lapping around two diagonal pins. The third pattern combines the \ pattern and the *Si* pattern (denoted: \Si). The fourth pattern combines the \ pattern followed by its counterpart / around alternate pins (denoted \ /). This pattern operates within distinct height regions for each pattern to avoid collision of the tip with the deposited structure. Each pattern was repeated 15 times (iterations) per *Z* position, moving a total height of 1.9 mm. These patterns were performed at an *S*_{max} of 50 and 250 mm.s⁻¹ in separate groups (*n*>4). The applied voltage (1.6kV), *WD* (1 mm) and PEO concentration (14% wt) were held constant. Solution extrusion rate was maintained at 3 nl.s⁻¹.

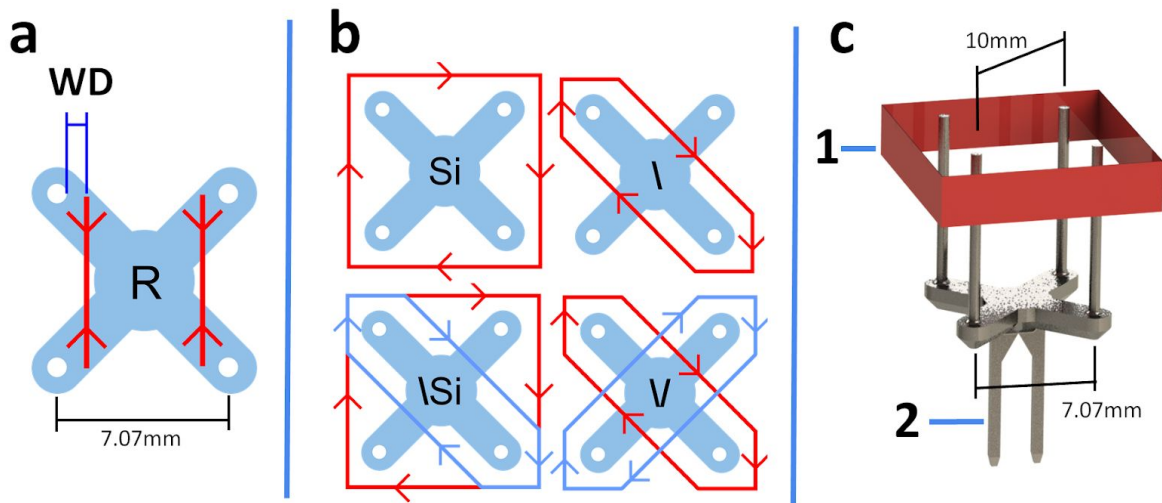


Figure 3.2. Pattern Variations. (a) R pattern tool-path (red) with working distance (Wd) shown. Each path moves back and forth at both positions. (b) Pattern tool-path variations with identifiers and routes (red and blue). (b) Pattern variations with identifiers and tool-paths (red and blue). (c) 3D CAD illustration of the Si pattern (1), showing the electrode connection pins (2).

3.3.3. Characterisation

3.3.3.1. Rheological Analysis

The polymer solutions of each concentration were analysed using a rheometer (ARG2, TA Instruments, Delaware, USA), measuring the viscosity as a function of shear rate, from 0.01 to 100 s⁻¹ in a rotating cone and plate system.

3.3.3.2. Light Microscopy

3D fiber arrays were imaged by light microscopy (M205A, Leica Microsystems, Wetzlar, Germany) observing orthogonal perspectives of each array plane (see article ¹ for additional details).

3.3.3.3. Scanning Electron Microscopy

The morphology of each nanoarray generated was investigated by scanning electron microscopy (SEM), with the exception of samples generated in section 2.2.3 Patterning Variation. Four pillar electrodes were mounted on stainless steel stubs by carbon tape, and SEM imaging was carried out on the entire electrode. SEM was performed using a JSM-7500FA (JEOL Ltd.) operating at 10 kV, and 5 mA. For each sample, a minimum of five high-magnification images ($\sim 2000\times$) were taken of fibres comprising the array ($n > 5$).

3.3.3.4. Image Analysis

Fiber arrays imaged by light microscopy were assessed for their order in terms of their distribution. This was quantified in terms of their normalised orientation distribution (OD), and estimated fibre number. The normalised OD is analogous to a probability density function of fiber orientation. Microscope images were converted to binary segmented images and semi-automatically analysed using ‘Diameter J’²²⁵, a plugin of image processing software ImageJ (National Institutes of Health, USA). This plugin applies the OrientationJ module to determine the OD of the fibers as well as producing axially thinned representations of the fibre arrays²²⁶. Refer to supplementary Figure 3.11 for an illustration of this process. To allow the comparison of distributions, we calculated the preferred orientation, defined by the distribution centroid (Φ_c)²²⁷ defined in equation 1 as:

$$\Phi_c = \frac{\sum_{\phi = \phi_{min}}^{\phi_{min} + 180^\circ} \left[(\phi - \phi_{min}) \frac{I(\phi) + I(\phi - 1)}{2} \right]}{\sum_{\phi = \phi_{min}}^{\phi_{min} + 180^\circ} \left[\frac{I(\phi) + I(\phi - 1)}{2} \right]} \quad (1)$$

Where ϕ_c is the distribution centroid, ϕ is the angle, and ϕ_{min} defines the starting position, 0° in this case, and thus the range of 180 degrees of analysis. Furthermore, we define the distribution skew as $\Phi_s = \Phi_p - \Phi_c$, where Φ_p is the maximum peak orientation obtained by peak analysis (i.e. global maximum). The greater the degree of Φ_s divergence from a symmetrical distribution the greater the likelihood the fiber OD is not a single population. All

distribution fitting, centroid calculations and peak analysis was conducted using OriginPro 2015 software (OriginLab Corp.). The code for centroid calculation is shown in supplementary section 1.

To indicate the degree of fibre alignment we describe the width of the distribution using the Orientation Index (OI) ^{225,227,228}. The OI is defined as the number of degrees expanded from Φ_c symmetrically in both clockwise and anticlockwise directions, which contains 50% of the total normalised frequencies (see Figure 3.3 (b) for an example). From this we can derive the intuitive Normalised Orientation Index (NOI): where $NOI = \frac{(90^\circ - OI)}{90^\circ} \times 100$, $NOI \in [0, 100]$. The NOI values of 0% (binary peak, lattice) or 100% (single peak, array), indicate highly aligned fibres, whereas values c.a. 50% indicate a random fiber distribution.

To estimate the number of fibres per sample, the axially thinned images of each array, generated by DiameterJ, were sectioned by four horizontal lines equally spaced across each image. Each line's pixel profile was measured and the number of fibres crossing the line were counted. The four counts were averaged to give the approximate fibre number in each sample. From SEM micrographs the diameters of the fibers were measured using ImageJ tools. Measurements of fiber diameter were performed at ten random locations in each micrograph manually, with a minimum of five images per sample to investigate diameter variability. This method is similar to one used in the literature ²²⁹. In several samples for the purposes of illustration SEM images were analysed using the DiameterJ function giving the frequency histogram of the diameter in the image.

To estimate the number of fiber intersections, microscopy images of the arrays were analysed. Images were prepared by threshold binarising and conversion to axially thinned fibers by ImageJ functions. Branch pruning by length was performed via a Beanshell script running in ImageJ, using a threshold of 150 pixels in length which equals ca. 0.41 μm , removing smaller fibrils splaying from the main fibers as well as image artifacts of skeletonizing the binary

image. This was then followed by the analyse skeleton function of ImageJ, outputting intersection number. This method was applied for all samples using the raster type pattern.

3.3.3.5. Statistical Analysis

To evaluate the independent distributions, a two-sample t test was used to determine the significant difference between groups. Mean fibre number (Section 2.2.3 Patterning Variation) were analysed to determine significance of variation between means. The means were subjected to the Shapiro-Wilk normality test, Levene's test of homogeneity of variance, and univariate ANOVA with the Games-Howell test. All calculations were performed using SPSS Statistics 23 (IBM, USA).

3.4. Results and Discussion

3.4.1. Effects of Process Parameters on Nanoarrays

In electrospinning there are many effective parameters of control, which can be broadly grouped into three categories: environmental, solution and process parameters^{108,145,187}. Additionally, certain regimes of electrospinning can be classified: spraying²³⁰, beading^{139,231}, continuous, and intermittent¹⁹⁸. These regimes define the effective parameter domains of continuous electrospinning. These parameters are interdependent when predicting a continuous electrospinning parameter group. In this study, relative humidity and flow rate were fixed, while varying the most readily controllable processes in two treatment groups, T1 and T2 (see Tables 3.1 and 3.2). The parameter range was constrained by the physical system (max speed, polymer concentration), as well as by dielectric breakdown (voltage, working distance). Air begins to break down when the electric field exceeds approximately 3 kV.mm⁻¹. NFES operation discontinues as the arcing causes rapid drying, and solidification of polymer at the emitter outlet, as well as disrupting communication with system instruments.

The minimum integer working distance which could be accurately applied was 1 mm, given the accuracy of calibration and the varying degree of angular divergence of both electrode and emitter from vertically aligned. The maximum working distance was defined by what had previously been found to be effective¹, where the working distance is typically no greater

than 10 mm for solution based NFES. Within these experiments voltages above 2 kV using a working distance of 1 mm were found to commonly result in dielectric breakdown. This defined the upper limit of voltage operation. The lower voltage limit was defined by the success in coherent jetting, and this varied for differing concentrations. 1.2 kV was found to be the minimum effective voltage across all sample concentrations used, and this defined the domain of effective operation for applied voltages, i.e. between 1.2 and 2 kV.

3.4.1.1. Effect of Process Parameters on Nanoarray Distribution

The R pattern would ideally produce highly aligned, parallel, equally spaced fibres in a precise number according to the design. We can quantitatively compare the precision between treatments in terms of the NOI (i.e. variance) and the global maximum peak information of each OD. The ideal distribution would have a global maximum peak at 90° (relative to the pillars), and an NOI of 100%. The first treatment group (T1) varied the working distance as well as the S_{\max} in a 3 level orthogonal experiment. The second group (T2) varied the voltage and the PEO concentration in a separate 3 level orthogonal experiment. Figure 3.3 (a) shows an example of a suspended array and its corresponding OD (Figure 3.3 (b)). Lorentz fitting of this OD showed a centre point of $87.2^\circ \pm 0.9$, with full width at half maximum (FWHM) value of $24.2^\circ \pm 3.1$. This example is accurate (ca. 90° orientated), yet imprecise (broad OD distribution, NOI = 80%).

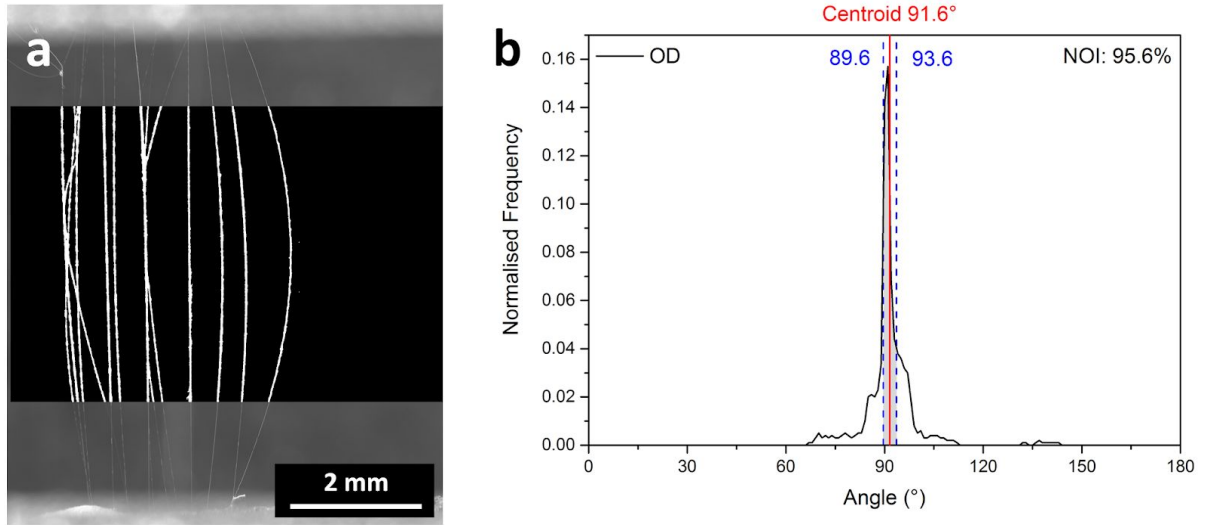


Figure 3.3. R patterned nanofibrous arrays. (a) Microscopy image of PEO fibre array generated using the R pattern. The overlay shows a binary segmented view of the fibres, generated by image processing. (b) The extracted OD for image A, with red line indicating a centroid of 91.6°. Dashed blue lines indicate the boundaries of the OI region (grey). The OI was calculated from the OD without the use of fitting distribution models.

Figure 3.4 (a) shows a box plot of global maximum angle (red), and NOI (blue) for each OD as a function of process parameters S_{\max} and WD . The distributions of the maxima are bounded in the region of $90^\circ \pm 5^\circ$, while NOI is above 80% with a few exceptions. This accuracy and precision information indicates 90° aligned fibre arrays, and in particular a WD of 2 mm achieved the most accurate global orientations with correspondingly high NOI. In comparison, Figure 3.4 (b) shows a greater variability in accuracy and precision in orientation with changing voltage and concentration. The NOI often reaches below 80%, with the greatest decline in samples produced using 20 wt% PEO, indicating poor array alignment. The global maximum peaks deviate from 90° in the sample generated using concentrations of 20% wt and particularly in 1.2 kV, 8 wt% samples.

The minimum working distance used here of 1 mm, was restricted by dielectric breakdown arcing effects. This may be overcome as in 2D NFES, where working distance is as low as *ca.* 0.2 mm, by reducing voltage and by working within an enabling solution parameter range.

If this intervention does not readily prevent dielectric breakdown, it may be necessary to work in a sealed controlled environment to manipulate the dielectric strength of air. This can be achieved in a number of ways using the principles of Paschen's Law. In air dielectric strength becomes exponentially higher as electrodes approach contact, higher atmospheric pressure leads to an increase in the dielectric strength and at extremely low pressures the dielectric strength is much greater. Reducing absolute humidity would also improve the dielectric strength of air. These untested interventions present a number of challenges in their implementation for SNFES, and may have unpredictable effects which will need to be investigated as part of future research.

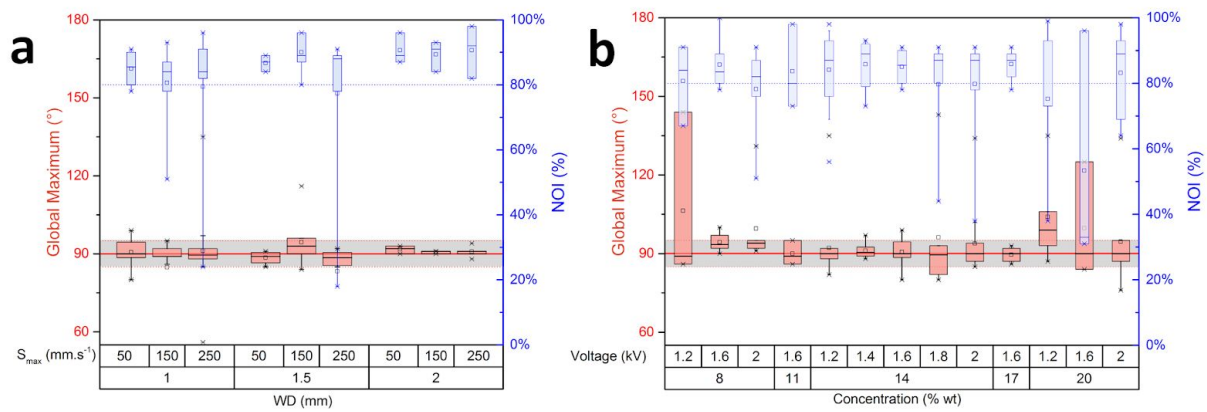


Figure 3.4. Orientation distribution statistics across varying process parameters. (a) Combined boxplots of the global maximum angle and NOI across samples generated by varying parameters of S_{max} and working distance. (b) Combined boxplots of the global maximum angle and NOI across samples generated by varying parameters of voltage and concentration. The dashed red lines bound the angles 85° to 95°. The dashed blue lines indicate 80-100% NOI.

3.4.1.2. Effect of Process Parameters on Nanoarray Fiber Diameter

The degree of success and conversely discontinuity in patterning is estimated in terms of the fibre density. We estimate the number of fibres in each sample by analysing microscope images. Fibres were first thinned to be one pixel in diameter, using DiameterJ, a plugin of

ImageJ software. This applies both an axial thinning algorithm, developed by Zhang and Suen²³², and a Voronoi tessellation algorithm, separately, then averages the result. By counting the pixels crossing four horizontal lines and taking the average, we estimate the number of fibres in the array. This was done semi-automatically using an ImageJ macro function.

Bowing during deposition can cause chaotic interactions with deposited fibers, resulting in entanglement as well as disruption to the continuity of deposition. The fiber must not be drawn beyond breaking point while minimizing the bowing of the fiber through more rapid drawing. The speeds of 50, 150 and 250 mm.s⁻¹ were found not to significantly influence the fibre number as predicted by this hypothetical breaking point disruption. This may be a case where critical breaking point speeds exceed the limitations of the system's max speed (250 mm.s⁻¹). Fibre number for these parameters are shown in supplementary Figure 3.14.

Figure 3.5 (a-b) shows the mean diameter values for samples created in group T2 showing no clear trend with respect to concentration and voltage. Conventional electrospinning research has shown that the effect(s) of voltage, concentration, working distance and speed has a typically non-linear relationship with fibre diameter^{54,78}, with the sensitivity of the output to process parameters described in work by Costolo et al.⁷⁸. For the purposes of MTC fabrication, fiber diameter is preferably below ca. 700 nm^{30,3746}. Increased polymer concentration (see Figure 3.5 (a)) led to a pronounced variability in sample fibre diameter and variance, exhibiting the greatest population variance at 20% wt PEO in solution, with greatest mean diameter, $1.19 \pm 0.99 \mu\text{m}$ across all parameters.

From these results, samples made using 1.2 kV, at working distance of 1 mm, at S_{max} 50 mm.s⁻¹ using 14 wt% solution were found to have the lowest mean diameter of $0.49 \pm 0.21 \mu\text{m}$ (Figure 3.5 (b)), marginally lower than 8 wt% solution at 1.6 kV. Figure 3.5 (c) shows representative SEM micrographs of the fibers, each an example of the mean diameter for their associated voltage. For additional information on findings involving working distance diameter variation and fiber number refer to supplementary Figure 3.14.

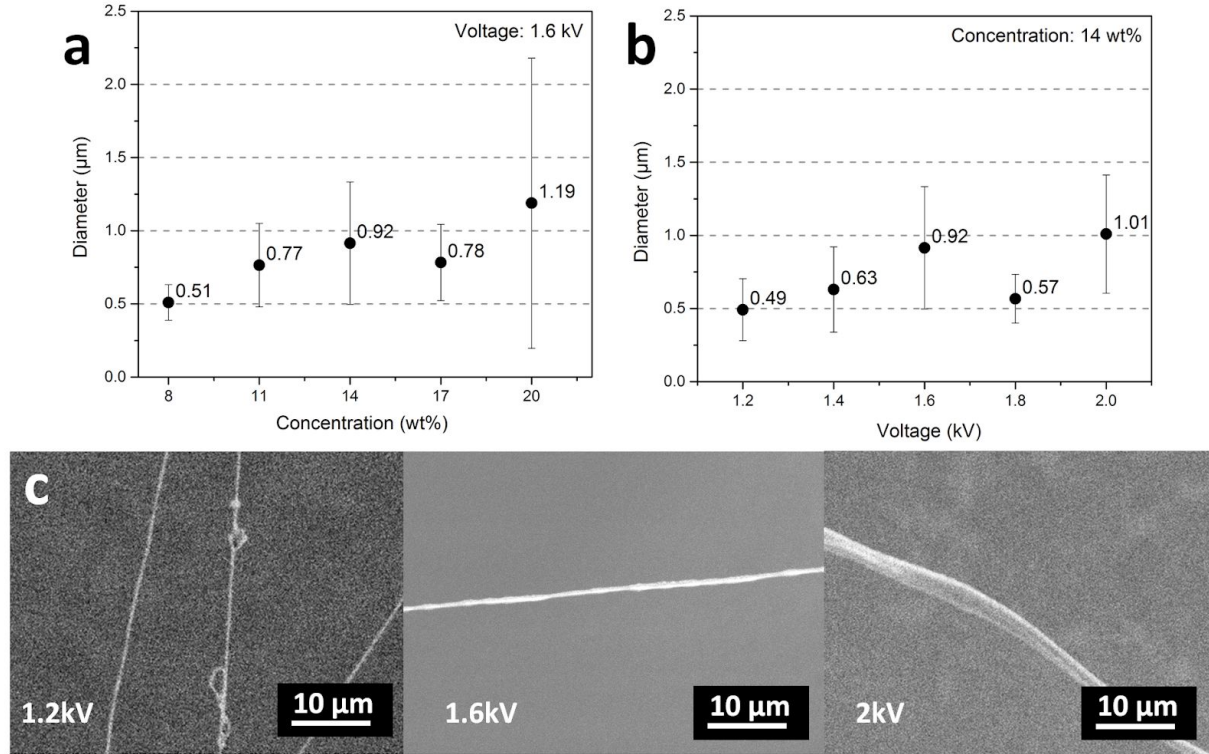


Figure 3.5. Fibre number and diameter as a function of process parameters. (a) Fibre diameter as a function of concentration and (b) voltage. (c) SEM images showing the morphology of fibres generated at different voltages. In the 2 kV case, the image illustrates the surface morphology of the fiber, showing a twisted ribbon structure.

3.4.2. Effect of Pattern Iteration on Fibre Number and Diameter

Fibrous mesh arrays were generated using the Si pattern, applying a range of iterations. Figure 3.6 (a) shows the nanostructure suspended between two pillar electrodes, produced using an iteration of 105. The inset shows a magnified view of the fibres, showing an overlapping web structure. Figure 3.6 (b) shows the build-up of nanofiber at the corner of a pillar electrode. The stage must reduce speed in the corners of the Si tool-path in order to manoeuvre each pillar around the emitter tip. The disproportionate time the emitter is in proximity of these regions causes this build-up, producing complex striation structures shown magnified in Figure 3.6 (c).

A plot of the average fiber number as a function of iteration is shown in Figure 3.6 (d), grouped by working distance. As the iteration value increases, we observe a phase exponential increase of the means in both working distance groups (1 mm, 1.5mm). The data

points indicated an exponential trend and fitting was further applied to determine the R^2 coefficients. Fitted trends of the means were of the form: $y = y_0 + Ae^{-x/t}$, where y is the average fiber number, x is the iteration, y_0 is the offset (or the plateau y value, the maximum fibers achievable at large iteration), A is the amplitude prefactor for the exponential, and t is the constant decay factor. The fittings achieved R^2 values of 0.996 (1.5 mm *WD*), and 0.998 (1 mm *WD*). y_0 is the plateau value, indicating the maximum fibers achievable based on this parameter setting. t is the decay factor and describes the ‘speed’ of decay, or the amount of iterations needed to reach the plateau of fibers, which relates to the inhibitory effect magnitude change with iteration. The relative change in fibre number declines at higher iterations. We attribute this effect to the established principle of decreasing electrospinning force as polymer mass at the collector increases¹³⁶. This leads to increased inhibition of the electric field, lessening the drawing force on the polymer jet and inhibiting further ejection.

The suspended fibrous mesh shown in Figure 3.6 (e) was analysed for the fiber diameter using ImageJ plugin: DiameterJ. The normalised histogram of the fiber diameter in Figure 3.6 (e) is shown in Figure 3.6 (f), with a log-normal distribution fitting (red), peaking at ca. 0.41 μm . Figure 3.6 (g) shows the plot of mean diameter of each sample as a function of changing iteration and working distance. For working distance 1.5 mm, the relative increase in fibre diameter and standard deviation at high iterations of 105 and 150, can be explained by fibre overlapping, which generates bundled and fused fibers. This bundling combines several fibers (see supplementary section Figure 3.15) increasing the measured diameter as well as expanding the variability of fiber diameter, i.e. increasing the standard deviation. This effect is not seen in the 1 mm working distance samples, and it is not clear if there is any preventative effect or if bundling is simply a statistical occurrence.

The electric field in the SNFES process has a number of confounding effects. During patterning it varies in intensity and vector strength during the toolpath excursion. Supplementary section 5.4 and supplementary videos 2 and 3, shows the field change as the emitter is passed by the pillars in both Raster and Square iteration patterning. This was done with modelling software Comsol Multiphysics. Further to this is that jetting fiber has some

cascade effects on its successor and is affected by its predecessor as well. After much deposition, this too has an effect on fiber ejection, inhibiting and ultimately limiting the ejection of fiber.

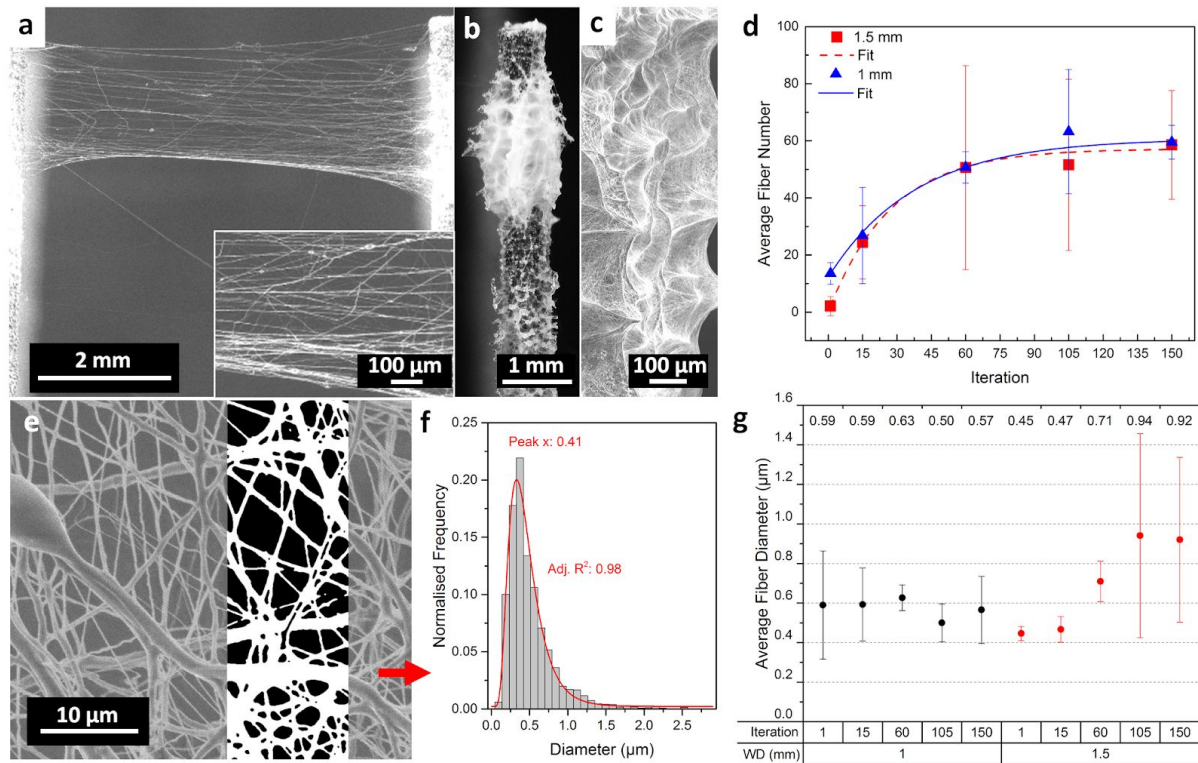


Figure 3.6. Iteration studies. (a) Microscopy of fibre array produced using 105 iterations, with high magnification inset. (b) Single electrode pillar showing fibrous build-up at the surface due to high iteration pattern deposition, with (c) SEM micrograph exhibiting the structure of the fibrous build-up. (d) Plot of the average fiber number as a function of iteration. Fitted trends of the means were of the form: $y = y_0 + Ae^{-x/t}$, where y is the average fiber number, x is the iteration, y_0 is the offset (or the plateau y value at infinite x), A is the amplitude prefactor for the exponential, and t is the constant decay factor. R^2 values for each group: 0.996 (1.5 mm WD , red), and 0.998 (1 mm WD , blue). Error bars represent the s.d. of the means. (e) SEM micrograph of fibrous mesh, showing overlapping and semi-fused structure of repeated iterations (105 in this case). Segmented overlay shows the information that is input for image analysis. (f) Diameter frequency distribution for the micrograph (e). This distribution is fitted

by a log normal distribution, with R^2 value of 0.988 with centre of $0.41 \mu\text{m}$. (g) Plot of the distribution of fibre diameter as a function of iteration and working distance with point value (μm) indicated in red.

3.4.3. Pattern Variation

3.4.3.1. Effect of Pattern and Maximum Speed on Nanoarray Distribution

To demonstrate patterns of differing types, several pattern designs were developed as shown in Figure 3.7, and this produced corresponding fibrous arrays as shown in Figure 3.7. The electrodes produce a non-homogeneous electric field, which the tip moves through while the jet changes direction based on the changing electric field intensity and direction (see supplementary Figure 3.12). Fabrication of patterns \backslash , \vee and $\backslash Si$ show direct control over fibre array distribution, within the four pillar volume. Figure 3.7 (a) shows a photo of the fibrous array produced using a $\backslash Si$ pattern. The nanoarrays are visible at this scale, due to the overlapping fibre density within the region. Figure 3.7 (b-d) shows top-down microscopy of the \backslash , $\backslash Si$, and \vee patterned nano-arrays.

It should be noted that \vee type patterning deviates from the intended outcome (see Figure 3.7 (d)), presenting a number of fibres spanning the exterior perimeter of the pillars similar to outcomes seen in Si pattern samples. This is despite the electrode motion never passing the perimeter directly. This implies that at some point fibers are drawn between these pillars without the influence of mechanical drawing, solely through electrostatic attraction. This phenomenon may occur as a result of the diagonal pathing entering relatively higher proximity to tertiary pillars (e.g. at the midpoint of pathing) such that fiber jetting changes angle, hitting three separate pillars in transit along diagonal toolpaths, forming the L shape fiber array, instead of the intended two-point diagonal adjacent pillars. The statistical frequency may be managed in future through toolpath management in the form of arc pathing or through electrode design.

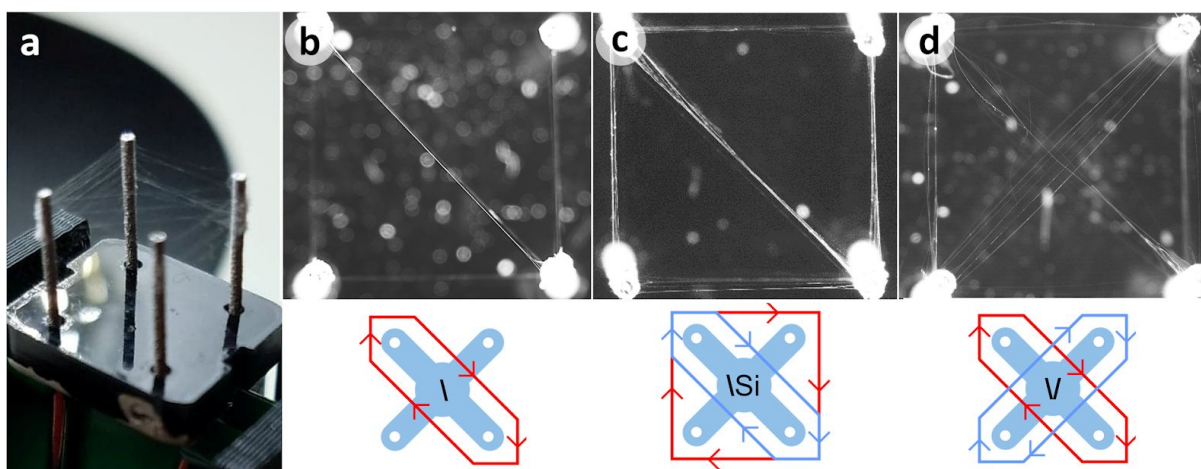


Figure 3.7. Pattern Variation. (a) Photograph of patterned nanofibers meshes suspended on electrode pillars. (b-d) Representative high magnification microscope images of PEO in three different patterns as indicated: toolpaths are indicated in alternate colours blue and red if separated events.

The histogram distribution of NOI for each pattern type is shown in Figure 3.8 (a). From the distributions we find the majority to be over 80% NOI, with the largest outliers in \ pattern. This indicates reasonable variability of OD equivalent to the R patterns applying the same process parameters in section 3.1.1. Figure 3.8 (b) shows the distributions of global maximums between patterns as box plots, bounded in the region of $90 \pm 5^\circ$, indicating a precise outcome for each with high alignment. The \Si pattern (Figure 3.8 (c)) required move sequence consideration, given that the path can interfere with previously deposited fibres. A structure formed of Si followed by \ would remove previously deposited fibres.

3.4.3.2. Effect of Pattern and Maximum Speed on Fibre Density

Figure 3.8 (c) shows the average number of fibres generated by each pattern. Inspection of Shapiro-Wilk normality test revealed that fibre number was normally distributed for all groups and by use of the Levene's test of homogeneity of variance, the variances were found to be significantly different. Univariate ANOVA was performed with the Games-Howell test comparing each group. It was found that, between patterns, the means were significantly different ($p < 0.01$), with mean total fibre number in each group: \Si (39 ± 17.9), V (22.8 ± 6.9), and \ (5.8 ± 4.3). In contrast, changing the speed from 50 to 250 mm/s⁻¹ had a non-significant effect on the fibre number in each case ($p > 0.85$). This result reinforces the

previous finding that the maximum value of 250 mm.s^{-1} does not exceed a critical failure value, or causes significant discontinuities. Additionally, the change in pattern had no bearing on this effect. The differences in fiber number cannot be linked to the differing timeframes in which these patterns operate, between 50 and 250 mm.s^{-1} as there is no significant change within each pattern group. The number is linked proportionally to the number of discrete moves (i.e. mechanical drawing operations) in each pattern. For example the \Si pattern combines the \ pattern and the Si pattern achieving a greater sum number of fibers due to the increased number of moves.

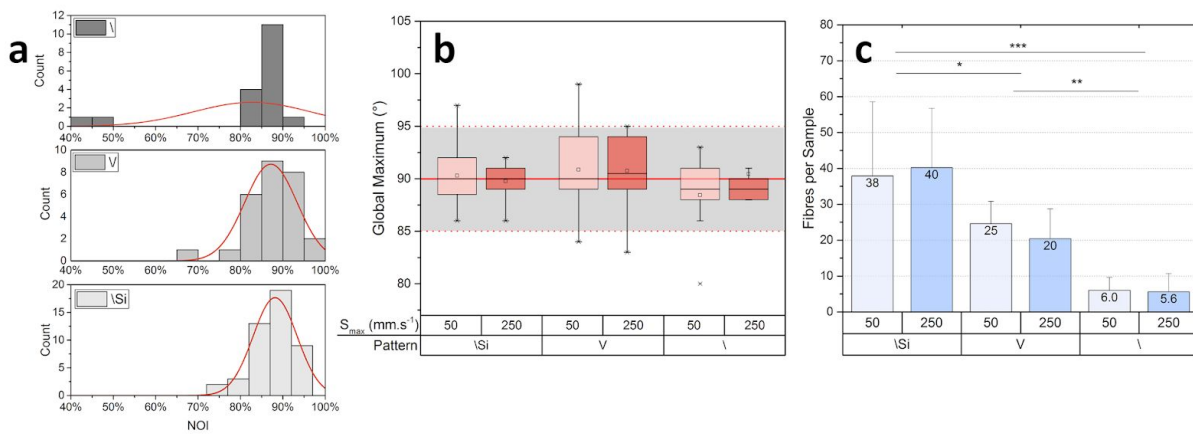


Figure 3.8. Pattern variation statistical information. (a) Normalised Orientation Index (NOI) histograms for each pattern type. (b) Box plots showing the distributions of the maximum peaks as a function of pattern and maximum speed. (c) Number of fibres per pattern type, as well as velocity. Data is presented as the mean \pm s.d. of four independent experiments * $P < 0.01$, ** $P < 0.001$, *** $P < 0.0001$; n.s., not significant. Significance was determined using Welch's t-test (two-sided).

3.5. Conclusions

Nanoarrays of PEO were patterned on 3D four-pillar electrodes, and analysed for their relative isotropy, alignment and diameter distribution. We first examined the process parameters for PEO by testing two process parameter groups: (i) max speed and working distance; (ii) voltage and concentration. In the majority of cases the alignment of the arrays was accurate to $\pm 5^\circ$. The exceptions were found in the extreme values of PEO concentration tested. The results of these experiments show that printed arrays can be significantly affected

by the process parameters. An optimal setting from the findings suggest the most stable parameters for achieving a large number of submicron PEO fibers is 14 wt%, 1.4 kV, using the efficient 60 iterations at a WD of 1mm with the Smax being the least influential parameter when applied in the range of 50-250 mm.s-1 .

In the second study, high density nanofiber meshes of PEO were patterned repeatedly, varying the number of iterations as well as maximum speed. The results showed a clear decaying exponential dependency of fibre number with iteration. The semi-automated NFES system was invaluable in the conduction of this repetitive process, as operations could take as long as two hours for high iteration value 150, for example.

Finally several pattern types were investigated. These patterns exemplified the defining design space for arrays within the constraints of the electrodes used. The degree of control of array structure demonstrates the principle of this technique. The findings of this study are significant as it creates for the first time multiple suspended nanoarrays in a directed manner across multiple working planes *in situ*. This shows promise for future work which can utilize electrodes of greater complexity. Significantly the combination of additive metal SLM and automated instrument systems allowed the investigation of this suspension NFES technique

This study contributes to the growing number of investigations into 3D culture and microtissue construct technologies. Suspended nanofiber arrays have a high surface to volume ratio, potentially improved Young's modulus ²³³, and can mimic the native ECM. Drug and neurotrophic factor release from fiber array scaffolds can achieve sustained, local factor delivery and contact guidance ¹⁸⁴. An example of the practical use of suspended fiber arrays is given in work by Kriebel et al. ¹⁷⁹, producing a nerve guide construct containing PCL arrays. This research builds on our previous work ¹, creating more complex patterns, developed for potential contact guidance and drug delivery applications. This technique is in its earliest development. Further studies, examining the feasibility of SNFES for the above applications, are underway. Ongoing studies aimed at integrating nanoarrays within 3D hydrogel constructs, will rely on improving the precision of the SNFES method.

This work highlights the potential of this new approach as a means of developing 3D scaffold nanostructures large enough for use in microtissue constructs for the medical research sector. Future work will aim to explore the use of biopolymers as well as biodegradable polymers (e.g. polyesters) to address cell culture and tissue engineering applications. This new technique adds a further dimension in nanofabrication tools, allowing the construction of consistent nanofibrous MTCs in a manner that facilitates cell culture, and tissue engineering studies, presenting an opportunity to examine the effects of nanofiber arrays distribution in 3D cell culture.

3.5.1. Acknowledgements

The authors acknowledge the financial support of the Australian Research Council (ARC) Centre of Excellence Scheme (Project CE 140100012). The authors thank the Australian National Fabrication Facility (ANFF) for providing facilities for the fabrication of the NFES system components. The authors thank the University of Wollongong Electron Microscopy Centre (EMC) for providing SEM facilities. The authors thank Mr. Grant Barnsley for his support in the fabrication of collector electrode arrays, and Mr Benjamin Filipi for his work in the production of the automatic cleaning device.

3.6. Supplementary Section

3.6.1. Centroid Function

The function built in the script editing module of Origin analysis software, was designed to produce the centroid of a distribution and is shown in Figure 3.9. See original source at this [link](#).

```
void centroid(string strCurve)
{
    Curve crv( strCurve );
    Dataset dsX;
    crv.AttachX(dsX);
    if( !crv || !dsX )
    {
        printf("%s is not a valid curve!\n", strCurve);
        return;
    }

    int iBegin = crv.GetLowerBound();
    int iEnd = crv.GetUpperBound();
    double dCentroid = 0, dSum = 0;

    for( int j = iBegin; j <= iEnd; j++)
    {
        dCentroid += dsX[j] * crv[j];
        dSum += crv[j];
    }
    dCentroid /= dSum;

    printf("Curve name: \t %s\n", strCurve);
    printf("X range: \t %f to %f\n", dsX[iBegin], dsX[iEnd]);
    printf("Centroid = \t %f\n\n", dCentroid);
}
```

Figure 3.9. Centroid function. Highlighted text indicates the main mathematical function.

3.6.2. Fiber Count Functions

The Fibre Count function (see Figure 3.10) operates using the ImageJ macro language, calling specific functions in sequence. Put simply, the function takes an open image and crops to a quartile region and measures the pixels. This is designed to crop a specific image generated in the DiameterJ plugin. The upper right quartile contains the fibre array which has been reduced to a skeletonised image, where the fibres are one pixel in width. The function runs four sequential profile measurements of the image horizontally, outputting the pixel values from 0 (black) to 255 (white) across the profile. These four columnated arrays are condensed using a matlab program which places the columns in a single .csv file. This is then copied into an interpretation program written in Google Sheets which counts the number of black pixels (zeros) in the columnated profiles. The mean of the black pixel count is considered the effective fiber number of the sample. This has the advantage of discounting fibres which do not span the total area between the pillars.


```

1 //Crop to region of interest
2 ws=getWidth();
3 hs=getHeight();
4 makeRectangle(0, 0, ws, hs);
5
6 name=getTitle;
7 run("Crop");
8 run("Select All");
9 run("Invert");
10 run("Copy");
11
12 //Check dimensions and create copy named Segment
13 w=getWidth();
14 h=getHeight();
15 close();
16 newImage("Segment", "8-bit", w, h, 1);
17 run("Paste");
18 selectImage("Segment");
19 run("Set Scale...", "distance=363 known=1 pixel=1 unit=mm");
20 run("Colors...", "foreground=black background=white selection=yellow");
21 run("Options...", "iterations=1 black count=1");
22 run("8-bit");
23
24 //Generate lines and profile each line
25
26 //1
27 makeLine(0, (h/5)*1, w, (h/5)*1);
28 run("Clear Results");
29 profile = getProfile();
30 for (i=0; i<profile.length; i++)
31 | setResult("Value", i, profile[i]);
32 updateResults;
33 path = "C:/Users/arn734/Pictures/MICROSCOPE/Image Analysis/count" + name + "1.csv";
34 saveAs("Results", path);
35
36 //2
37 makeLine(0, (h/5)*2, w, (h/5)*2);
38 run("Clear Results");
39 profile = getProfile();
40 for (i=0; i<profile.length; i++)
41 | setResult("Value", i, profile[i]);
42 updateResults;
43 path = "C:/Users/arn734/Pictures/MICROSCOPE/Image Analysis/count" + name + "2.csv";
44 saveAs("Results", path);
45
46 //3
47 makeLine(0, (h/5)*3, w, (h/5)*3);
48 run("Clear Results");
49 profile = getProfile();
50 for (i=0; i<profile.length; i++)
51 | setResult("Value", i, profile[i]);
52 updateResults;
53 path = "C:/Users/arn734/Pictures/MICROSCOPE/Image Analysis/count" + name + "3.csv";
54 saveAs("Results", path);
55
56 //4
57 makeLine(0, (h/5)*4, w, (h/5)*4);
58 run("Clear Results");
59 profile = getProfile();
60 for (i=0; i<profile.length; i++)
61 | setResult("Value", i, profile[i]);
62 updateResults;
63
64 path = "C:/Users/arn734/Pictures/MICROSCOPE/Image Analysis/count" + name + "4.csv";
65 saveAs("Results", path);
66 close();

```

Figure 3.10. Fibre counting macro function.

3.6.3. Image Analysis Process

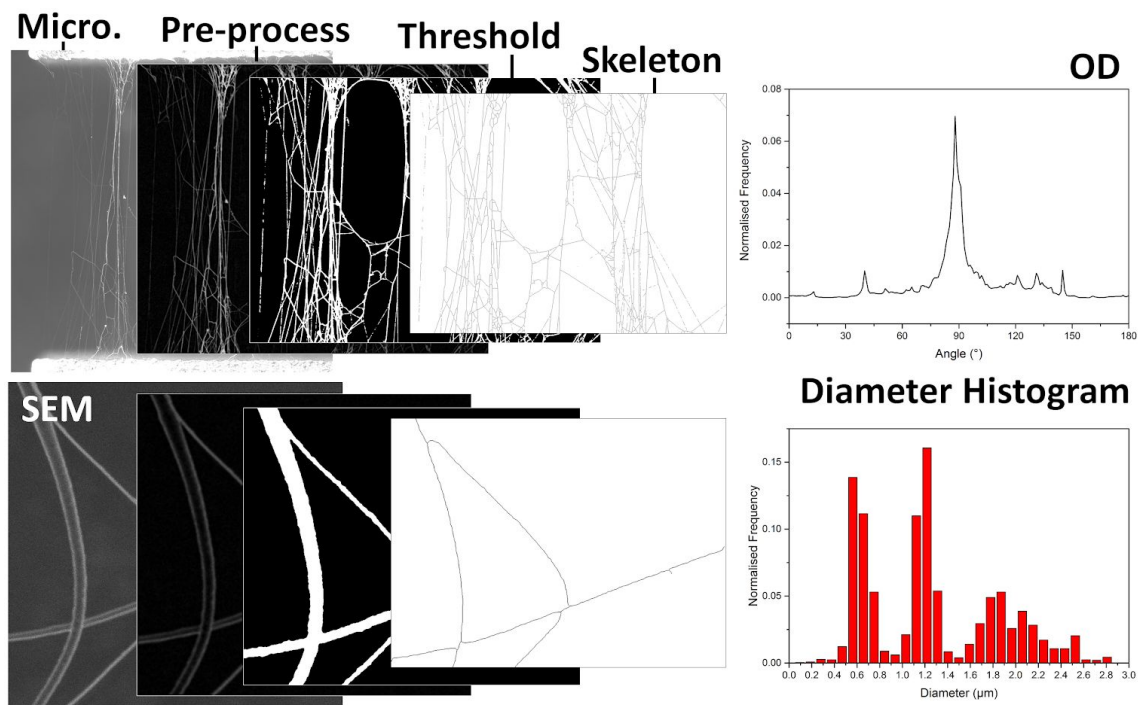


Figure 3.11. Image analysis processing steps for microscopy and SEM.

3.6.4. Electric Field Simulation

The electric field was simulated for the electrodes using a typical voltage of 1.6 kV, in the modelling software Comsol Multiphysics working using a model generated using the Solidworks CAD program (see Figure 3.12 (a)). This illustrates an example of the change in electric field intensity during operation. Please see attached animation (Supplementary Video 2 and Video 3) which illustrates the *R* and *Si* patterns.

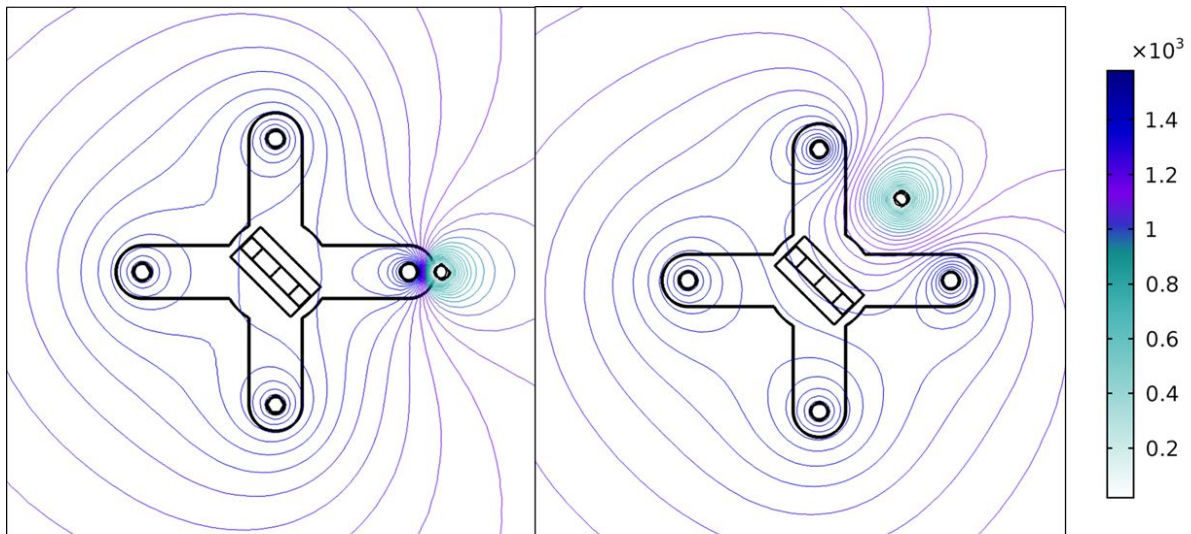


Figure 3.12. Simulation of electric field lines as the emitter moves relative to the electrode pillars at a voltage of 1.6kV.

3.6.5. PEO Rheological Characterisation

Polymer solution viscosity is primarily caused by the friction of entangled polymer chains. The variation of viscosity with polymer concentration depends on the nature of the polymer and solvent. PEO solutions were analysed by cone plate shear flow rheology. PEO concentration shows an exponential dependency on polymer concentration as shown in Figure 3.13 (a). The solutions viscosity is shear rate dependant as shown in Figure 3.13 (b), showing a response typical of non-newtonian shear thinning fluid, although this character is only visible for high concentration solutions, with the lower concentrations retaining the newtonian characteristics of the solvents, water and ethanol. The exponential dependency of viscosity and the shear thinning characteristics can give insights into flow behaviour and fiber output in electrospinning.

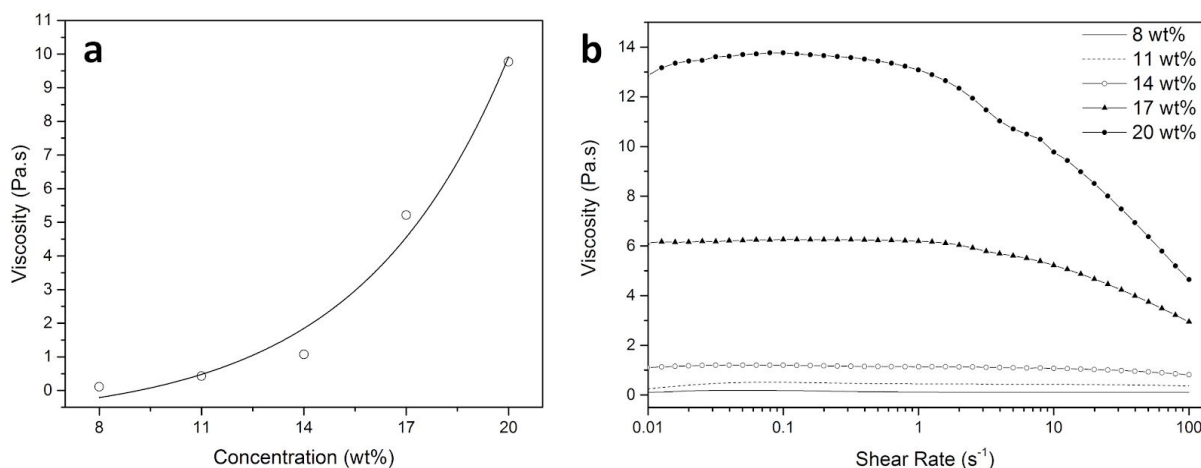


Figure 3.13. PEO rheology. (a) Viscosity of PEO solutions in water/ethanol (3:2) as a function of concentration. Held at shear rate of $10\ s^{-1}$. (b) Viscosity of PEO solutions in water/ethanol (3:2) as a function of shear rate.

3.6.6. Effects of Parameter Variation

Figure 3.14 (a) shows the distribution of fibre diameter as a function of WD and S_{\max} . Minimal differences suggest that these parameters do not affect fiber diameter with any consistent linearity. With increasing electrode proximity the electric field is linearly increased. With each unique setting, the maximum electric field varies. Figure 3.14 (b) shows the distribution of fibre number as a function of WD and S_{\max} . Ideal fibre number is 50 for a pattern generating 50 passes of the electrode pillars. The range of estimated fibre number in each group is substantially lower than ideal: 22% to 5.6% of the objective. Figure 3.14 (c) shows the distribution of fibre number as a function of voltage and concentration. The mean fibre number is below the objective by a similar degree in both treatment groups, with the highest success rate seen in samples generated using 50 mm.s^{-1} S_{\max} , 1 mm Wd, 1.6 kV, and 14% wt PEO solution. For this reason these parameter settings were carried through in subsequent experimental groups.

The estimated mean fibre number found indicates a poor outcome in terms of reaching the objective. Such an outcome may be due to a number of possible events. Excessive or insufficient force: speed, acceleration, surface tension, electric field variation, causing discontinuity of ejection. Preference for individual fibril deposition on the pillar, due to insufficient drawing speed among other parameters. Fibre breakdown after suspension due to poor material properties, subsequent fiber interference.

To quantify the branching morphology of the suspended array structures, intersection number was assessed in each parameter set (see supplementary figure 3.15). The ratio of the intersection number divided by the number of fibers gives an indication of the density of intersections, normalising across differing fiber number samples.

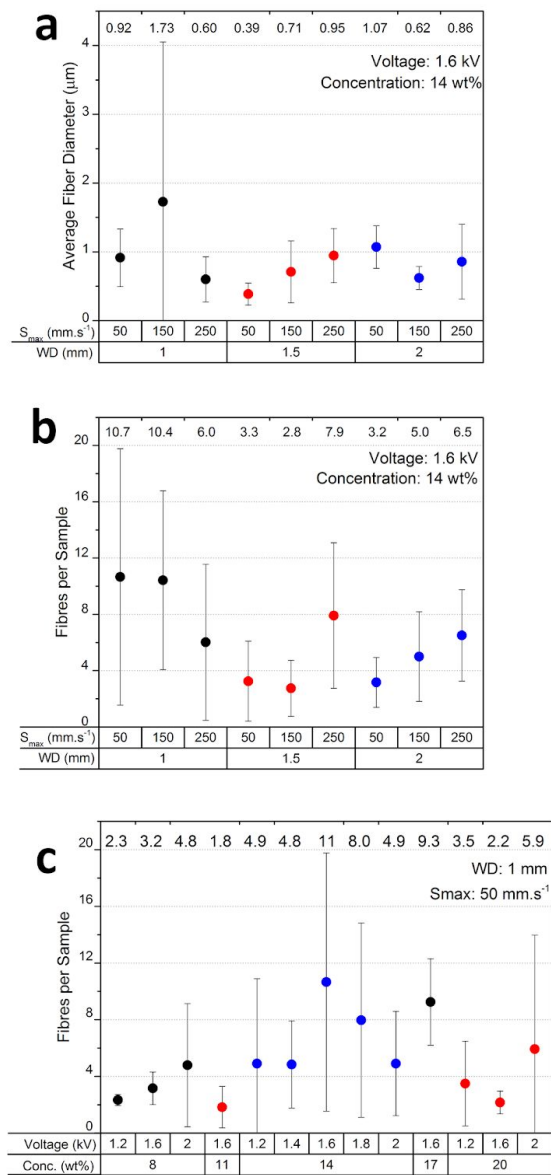


Figure 3.14. Fiber variation as a function of process parameter variance. (a) Average fiber diameter variation as a function of WD and S_{max} . (b) Fiber number as a function of S_{max} , and working distance. (c) Fiber number as a function of voltage and concentration

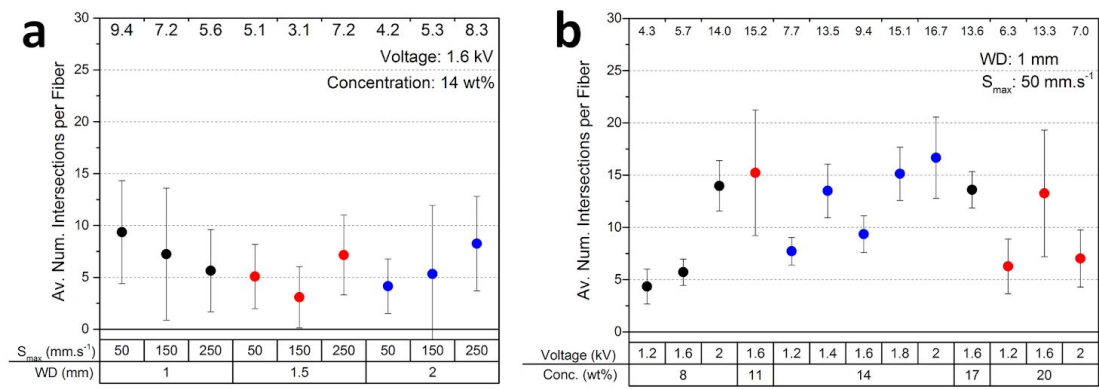


Figure 3.15. Intersection per Fiber number variation as a function of process parameter setting in raster pattern SNFES: (a) As a function of WD and Smax. (b) As a function of Voltage and Concentration.

3.6.7. Fiber Examples

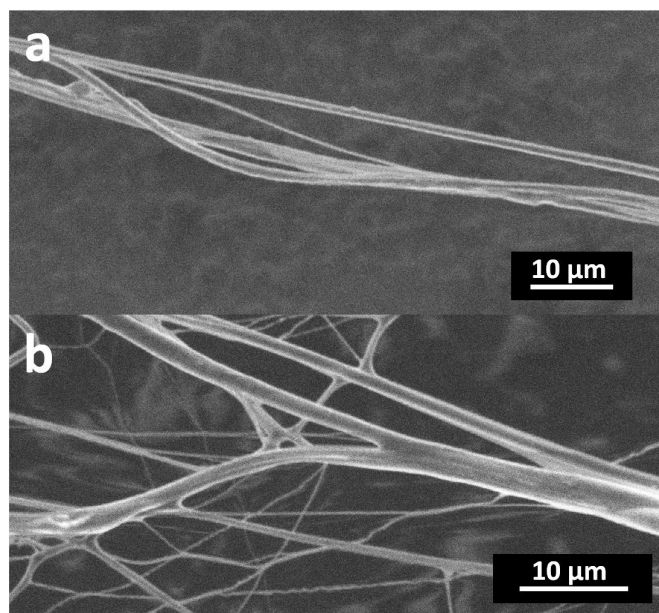


Figure 3.16. SEM micrographs of PEO arrays exhibiting (a) fibre bundling and (b) fibre fusing.

3.6.8. Video Files

Supplementary Video 3.1. Pattern Operation Example. The video shows automatic cleaning, followed by manual initiation and \ patterning.

Supplementary Video 3.2. *R* Pattern Electric Field Simulation.

Supplementary Video 3.3. *Si* Pattern Electric Field Simulation.

Chapter 4. Suspended Three-dimensional Polycaprolactone Nanofibers Encapsulated within a Gelangum Methacrylate Hydrogel for Neural Tissue Engineering

This chapter has been adapted, with the author's permission, from the article - 'Suspended Three-dimensional Polycaprolactone Nanofibers Encapsulated within a Gelangum Methacrylate Hydrogel for Neural Tissue Engineering', submitted for peer review to the journal Materials Science and Engineering: C.

Alexander R. Nagle, Thomas M. Robinson, Cormac D. Fay, Gordon G. Wallace, Zhilian Yue, and Michael J. Higgins

ARC Centre of Excellence for Electromaterials Science, Intelligent Polymer Research Institute, AIIM Facility, University of Wollongong, NSW 2522, Australia

Author Statement:

The study detailed in this chapter could not have been made without the work of i) Dr. Cormac D. Fay, who produced the NFES platform control software, editorial as well as intellectual support.. ii) Mr. Thomas Robinson, who provided all hydrogel materials by synthesis and raw material characterisation. iii) Mr. Grant Barnsley who acted as fabrication technician of selective laser melt manufacture of collector electrode arrays. All experiments and data analysis presented in this chapter were completed by the author, Alexander R. Nagle.

Preface

This chapter is divided into three parts. The first part aims to introduce the theory of NFES and cover the background of suspension based ES. The second describes the method applied to generate suspended polymer nanoarrays on four-pillar electrodes, varying the parameters of NFES. The third part discusses the results of this study.

Abstract

A major goal in tissue engineering is to mimic the nanofibrous proteins found in the extracellular matrix. Near-Field Electrospinning (NFES) is a versatile nanofiber patterning technique, which can utilise the layer-by-layer method to create microstructures to mimic these native nanofibrous proteins. However, this layer-by-layer method generates disconnected pores within the microstructure, and high volume can be difficult to achieve due to inhibition of the ejection process by increased electrostatic charge of many layers.

Here, we use suspension NFES (SNFES) to pattern ultrafine polycaprolactone fibers onto 3D electrode collectors, manufactured by Selective Laser Melting, with smallest fiber diameter of $0.76 \pm 0.26 \mu\text{m}$. The fiber array structures were encapsulated within a biocompatible gellan gum methacrylate hydrogel matrix. It was found that fiber encapsulation increased the construct's mechanical properties, raising the storage modulus from 0.17 kPa (control) up to 1.28 kPa. Further investigations elucidated the conditions of array influence in this regard, examining the effects of changing fiber diameter through parameter variation as well as changing electrode pillar design and pattern implementation. The constructs produced were investigated through these parametric studies to achieve a hybrid tissue construct, with potential for 3D neural tissue engineering application.

4.1. Introduction

In the brain, disease (carcinoma, stroke) and traumatic injury cause permanent damage, leading to debilitating cognitive and motor dysfunction for many people throughout the world

²³⁴. Current treatments are incapable of achieving optimal recovery, as they do not address the loss of tissue at the site of trauma, with the brain only capable of limited self-repair. In excision cavities regenerative cell therapy can be enhanced by a supportive matrix that imitates the natural microenvironment to achieve directed cell maturation and integration at the implant site ^{11,18}. The matrix must present structural guidance for neurite outgrowth; regulate fluid flow to supply nutrients and remove metabolic waste; regulate cell behaviours such as migration and differentiation through chemical and physical cues; and deter cell death and fibrosis ¹⁸. To achieve these goals, tissue engineering (TE) applies scaffolding; bioactive molecule encapsulation; fluidic control realised via bioreactor or built-in channels; and electrostimulation. The native neural stem cells extracellular matrix (nECM), exhibits complex pinwheel architectures ²⁹, formed of interconnected, porous 3D nanofibrous proteins and proteoglycans ²³⁵, which impart physical and biochemical cues necessary for cell survival and development ^{3,46}.

For such structures to operate, an interconnected porosity is necessary to allow diffusion of oxygen and nutrients to embedded cells and allow for waste removal ⁸¹. Cell migration and angiogenesis rely on this interconnectivity, while the cell type determines the pore size required ^{236–238}. Variation in the dimension and hierarchy of the environment, alters cell behaviour. A 3D aspect to an environment permits cellular migration and improves viability ^{26,28,213,239}. At present, the most prevalent 3D culture technologies today include aggregate cultures ^{240,241} and scaffolding; solid synthetic material based ^{239,242–244} and/or hydrogel based ^{245–247}.

Hydrogels are crosslinked hydrophilic polymers that swell substantially in water, typically forming a randomly interconnected network, with tunable porosity ²⁴⁸ which varies based on parameters such as crosslinking density ⁴⁵, water content ^{248,249}, and temperature ²⁵⁰. For biomedical applications, hydrogels are designed to resemble the characteristics of native tissue and to provide 3D supports for cellular growth and tissue formation. A hydrogel's ability to gel in situ allows for minimally invasive and effective surgical implantation, as the liquid precursor can be injected, conformally filling irregular cavities created in excision voids, before crosslinking forms the supportive matrix ^{6,251–256}. However, hydrogels are typically soft or mechanically weak, requiring low force environments ^{36,257–259}.

Nanofabrication methods in TE aim to mimic the nanofibrous structural characteristics of the nECM. One of the most commonly investigated nanofiber fabrication methods is electrospinning due to its relative simplicity, low cost, and variety of material choice. Early investigations in electrospinning for tissue engineering investigated cell interactions on planar fibrous mats^{30,38,260,261}. More recent research has focused on the substrate structure or alignment in which fiber orientation leads to a corresponding cell orientation and migration via contact guidance^{47–50}. Sub-micron fibers have a beneficial effect on cell viability^{30,37,38} and behaviour⁴⁶, however, the random deposition of electrospinning produces bulk pore sizes too narrow to allow for cell infiltration^{48,262–264}, with exceptions using large microfibers to achieve a greater pore size²⁶⁵, lacking the benefits of nanoscale fibers.

Current advances in nanofabrication methods have allowed for the creation of pore size controlled microstructures. Controllable patterning of ultrafine fibers has developed, in both solution and melt based electro-writing, from the near-field electrospinning (NFES) technique, which applies a reduced working distance and lower voltage. In this NFES scheme, recent developments have progressed the technique beyond 2D patterning to producing 3D ordered structures by additive layer-by-layer deposition^{40,146,167,171,172,194}. This has extended NFES capabilities, allowing researchers to develop 3D microfiber scaffolds for TE research via layer-by layer electro-writing^{40,167}.

A typical 3D culture volume is on the order of 0.1cm^3 ²⁶. The layer-by-layer technique is limited by the suppression of an electric field, arising from the accumulation of charged polymer fiber, inhibiting deposition⁴⁰. Due to this restriction, Visser *et al.* applied sheet assembly⁴⁰, forming greater structures for hydrogel encapsulation. However, this delamination and manual assembly may lead to the destruction of fragile 3D nanofiber architectures. Researchers have electro-written layered lattice structures to control pore size^{164,165}. However, the lattice pores can be limited in their inter-connectivity by the lattice walls^{40,167}, and can also be biomimetically limited by the use of melt based electro-writing, producing fibers with diameters over a micron.

When implemented individually, hydrogels and nanofibrous scaffolds are inadequate for 3D cell culture. To build up a 3D array of nanofibers within a hydrogel we propose the use of a suspension NFES (SNFES) technique, utilising 3D collectors manufactured by Selective Laser Melting (SLM). Patterned fibrous polycaprolactone (PCL) arrays generated on the electrodes, were then encapsulated within a bio-compatible gellan gum methacrylate (GGMA) ²⁶⁶ hydrogel matrix. To mimic the complex nECM tissue, several key aspects are important to address: fiber orientation, sub-micron diameter, construct bulk volume and interconnected porosity ^{208,267}. The constructs produced were investigated through parametric studies to achieve a mechanically tunable matrix with potential application as a tissue construct for 3D cell culture.

4.2. Materials and Methods

4.2.1. Materials

Titanium Grade 5 (Ti 6Al-4V) powder (spherical particle size < 63 μm) was purchased from TLS Technik GmbH (Bitterfeld, Germany). Lithium phenyl-2,4,6-trimethylbenzoylphosphinate (LAP) ($\geq 95\%$)²⁶⁸, Low-acyl gellan gum (GG) (Gelzan®, Gelrite®, Mw = 1,000 kg/mol), and methacrylic anhydride (MA) were sourced from Sigma-Aldrich Co. (Sydney, Australia). GG was purified by dialysis to remove excess impurities and cations from solution. Polycaprolactone (PCL) pellets (average M_n : 80,000), purchased from Sigma-Aldrich Co. (Sydney, Australia), were mixed by shaking for 1 hr with fluorescein sodium salt (Sigma-Aldrich Co., Sydney, Australia) (30 mg) in a binary solution of glacial acetic acid (AA) and formic acid (FA) (3:1 by volume) to generate solutions of varying concentration (5, 10, 12.5, 15, 17.5, 20, 22.5, 25 wt%) above and below ranges used in previous literature^{88,269}. Fiber samples were generated within 24 hours of solution preparation to avoid extensive bond denaturation of PCL by acid-catalyzed hydrolysis of the ester bonds.

4.2.2. NFES System

An in-house developed system was used for all suspension NFES¹. Briefly, This system consisted of a two-axis X-Y platform, translating collecting electrodes beneath a syringe pump on a vertical Z-stage, mounting the syringe and emitter tip. The emitter needle tip used was a 25 gauge, 0.25 mm inner diameter stainless steel and was connected to ground to allow for electric field formation. The instrumentation was controlled by in-house developed software.

An SLM-50 (Realiser) was used to produce four-pillar electrodes from grade 5 titanium powder¹. Eight-pillar electrodes were made using a more advanced Direct Metal Laser Melting (DMLM) [Mlab](#) cusing 200R (General Electric), using Grade 23 titanium powder. These methods produced analogous electrodes, with a slightly improved micro-particle surface finish in the latter case. These electrodes, shown in Figure 4.1 (A-B), were connected by their underside pins to IDC sockets, locking them to the X-Y platform. The sockets were connected to positive bias high voltage power supply (ES30, Gamma HV) via a mounted

contact point on the X-Y platform. The system was contained in a perspex case, which was flooded with dehumidified air (ca. 19% RH), measured using a temperature and humidity data logger (XC0424).

4.2.3. Synthesis of Gellan Gum Methacrylate

Gellan gum methacrylate (GGMA) powder was synthesized through the reaction of gellan gum (GG) and methacrylic anhydride (MA) in a similar manner to the methods employed by Coutinho et al., applying the reaction scheme shown in their work ²⁷⁰.

Briefly, 1% (w/v) of GG was dissolved in deionized water at 90 °C for 30 min, and then allowed to cool to 50 °C. Subsequently, 8% (v/v) of MA was added dropwise to this solution and the reaction mixture was under continuous stirring for 6 more hours, during which the pH of the reaction was maintained at ~8.0 using 5M NaOH. The solution was centrifuged at 4400 rpm for 5 min at 21 °C to remove excess MA. The clear solution was poured directly into an excess of chilled acetone, three times the sample volume, and allowed to precipitate overnight at -20 °C. The GGMA precipitate was collected by centrifugation at 7,500 rpm for 5 min at room temperature, and dissolved in deionised water at 37 °C under constant stirring for 30 min to ensure complete dissolution. The GGMA precipitate was resuspended in 50 mL of deionized water and heated to 37 °C under constant stirring for 30 min to ensure complete dissolution. The GGMA solution was then purified by dialysis (membrane with molecular weight cut-off of 12-14 kDa, Sigma-Aldrich)) for 3 days against distilled water to ensure complete removal of any residual MA and acetone. Water was exchanged at least three times per day until a clear solution was evident. In the event of any remaining large particles left in suspension, the purified GGMA was vacuum filtered. The GGMA was lyophilized and stored in a dry place under dark conditions to protect it from UV exposure until further use. All batches achieved approximately $19.1 \pm 0.2\%$ DS measured by ¹H NMR spectroscopy, where all -OH sites were accounted for with regards to methacrylation, providing ~2.10 methacrylate groups within each repeating tetramer.

4.2.4. Suspended Nanofiber Fabrication

Suspended nanoarrays were generated using two distinct inter-pin patterns. A square iterative (Si) pattern was used to generate polymer nanoarrays on four-pillar electrodes (see Figure 4.1

(A)). The needle tip moves in each pattern, navigating electrode pillars such that the tip's surface never moves within a working distance (WD) proximity of any pillar's surface. The tip is raised in a series of 0.1 mm steps in the Z axis, after each full pattern is completed, forming a stacked series of patterns with a total height of 2 mm (finishing level) with the apex of the electrode. The 1 mm steps were chosen to achieve this height in a reasonable timeframe. For the four-pillar electrodes a square-iterative (Si) pattern was implemented (see Figure 4.1 (C) and (F)). For eight-pillar electrodes a more complex, cross square iterative (CSi) pattern was implemented (see Figure 4.1 (D)). This was done to achieve a much higher volume network of suspended fiber arrays, compared to a Si pattern, which operates only to deposit external perimeter. This CSi pattern works within the constraints of the eight-pillar electrode geometry, passing by pillars at midpoint distances. Iteration in this method is defined as the number of complete cycles the pattern is performed at a certain height, before a Z -axis 0.1 mm step.

The electrodes were washed in an aqueous ethanol (70% v/v) solution, before being mounted on the electrode platform, within a recess in the acrylic (shown in Figure 4.1 (F.1)), and connected to the IDC line sockets (shown in Figure 4.1 (E.1)). The environment's humidity was lowered by first flooding the case with dehumidified compressed air, then supplying compressed air at low pressure once the humidity reached 19% RH, the consistent humidity of the compressed air line. This was held constant during all SNFES fabrication experiments. The polymer solution was loaded in a sterile 1 mL syringe and mounted on the syringe pump. A monochrome camera (Chameleon, PTGrey) was used to calibrate the blunt tip with the electrode pin apex, as well as to observe the SNFES process (shown in Figure 4.1 (G)). The G-code pattern was then generated from this calibration using a spreadsheet program, set with coordinates of the particular pattern to be implemented.

For each experiment, the following procedure was implemented. A solution droplet was first formed and maintained, a voltage was applied between the tip and the electrodes, and the G-code pattern was initiated. An initial cleaning procedure was carried out using the automatic cleaning system. The initiation of electrospinning was achieved by breaking the emitter droplet surface on a sharp stainless steel pin embedded in the platform, then commencing the pattern. Patterns are halted in their process by a periodic cleaning procedure,

and subsequent reinitiation, every 15 patterns completed. This was done to prevent buildup of detritus and drying at the outlet, which would lead to a discontinuation of the ejection process.

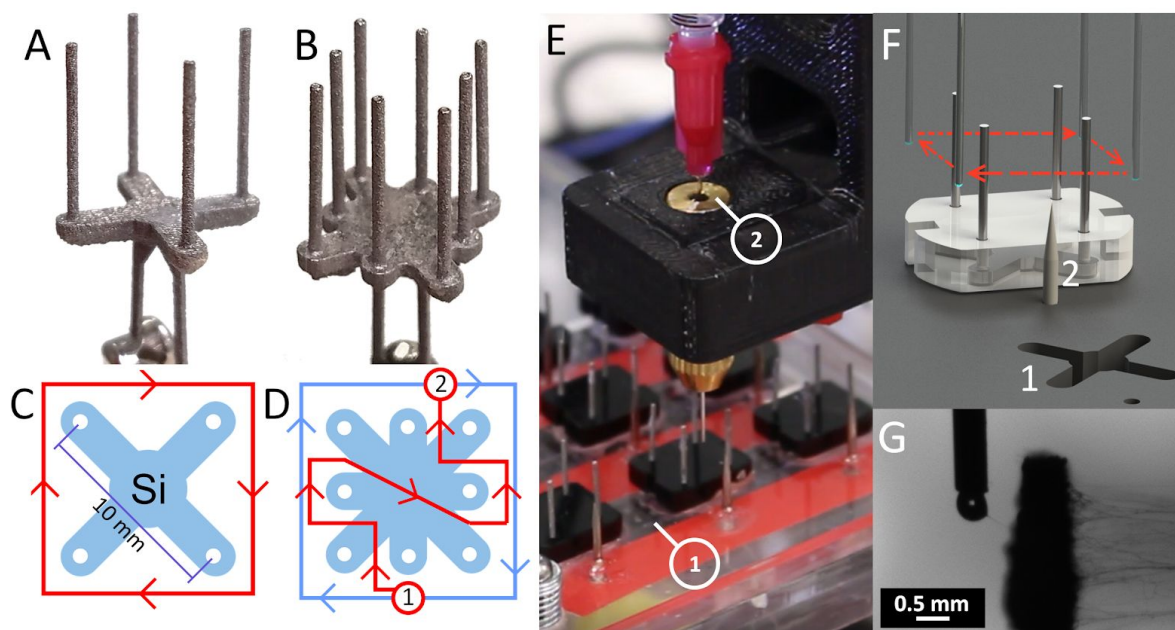


Figure 4.1. Electrodes and toolpath routes for patterns. (A) Four-pillar electrode. (B) Eight-pillar electrode. (C) *Si* pattern. (D) *CSi* pattern with indicated starting position (1), moving to position (2) along the inner red path, completing the outer blue path (2-2), return from (2-1) along the red path and repeat from (1). (E) Photo of the emitter and electrode array setup, during operation. (1) IDC line sockets; (2) (F) Model of the *Si* pattern showing the four-pillar electrode with cap mounted in the acrylic recess. (G) Magnified photo of the SNFES process, showing the emitter producing fibers on a pillar electrode.

4.2.5. Encapsulation of Nanofiber Arrays

GGMA fibrous material, partially dried, was first vacuum dried in an oven depressurised to -60 kPa at 70 °C for two hours to remove any residual water content for subsequent solution preparation. A stock solution of GGMA at 1 wt% was prepared at 37 °C and stored at -18 °C until needed. This was then heated in a water bath at 37 °C for 1 hr. The tube was then shaken by vortex mixer until the solute was dissolved. The solution was frozen until needed. Prior to gelation, 1 mL GGMA solution was thawed and LAP (photoinitiator) was added with a final

concentration of 0.06 wt% . The sample was centrifuged at 1,000 rpm for 30s to remove any air bubbles trapped in the solution and protected from light to avoid premature crosslinking.

Acrylic moulds were laser cut, one 5 mm the other 10 mm thick acrylic, with a centred hole in each, diameters 11.9, and 15.6 mm respectively. The lower 5 mm thick section was laser etched to allow for press-fit attachments of the acrylic mould to the end of a glass slide (see Figure 4.3 (A)). Petroleum jelly was applied to the mould surfaces to ensure a tight seal and offer a hydrophobic coating for ease of sample removal. 0.33 mL GGMA-LAP solution was pipetted into each mould from the sides, filling to approximately 3 mm height in the lower well. Pillar electrodes hosting the fibres were inserted into the mould, pin apex down, resting on the glass slide. Control samples were created using bare moulds, without electrode insertion.

A UV lamp (Omnicure® LX400+, Excelitas Technologies Corp.) operating at 400 nm wavelength, max power 9000 mW.cm^{-2} , was shone at 15% intensity (I) ca. 54 mW.cm^{-2} , from below the slide at a working distance (D) of 5 cm, on to the solution surface (see Figure 4.3). The wells were then covered to prevent further UV exposure. The slides were left in darkness to allow crosslinking to complete and the system to reach equilibrium. After the gelation was allowed to complete ca. 30 minutes the cover was removed and each electrode was gently removed from the wells, with the hydrogel on the surface of the glass slide (see Figure 4.3 (A4)). LAP was chosen as the photoinitiator due to its concentration dependant biocompatibility^{268,271}, water solubility, as well as its simple and effective crosslinking process. For SNFES fabrication the tip inner diameter was held constant at 0.25 mm in all experiments.

To examine the effect of fiber diameter on construct properties, PCL solution concentration was varied across a range of concentrations. These solutions were applied in SNFES using a four-pillar electrode with a *Si* pattern. The following process variables, determined by observation of jetting consistency, were kept constant: extrusion rate (4 nl.s^{-1}), applied voltage (1.9 kV), WD (1.5 mm), iteration (15), and S_{max} (250 mm.s^{-1}). These arrays were then encapsulated within the GGMA hydrogel using a curing time of 120 seconds via the

encapsulation technique as described (n=4). This time was chosen as it produced hydrogel of sufficient mechanical cohesion for manual handling, compared to 60 s curing.

To examine the effect of increased electrode pillar density, with the goal of increasing fiber volume and density, the eight-pillar electrodes were employed in SNFES. The CSi pattern, using 10 wt% concentration PCL was used. The CSi pattern operated in between pillars of the electrode and required careful maneuvering and so the path operated to move through the midpoint of the gap between each pair of pillars. The *WD* to achieve this cannot be varied, by this definition, and was held constant at 1.19 mm based on the nominal radius of the electrodes ca. 0.32 mm (see Figure 4.1 (D)). The following process variables were kept constant: extrusion rate (4 nl.s⁻¹), applied voltage (1.9 kV), iteration (15), and S_{max} (250 mm.s⁻¹). The samples were encapsulated using a curing time of 120 seconds (n=4).

To examine the effect of fiber density an iteration value of 60 was implemented in tests using four pillar and eight-pillar electrodes, patterning with *Si* and *CSi* pattern respectively. To output a higher volume of fibers the *Si* pattern on four-pillar electrodes was modified to work at a greater distance using a higher voltage (3.6 kV), placing a higher electrostatic force on the emitting jet. If an equivalent voltage was used at lower working distances (1-2 mm), arcing was observed to occur under conditions of 19% RH. The following process variables were kept constant for four-pillar electrodes: extrusion rate (4 nl.s⁻¹), applied voltage (3.6 kV), *WD* (3 mm), and S_{max} (250 mm.s⁻¹). The following process variables were kept constant for eight-pillar electrodes: extrusion rate (4 nl.s⁻¹), PCL solution concentration (10 wt%), applied voltage (1.9 kV), *WD* (1.19 mm), and S_{max} (250 mm.s⁻¹). The samples were encapsulated using a curing time of 120 seconds (n=4).

4.2.6. Rheological and Dynamic Mechanical Analysis

The viscosity of the polymer solutions, for various concentrations, was measured using a rheometer (ARG2, TA Instruments, Delaware, USA), fitted with a temperature controlled steel base-plate. Flow curves were recorded to evaluate the viscosity of liquid samples at shear rates between 0.01 and 100 Hz, with the aid of a conical plate measuring tool (steel, 60

mm diameter, 2° angle). All experiments were performed at a controlled temperature of 22°C.

To assess the effect of fiber diameter, number and distribution on the mechanical properties of the developed hydrogels; isothermal dynamic mechanical analysis (DMA), using a frequency sweep mode, was performed on a DMA Q800 (TA Instruments). All hydrogels and hybrid constructs were prepared as cylinders, nominally 11.9 mm in diameter and approximately 3 mm in height. Gels were swollen in phosphate buffer saline (PBS) solution at 37 °C for over 24 hours to allow a swelling equilibrium to be reached. Hydrogel mechanical properties were measured isothermally at 37 °C, via oscillation frequency sweep of 1-50 Hz with a constant strain of 0.5% compression, using a 50 mm diameter flat steel plate. A 0.001 N compressive contact force was applied to the specimen to ensure repeatable data collection and preserve contact with the sample. Upon completion of data acquisition, the DMA software calculated the compressive moduli as a function of frequency.

4.2.7. Optical Characterisation

4.2.7.1. Light Microscopy

3D fiber arrays were imaged by light microscopy (M205A, Leica Microsystems) from a plane orthogonal perspective relative to each array, and hybrid constructs were imaged for illustration purposes. To achieve reproducible imaging, the electrodes were held by their connection pins using bulldog clips mounted on 3D printed bases.

4.2.7.2. Scanning Electron Microscopy (SEM)

To study the topology of the fibers, SEM images were acquired operating at 10 kV. Electrodes suspending fiber arrays were mounted on aluminium stubs, by carbon tape and analysed as a whole using SEM (Jeol, JSM-7500FA).

4.2.7.3. Laser Confocal Fluorescence Microscopy

To examine the fiber arrays within the GGMA-Array construct, a laser confocal fluorescence microscope (TCS SP5 Confocal, Leica Microsystems) was used to image volumes at the surface of a several samples using a 488 nm wavelength laser with a 504 nm - 578 nm filter.

4.2.7.4. Image Analysis

SEM as well as microscopy images were semi-automatically analysed using ImageJ software (National Institutes of Health, USA) by a number of distinct methods and plugin programs.

Microscopy images of fiber arrays were first pre-processed through successive rounds of background removal, despeckle and contrast enhancement commands (local and global). Processed images were then manually thresholded creating segmented images, which were then analysed using the ImageJ plugin DiameterJ²²⁵. The fiber number was calculated from the skeletonised DiameterJ output images, measuring the number of fiber pixels crossing four horizontal profile measurements. Cases in which the fiber array mesh density was above a reasonable limit, where fiber overlap leads to miscounting, were not analysed (e.g. samples generated in the iteration study were entirely exempted), as a reasonable fiber separation is required for a determination of fiber number in light microscopy.

SEM images of the fibers were first processed in a similar manner as with the microscopy images, generating segmented images. These were analysed by DiameterJ to measure the diameter distribution and mean value in each image, which allowed the mean diameter in each case to be calculated from a set of images (n=5). Confocal images were analysed by a Simple Neurite Tracer, a plugin program of ImageJ and part of the project Fiji, a suite of programs for image analysis of biological systems. This allowed the thresholding, in 3D, of the stacked fluorescence images and reconstruction of the fibers in 3D.

4.2.7.5. Statistical Analysis

Statistical analysis was applied to compare the difference between means of control and sample in a number of instances. To evaluate the independent distributions, the resulting data were subjected to the Shapiro-Wilk normality test, Levene's test of homogeneity of variance, and univariate ANOVA with the Games-Howell test to establish the significance of the differences between means. All statistical calculations were performed using SPSS Statistics 23 (IBM, USA). The Dixon's Q test was applied to detect outliers in the groups, and in each case these were removed.

4.3. Results and Discussion

4.3.1. Effect of Changing Polymer Concentration on Fibre Diameter and Construct Properties

PCL, a synthetic biopolymer, was chosen for its biocompatibility, biodegradability, robust mechanical properties and established record in tissue engineering and solution electrospinning research ^{73,179,193,217,269,272,273}. Additionally, PCL is a water stable ²⁷⁴, slowly degrading over years *in vivo* ²⁷⁵, making it a feasible biomaterial for encapsulation in highly water swollen GGMA. The solvents chosen for PCL were acetic and formic acid, based on an effective formulation by Luo et al.²⁶⁹. The use of this binary solvent system has a number of advantages. The boiling points of both solvents are greater than 100 °C, making them considerably less volatile than alternatives (e.g. chloroform). This prevents clogging issues at the capillary outlet as a result of solvent evaporation, allowing the process to continue for the extended periods necessary for this technique. Additionally, binary systems can drastically reduce the diameter of fibres produced, as shown by Van der Schueren *et al.* ⁷³. However, the ester bond scission by acid catalyzed hydrolysis does pose an issue for this solution based system, which may lead to time dependent fluctuation in solution properties and thus fiber properties. Importantly, the method used here acts to minimise this, by using freshly prepared solutions in production.

Hydrogel encapsulation was used to retain the integrity of the porous fiber architectures in 3D, without the support of the rigid electrode pillars. Ideally, the architecture fiber network would be self-supporting. Micro/nanofibers of PCL would require a high density of structural latticework to achieve a free-standing structure. This can be produced using direct writing approaches (e.g. MEW) however currently these methods do not produce structures at the volume needed for TE. In future studies, free standing structures by SNFES could be achieved through the use of much more rigid polymer materials, e.g. carbon nanofibers. However, for the purposes of TE, these materials would be too rigid.

A variety of PCL concentrations in AA:FA (3:1) were tested as individual samples. Viscosity of PCL as a function of polymer concentration in solution is shown Figure 4.2 (A) for a shear

rate of 10 Hz. The viscosities of the solutions were reasonably constant as a function of shear rate in each case for the range of 0.1 - 100 Hz (see Supplementary Information, Figure 4.5).

To investigate the effect of PCL solution concentration, an *Si* pattern of 15 iterations was used to generate fiber array samples as shown in Figure 4.2 (B), with a magnified image of the array in Figure 4.2 (C). In Figure 4.2 (D) fibre number as a function of PCL concentration was compared, with the greatest mean fiber number generated (49) for solution concentration of 10 wt%, with a secondary peak at 20 wt% (44), followed by a decrease minimum at 25 wt% (23). However, the variation in the 10 wt% case is far greater than other tested values for concentration, and may indicate a degree of instability in the jet cohesivity. This variation may be the result of differing printabilities of the polymer concentrations based on the solution characteristics, such as viscosity which affects the surface tension of the solution.

SEM images in Figure 4.2 (E) show representative fibers for several concentrations, illustrating the increase in fiber diameter with increasing solution concentration. The mean fiber diameter was quantified from SEM micrographs as a function of solution concentration presented as the mean \pm s.d. of $n \geq 4$ independent experiments. This follows an exponential trend (with exclusion of outlying data point at 22.5 wt%) (Figure 4.2 (F)), and this may be due to the increasing viscosity of the solution leading to a larger taylor cone point on the droplet.

Samples of 5 wt% were found not to effectively produce arrays consistently (data not shown), and were not considered in further experiments. Additionally samples generated from solution concentrations of 22.5 and 25 wt% exhibited high diameter fiber arrays, as well as exaggerated drying at the outlet and were not considered for further encapsulation experiments as the diameter was far outside the scope for tissue engineering purposes.

Concentration of 10 wt% achieves the lowest mean fibre diameter, while achieving the greatest mean fibre number per sample. Fibers with diameter below one micron have been shown to improve cell viability compared to greater diameter fibers^{30,37,39,46}, and specifically improved neural stem cell differentiation³⁷. Additionally, there is a dramatic increase in composite tensile strength, modulus and toughness as fiber diameter transitions from the

microscale to the nanoscale^{276–279}, and these strengths can be imparted when encapsulated within hydrogel matrices^{36,40,43,280}. Two known mechanisms of fiber reinforcement of hydrogels have been modeled in a finite element system by Castilho et al.¹⁵⁷. The first arises as the construct is placed under compressive force, in which the lateral expansion of the hydrogel is reinforced by the tension of the viscoelastic fibers. In the second mechanism, strength arises as fibers arrest propagating cracks in the gels²⁸⁰. The major objective is to present fibrous scaffolding for cellular behaviour enhancement. In previous research, sub micron fibrous scaffolding achieved this to the greatest extent^{30,37,46}, and fiber alignment provides contact guidance^{47–50}, and so these are major objectives in this work. A further goal of this study is to enhance the mechanical properties of the GGMA hydrogel by the mechanisms described.

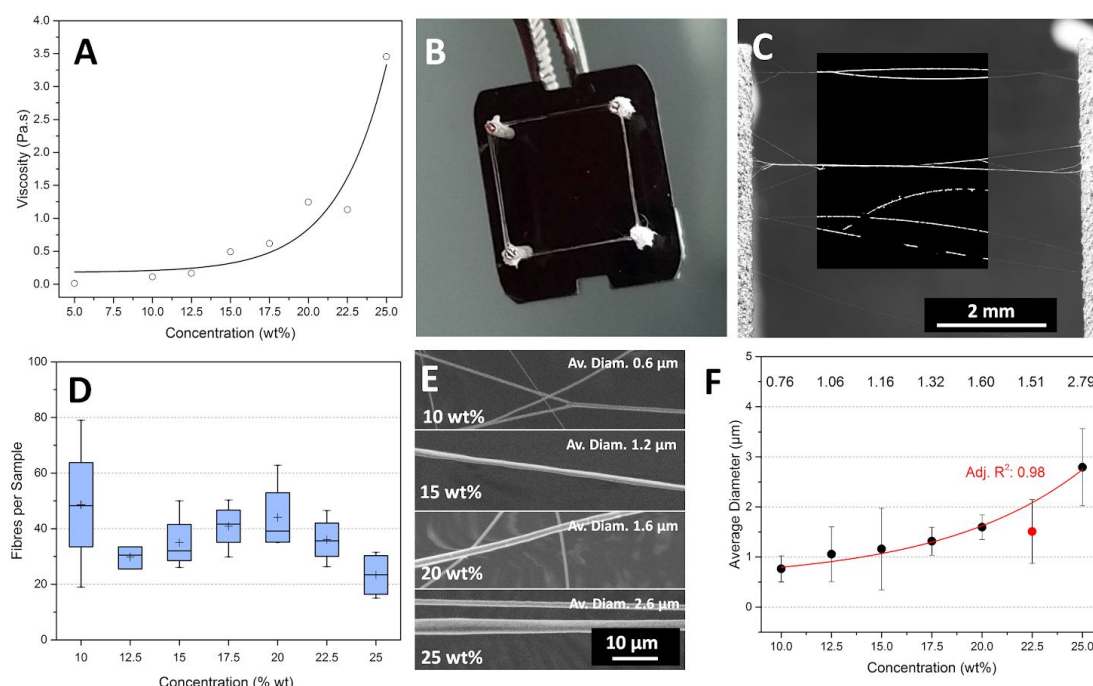


Figure 4.2. (A) Viscosity of PCL solutions in AA:FF (3:1) as a function of concentration at shear rate of 10 Hz. (B) Fibers suspended on four-pillar electrode in *Si* pattern. (C) Fiber array spanning the region between two electrodes, with segmented background black-box region in the centre for visual clarity, typical of that which is used in image analysis. (D) Average number of fibres as a function of PCL concentration. (E) Representative SEM images of fibers generated using solutions of 10, 15, 20 and 25 wt% concentration. (F) Average diameter of fibres as a function of PCL concentration. Data are presented as average

of $n \geq 4$ independent experiments. Illustrative fitting (red) is an exponential with an adjusted R^2 value of 0.98 and which excludes outlier 22.5 wt%.

The process for incorporation of the fiber arrays into the GGMA hydrogels is shown in Figure 4.3 (A), involving a straightforward UV curing method of the hydrogel after immersion of the electrodes with the fiber arrays. Through observations of the collector electrodes after their removal from the crosslinked GGMA, occasionally fibers would remain on the collector electrodes, i.e. those fibers that remained strongly attached to the electrode, as well as fibers patterned out of range of the encapsulation.

At low fiber volume fractions, as is in this construct, the tension of the viscoelastic fibers reinforcement is the most effective/dominant factor¹⁵⁷. The stress vs. strain response varies in phase from 0 to $\pi/2$ for elastic to viscous materials. Hydrogels are viscoelastic and have a phase value between these extremes. The compressive storage modulus (E') of viscoelastic materials represents the elastic component, while the loss modulus (E'') represents the energy dissipative, viscous component. Cyclic loading and unloading, over a range of frequencies, was applied to test the compressive storage and loss moduli for pure GGMA (control) and GGMA with incorporated PCL fiber arrays (GGMA-array). Figure 4.3 (B) shows the average storage modulus E' as a function of frequency for the control and different GGMA-array samples. In Figure 4.3 (B), different coloured data refer to the PCL solution concentrations used to produce the incorporated fiber arrays, with their corresponding average fiber diameter value denoted in the legend. Evidently, compared to pure GGMA, there is a clear increase in storage modulus E' after incorporation of the nanofiber array. Figure 4.3 (C) further illustrates the change in storage modulus (obtained at 1 Hz only) as a function of PCL solution concentration (or fiber diameter). Most notably in the lowest diameter fiber constructs, produced with 10 wt% solution concentration, there is over 7 fold increase in average E' (1.28 ± 0.24 kPa) compared with control sample (0.17 ± 0.24 kPa). At all solution concentrations > 10 wt%, the average E' showed a subsequent decrease to values between $\sim 0.5 - 1$ kPa.

Nanofibers have a greater aspect ratio, specific surface area and molecular chain alignment, than their micrometer diameter counterparts; each of these factors contributing to improvements in modulus, strength, and toughness²⁸¹. For example, when researchers Chew

et al. reduced fiber diameter from 5 μm to 200-300 nm, the modulus went from 300 to 3200 MPa²⁸², with similar effects seen in work by Hwang et al.²⁷⁸. Low aspect ratio (short, high diameter) fibers have poor reinforcement properties due a greater propensity to agglomerate, and a lessened fiber to matrix transfer of external force. Nanofibers exhibit aspect ratios hundreds of times higher than that of microfibers. High strain rates and draw ratio induce molecular orientation along the fiber axis during electrospinning, as observed in TEM, AFM and Raman spectroscopy²⁸³. In addition to this effect, a greater molecular alignment is achieved with low diameter fibers, where the thinner the fiber the more constrained the chain molecules, forcing alignment in-axis²⁸⁴. This alignment is associated with improved mechanical properties in-axis. The 7 fold increase in average E' can be attributed to a combination of these factors, arising as a result of the reduction in fiber diameter to the nanoscale.

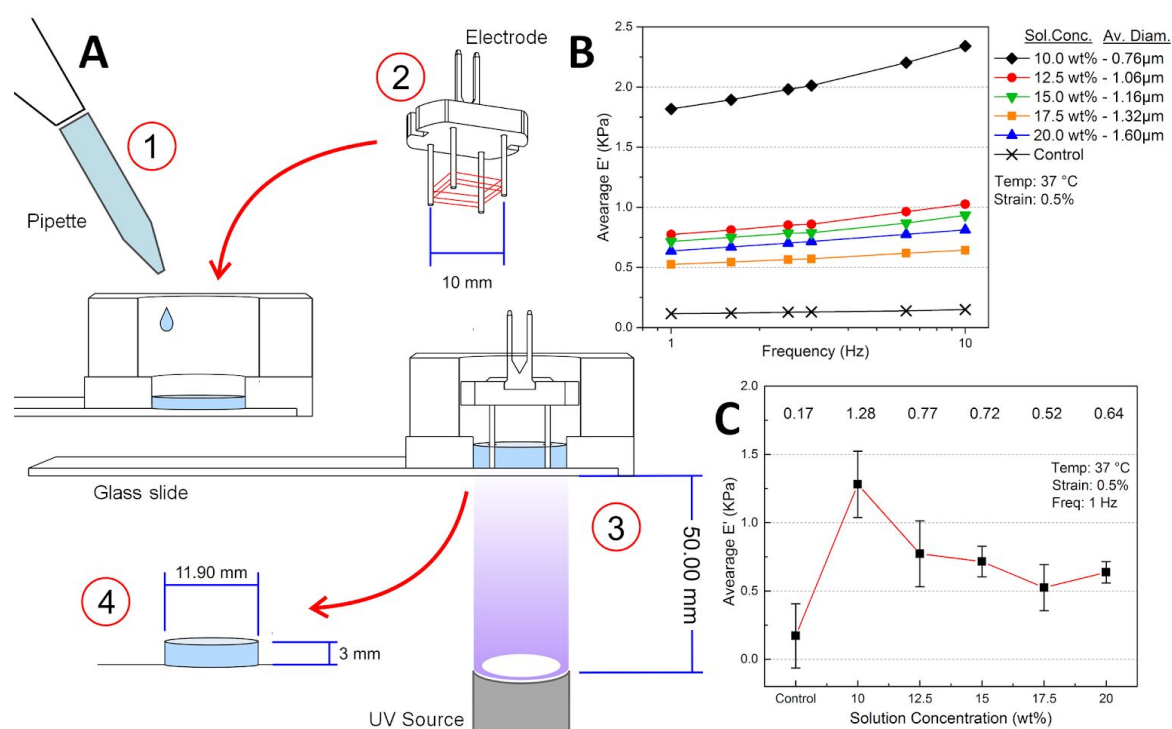


Figure 4.3. Characterisation of GGMA-Array constructs with arrays of varying fiber diameter. (A) Curing process schematic. (1) Addition of GGMA-LAP solution into the mould. (2) Addition of four-pillar electrode hosting PCL nanoarray. (3) UV curing from below. (4) Dimensions of a single hydrogel sample. (B) The average E' (compressive storage modulus) for samples incorporating fiber arrays generated using varying PCL concentration

in solution, as well as control samples of curing time 120 s. (C) Graph of the average E' of GGMA-Array constructs at specific frequency 1 Hz.

4.3.2. Effect of Changing Iteration and Electrode Structure on Fiber Array and Construct Properties

Figure 4.4 (A) and (B) shows fiber arrays suspended on four- and eight-pillar electrodes, reflecting the *Si* and *CSi* patterns, respectively, using an iteration of 60. The fiber density is visibly greater, compared to 15 iteration samples in each case (See Supplementary Figure 4.6). Figure 4.4 (C) shows representative SEM examples of the fibers generated for each condition. Figure 4.4 (D) shows the scatter plot of average fiber diameter as a consequence of changing electrode type and iterations used. Despite the increase in fiber diameter for an iteration of 60, a direct comparison between *Si* groups to elucidate the iteration effect is inappropriate, as different process parameters such WD and voltage are used in each case. A comparison could be made however between *CSi* (15) with *CSi* (60), in which we see a significant fiber diameter increase with iteration. This increase may be as a consequence of a greater number of fiber bundling or fusing events in 60, leading to an apparent increase in fiber size.

The mean E' storage modulus of GGMA-fiber arrays, produced from the two different patterns with low and high iterations, as a function of frequency is shown in Figure 4.4 (E). An increased fiber density would be expected to reinforce the GMMA^{157,285}. Previous research showed that the number, or mass, of conventionally electrospun nanofibers within a composite had a significant effect on the properties²⁸⁶. Figure 4.4 (E), showing the average E' for each pattern/iteration, unexpectedly revealed that the lower iteration (density) *Si* pattern gave an increase in E' while the reverse was the case for *CSi* patterning. For each case, the inclusion of fibrous arrays achieved an enhancement of the hybrid E' compared with the control. However, in Figure 4.4 (F) (obtained at 1 Hz only) the large E' variability in *Si* (15) is illustrated, and statistical analysis did not reveal statistical significance to $p < 0.05$ between any mean value. Improvements in control and increases in density were achieved with increasing iteration, as shown in *Si* (15) to *Si* (60) (Figure 4.4 (F)). The precisional deposition

in CSi patterning lacks consistency particularly in the inner region (See Supplementary Figure 4.6). This may be as a consequence of the complexity of the pattern motion and electrode design, leading to a position dependent electric field variation, with changing vector strength, which may destabilise jetting consistency.

There are a number of possible explanations for the above results, illustrated in Figure 4.4 (E-F) . Firstly, this result could be a consequence of the electrode extraction method illustrated in Figure 4.3 (A). Withdrawing the electrodes from the hydrogel leads to the destruction of the fiber array to some extent. During withdrawal of the electrodes from the hydrogel, the fibers encapsulated in the hydrogel are subject to a pulling force and detach from the electrodes. The perturbation of the fiber array in terms of alignment and integrity, may generate variability in the mechanical reinforcement, leading to a variability, seen in *Si* (15). The eight-pillar electrodes have a higher number of attachment points for the suspended fiber array, increasing the likelihood that the fiber array structure will be compromised during withdrawal of the electrodes. This may account for the greater E' of *Si* (15) on four-pillar electrodes, despite *CSi* (60) having a greater fiber density. This would require further investigation of removal techniques, to mitigate any losses incurred during the process.

To visualise the fibers within the hydrogel, SEM and confocal microscopy was applied. Confocal imaging managed to extract an example fiber in the hydrogel reconstructed in 3D, see Supplementary video 4.1. Confocal imaging did not lead to clear observations, due to the dissolution of fluorescein into the hydrogel, as well as the limited depth capabilities of confocal imaging. SEM imaging of sectioned samples, did not result in clear observations of fiber arrays, due in part to the size as well as the low volume fraction of the fibers. Lastly, in the previous study (section 3.1) smaller fibers provided greater reinforcement (as seen in Figure 4.3 (C)). In light of this, the submicron fiber diameter in *Si* (15) patterns may contribute to the increased E' through further investigation, alongside confirmation of the encapsulated fiber arrays, is required.

Analysis using short range fluorescence microscopy (~200 μ m depth of penetration) had limited success showing only individual single fibres. A useful analyte in these experiments would be the porosity of the fiber array. The characterisation necessary to accurately and

systematically analyse the porosity of micro/nanofibrous array structures in 3D includes: (i) Mercury porosimetry, (ii) nano-CT, (iii) long range fluorescence microscopy. Unfortunately (i) requires pressures deemed likely to be destructive for samples while (ii) and (iii) are non destructive but prohibitively expensive technologies. In future work with reducing costs of nano CT technologies, it is hoped that a thorough analysis of the structures porosity and polar orientational distribution can be completed.

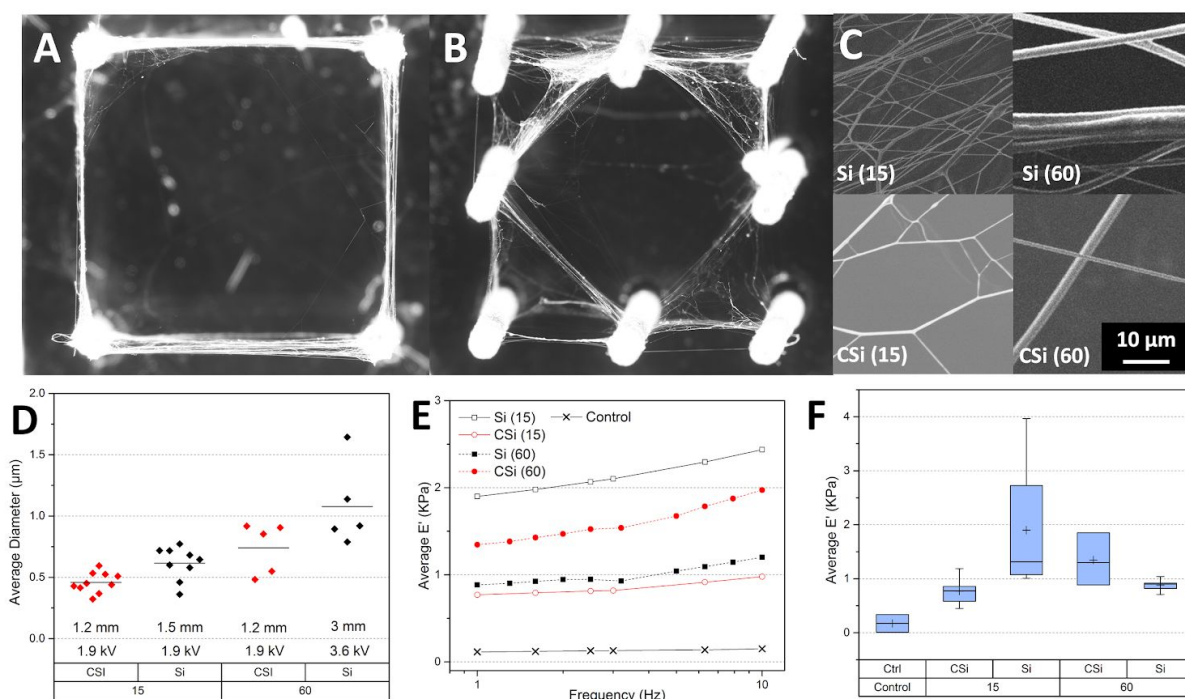


Figure 4.4. Iteration and electrode variation. (A) Microscopy image of four-pillar electrode with attached array generated at 60 iteration of *Si* pattern, and of (B) *CSi* pattern. (C) SEM images of PCL fiber array for each individual condition each at equal scale. (D) Plot of diameter for varying iteration and electrode conditions, with bar indicating mean for each group. (E) DMA isothermal frequency sweep, average storage modulus E' for varying conditions of iteration and electrode. (F) Boxplot showing the distribution of average storage modulus at 1 Hz frequency.

In the gel-forming solution, GGMA long chain molecules wrap around the spun fibres, causing the chains to separate. When a methacrylated hydrogel covalently crosslinks the molecules link together by their methacrylate groups. This would lead to negligible changes in their positions, with minimal resulting tension. No visible contraction of the bulk gel took place, with no excessive tension due to contraction placed on the fiber array structure. Gellation held the fiber arrays in place and, once the pillars were removed, intact fibers were observed within the gel, suggesting that no destructive transverse forces were introduced during gelation.

The fused titanium electrodes exhibited a roughened surface at the microscale (by SEM analysis), with slight increases in smoothness between the grade 5 and the grade 23 Ti powders used. The electrode material is best suited for medical applications, while other metals may be incompatible. In the future copper (as well as other materials) may be used, as material compatibility of SLM is expanded. The electrode designs were chosen to fit well within 24 well plates (~15.6mm diameter), with a view to use the electrodes in future systematic cell studies. The electrodes were 10 mm in height, 0.6 mm in diameter (near minimum resolution of SLM for free standing pillars), with maximum interpillar distance of 10 mm diagonally. Minimum pillar interspacing was varied, where the 8 pillar electrode variant increased the density of pillars relative to 4 pillar. This decrease in pillar interspacing showed a decrease in fiber diameter between 4 to 8-pillar electrodes (See Figure 4.4. D). The 8-pillar variant also holds a greater capacity for varied patterns, allowing an increased fiber density in the central space between pillars using the CSi pattern. There remain several electrode factors yet to be investigated and the design space can expand further in future studies as the fundamentals of this technique are examined.

The nanofibrous protein structures of the matrix provide cues to neural stem cells, and as such, the interest in nanomaterials for biomimetic scaffolds has led to advances, as well as challenges for 3D cell culture nanofabrication ²⁸⁷. To address the challenges of 3D nanofabrication, SNFES with SLM manufactured electrodes provides an interesting approach for producing greater volume nanofibrous scaffolds; feasibly, with the current system, up to 14 mm in height. Whilst in this study the collector electrodes were removed for the purpose of determining the effects of fiber arrays on the hydrogel storage modulus, in future they could conceivably be left in the hydrogel as a means to provide electrostimulation during in vitro studies.

4.4. Conclusions

In this study, the suspension electrowriting technique, SNFES, was employed to fabricate ultrafine PCL fiber arrays across two types of collecting electrodes, using programmed patterns. These 3D scaffolds were then encapsulated within a biocompatible GGMA hydrogel matrix. This encapsulation was to provide scaffolding to mimic native nECM for tissue

engineering applications. SNFES patterning was performed on four-pillar electrodes, varying PCL solution concentration, leading to a corresponding fiber diameter change, achieving sub-micron diameter fibers $0.76 \pm 0.26 \mu\text{m}$, at concentrations of 10 wt%. GGMA-Array samples were measured by unconfined compressional DMA, and it was found that encapsulation led to increases in the constructs' mechanical properties.

The greatest effect was seen in constructs with sub-micron diameter fibres, which raised the storage modulus from 0.17 (control) to 1.28 kPa, with native brain tissue elastic modulus typically in the range of 0.5 - 1 kPa ³¹. A second eight-pillar electrode was implemented, to examine the effects of electrode configuration. On both four- and eight-pillar electrodes, comparisons were made of fiber arrays generated using typical and high pattern iteration, to examine fiber density effects. In this case, the mechanisms responsible for the change in storage modulus with increasing fiber density, were complicated by the confounding effects of fiber diameter as well as the perturbing withdrawal of collectors from the hydrogel.

The constructs produced have potential use in neural tissue engineering, providing scaffolding beneficial for cell viability, behavior and contact guidance; in a 3D biocompatible hydrogel matrix which can be tuned to mimic the elastic modulus of native neural tissue.

4.5. Acknowledgements

The authors acknowledge the financial support of the Australian Research Council (ARC) Centre of Excellence Scheme (Project CE 140100012). The authors thank the Australian National Fabrication Facility (ANFF) for providing facilities for the fabrication of the NFES system components. The authors thank the University of Wollongong Electron Microscopy Centre (EMC) for providing SEM facilities. The authors thank Mr. Grant Barnsley for his support in the fabrication of pillar electrodes, and Dr. Paul Molino for his assistance in performing confocal microscopy.

4.6. Supplementary Section

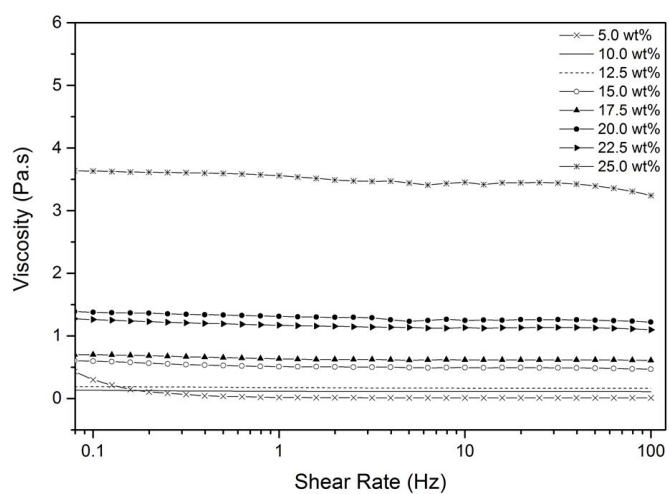


Figure 4.5. Viscosity of PCL solutions as a function of shear rate.

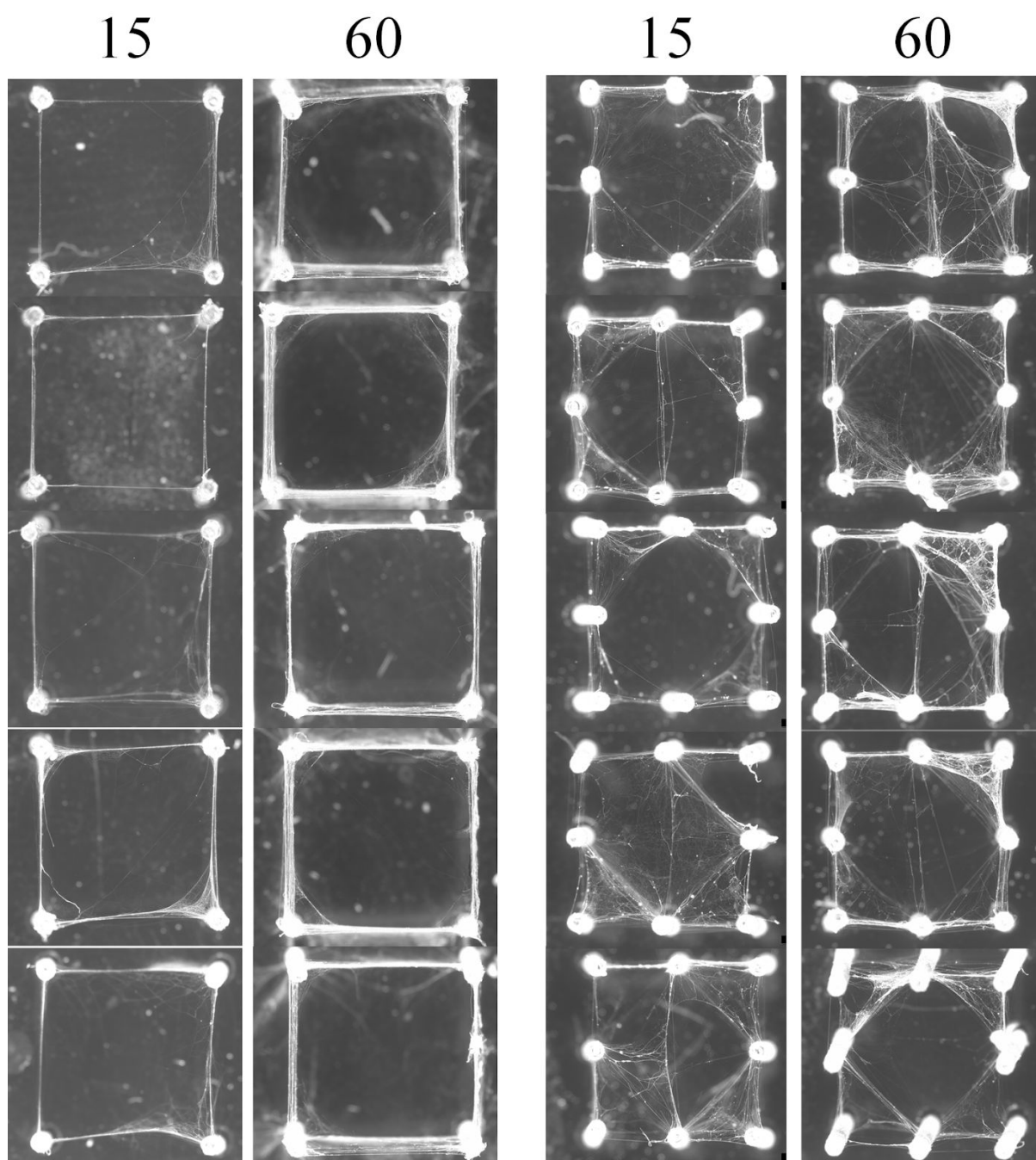


Figure 4.6. Microscopy of fiber arrays on four- and eight-pillar electrodes with varying iteration (15, 60)

Supplementary video 4.1. Animation of confocal image of fiber, emanating from the electrode void space.

Chapter 5. Conclusions and Future Perspective

5.1. Conclusions

The major goal in this thesis was to mimic the nanofibrous proteins found in the neural extracellular matrix (nECM). NFES is a versatile nanofiber patterning technique, utilising additive layer-by-layer deposition to create nanofibrous microstructures. However, by this layer-by-layer method, high volume can be difficult to achieve due to inhibition of the ejection process by polymer build-up. The question of how to overcome this limitation, to mimic the 3D nECM, led to the development of a new technique: Suspension Near-Field Electrospinning (SNFES), which allowed the direct suspension of ultrafine polymer arrays.

This goal necessitated the development of a direct electro-write system as detailed in Chapter 2. The instrumentation and platform control software were successfully implemented to achieve complex, high accuracy patterning on 2D silicon wafer. Four-pillar 3D titanium electrode substrates were then fabricated by Selective laser melt (SLM). Platforms for mounting the electrodes were employed and the SNFES technique was developed to achieve suspended fibrous arrays, by direct patterning on the electrodes. This involved interpillar motion of the emitter to draw fibers suspending them between the pillars. Initial findings, testing raster patterning, showed that humidity had a dramatic effect on the spinnability of the PEO solution, with success at 30-50% RH, while no success at 50-62% RH. The need for humidity control led to the development of a low humidity air supplied acrylic case.

Higher iteration experiments were performed, managing square iterative patterning over periods up to and over 1 hour of operation. This extended operation necessitated the development of an automated cleaning device, to handle clogging issues periodically. The suspended nanofibrous arrays produced were analysed for their orientation distribution and diameter. It was shown that fiber orientation aligned with patterning toolpaths, which achieved an average fiber diameters below one micron. This study explored simplistic patterning geometries, as a necessary first step towards more complex structures to meet the needs of tissue engineering.

The next step in this research was to investigate the process parameters and pattern iteration effects of SNFES through orthogonal experiments, discussed in Chapter 3. This examined the ultrafine fiber array structures in terms of distribution, fiber number and diameter. This specifically investigated varying working distance, maximum stage speed, voltage and PEO solution concentration. The second section produced high density nanofiber meshes of PEO, varying the number of iterations. The need for more complex structures in TE, led to the development of further pattern types, working around the simple four-pillar structure, to produce crossing arrays.

Fiber arrays were studied by light and scanning electron microscopy, determining orientation distribution, number and diameter. This revealed effects with respect to variation in diameter, fiber alignment and relative fiber density; and identified capabilities of the technique, finding more optimal process settings for nanoarray suspension. In the majority of cases the alignment of the arrays was accurate to $\pm 5^\circ$. Diameter was modulated by the process parameters; while the increase in iteration led to density which exponentially decayed by the electrostatic inhibitory effects of polymer build up at the collector.

The final major objective was to incorporate ultrafine fiber arrays into a hydrogel matrix, to mimic both the nanofibrous proteins and the mechanical properties of the nECM. In order to achieve a 3D substrate for cell proliferation, ultrafine polycaprolactone (PCL) arrays were encapsulated within a biocompatible gellan gum methacrylate (GGMA) hydrogel matrix, described in Chapter 4. It was found that fiber encapsulation led to dramatic improvements in the constructs mechanical properties, raising the storage modulus by up to seven fold. Parametric studies varying fiber diameter, as well as electrode pillar design and pattern iteration; elucidated the encapsulated array effects. A second, eight-pillar electrode was implemented, and iteration variation studies were performed to understand the effect of increased fiber density on mechanical reinforcement of the matrix.

The most dramatic hydrogel reinforcements were found upon minimising the fiber diameter below 1 micron; raising the storage modulus from 0.17 to 1.28 kPa. The results of these studies can enable the design of targeted mechanical reinforcement of the weak GGMA hydrogel, to match the properties of the nECM. Not only does the array structure provide

biomimetic nano-scaffolding beneficial for cell viability, it mechanically reinforces the weak hydrogel matrix to within and above neural tissue norms.

The findings of this research are significant as it creates for the first time a suspended polymer nanoarray, in a directed manner, which can be extended across multiple working 3D planes *in situ*. Significantly, this is the first time the technologies of selective laser melt manufacturing and NFES have been combined. In conclusion, ultrafine fiber arrays were prepared using the new technique SNFES, and encapsulated in the GGMA hydrogel. Our research contributes to the growing number of techniques in 3D electrowriting, nanofabrication and microtissue construct technologies. The scaffold nanostructures are large enough for use in microtissue constructs for the medical research sector, and can be tailored based on the findings of the parametric experiments. The increase in nanoarray volume and density achieved here is expected to address challenges of producing hierarchical tissue constructs in 3D.

5.2. Future Perspectives

The tissue constructs produced in this research have potential application as part of an *in vitro*, benchtop, cell culture system; for low elastic moduli tissues such as the nECM. The hybrid constructs produced herein, can be tuned to have similar mechanical elastic modulus as nECM, in the region of 0.5 - 1 kPa ³¹. A logical continuation of this work, involves extensive biocompatibility studies; beyond the scope of this research. These would aim to evaluate the hybrid constructs produced through neural cell tissue culture experiments. A mixture of neuroblastic cells and eosinophilic cells, could be used in differentiation and proliferation studies in a biocompatible GGMA-Array matrix. This array could be modified by pattern, density and fiber diameter to investigate their modifying effects on cellular behaviour. Confocal fluorescence microscopy as well as μ CT measurements of the suspended arrays could then be used to reconstruct fiber and cellular 3D distribution.

A titanium SLM manufactured electrode pillar array, built to investigate 3D electrostimulation of cells in media, was the initial inspiration for four- and eight-pillar electrode designs. The structure of this electrostimulation electrode was relatively complex and was not considered for the purposes of the SNFES experiments. Now the effects of SNFES are better understood, further experiments can incorporate this model. Retaining the developed pillar electrodes within the matrix construct can provide *in vitro* electrical stimulation as well as structural guidance nanoarchitectures for cell culture. This can allow the study of cell–nanofiber interactions in combination with local electrostimulation, potentially producing significant insights in tissue engineering research.

For NFES, many advances in the future will rely on complex automated systems, which would promote technique repeatability, enhance process monitoring, and accelerate protocol development. Automation systems can rely on feedback mechanisms such as: machine vision ^{196,197,288}, physical triggers, as well as electrical ²⁸⁹ and environmental monitoring. Camera-computer systems ²⁹⁰ can use machine vision to continuously measure/observe SNFES phenomena, such as: the droplet size and shape ¹⁹⁸; and object separation *i.e.* emitter to pillar electrode distance allowing automated calibration. The electrohydrodynamic (EHD) jet printing method has established the effective control of NFES jetting through voltage

waveform control ^{198,291,292}. In a similar fashion, SNFES can be advanced by including a variable voltage control system within the program. This, combined with object separation machine vision, could allow the automated control of electric field strength. Additional automated systems that could work in isolation include commercially sourced ambient temperature and humidity control and active vibration isolation systems.

In order to achieve improved SNFES accuracy and reproducibility, electrode systems can be advanced by: generating new structures and patterns; and modifying electrodes to have locally insulated elements thereby modifying the local electric field. Furthermore the SNFES technique can be upgraded by developing a selectively charged electrode procedure, as in work by Kai *et al.* ¹⁷⁶, allowing experiments into dynamic field control for SNFES. Automation, increased density and fine control in 3D will be the next great challenge for this emerging technology.

References

1. Nagle, A. R. *et al.* A direct 3D suspension near-field electrospinning technique for the fabrication of polymer nanoarrays. *Nanotechnology* **30**, 195301 (2019).
2. Nagle, A. R. *et al.* Patterning and process parameter effects in 3D suspension near-field electrospinning of nanoarrays. *Nanotechnology* (2019) doi:10.1088/1361-6528/ab3c87.
3. Zhao, C., Deng, W. & Gage, F. H. Mechanisms and functional implications of adult neurogenesis. *Cell* **132**, 645–660 (2008).
4. Pettikiriarachchi, J. T. S., Parish, C. L., Shoichet, M. S., Forsythe, J. S. & Nisbet, D. R. Biomaterials for brain tissue engineering. *Aust. J. Chem.* **63**, 1143 (2010).
5. Tysseling, V. M. & Kessler, J. A. Biomaterials for central nervous system regeneration. in *Comprehensive Biomaterials* 455–466 (2011).
6. Zhong, Y. & Bellamkonda, R. V. Biomaterials for the central nervous system. *J. R. Soc. Interface* **5**, 957–975 (2008).
7. A randomized, controlled trial of methylprednisolone or naloxone in the treatment of acute spinal-cord injury. *N. Engl. J. Med.* **323**, 1207–1209 (1990).
8. Maas, A. I. R., Marmarou, A., Murray, G. D. & Steyerberg, E. W. Clinical trials in traumatic brain injury: current problems and future solutions. in *Mechanisms of Secondary Brain Damage from Trauma and Ischemia* 113–118 (2004).
9. Kalladka, D. *et al.* Human neural stem cells in patients with chronic ischaemic stroke (PISCES): a phase 1, first-in-man study. *Lancet* **388**, 787–796 (2016).
10. Steinberg, G. K. *et al.* Clinical outcomes of transplanted modified bone marrow-derived mesenchymal stem cells in stroke: a phase 1/2a study. *Stroke* **47**, 1817–1824 (2016).
11. Baker, E. W., Kinder, H. A. & West, F. D. Neural stem cell therapy for stroke: A multimechanistic approach to restoring neurological function. *Brain Behav.* **9**, e01214 (2019).
12. Bible, E. *et al.* Neo-vascularization of the stroke cavity by implantation of human neural stem

- cells on VEGF-releasing PLGA microparticles. *Biomaterials* vol. 33 7435–7446 (2012).
13. Jin, K. *et al.* Transplantation of human neural precursor cells in Matrigel scaffolding improves outcome from focal cerebral ischemia after delayed postischemic treatment in rats. *J. Cereb. Blood Flow Metab.* **30**, 534–544 (2010).
 14. Dodson, B. P. & Levine, A. D. Challenges in the translation and commercialization of cell therapies. *BMC Biotechnol.* **15**, 70 (2015).
 15. Mason, C., Brindley, D. A., Culme-Seymour, E. J. & Davie, N. L. Cell therapy industry: billion dollar global business with unlimited potential. *Regen. Med.* **6**, 265–272 (2011).
 16. Johnson, P. J., Tatara, A., Shiu, A. & Sakiyama-Elbert, S. E. Controlled release of neurotrophin-3 and platelet-derived growth factor from fibrin scaffolds containing neural progenitor cells enhances survival and differentiation into neurons in a subacute model of SCI. *Cell Transplantation* vol. 19 89–101 (2010).
 17. Karimi-Abdolrezaee, S., Eftekharpour, E., Wang, J., Morshead, C. M. & Fehlings, M. G. Delayed transplantation of adult neural precursor cells promotes remyelination and functional neurological recovery after spinal cord injury. *J. Neurosci.* **26**, 3377–3389 (2006).
 18. Skop, N. B., Calderon, F., Cho, C. H., Gandhi, C. D. & Levison, S. W. Improvements in biomaterial matrices for neural precursor cell transplantation. *Mol Cell Ther* **2**, 19 (2014).
 19. Berthiaume, F., Maguire, T. J. & Yarmush, M. L. Tissue engineering and regenerative medicine: history, progress, and challenges. *Annu. Rev. Chem. Biomol. Eng.* **2**, 403–430 (2011).
 20. Riquelme, P. A., Drapeau, E. & Doetsch, F. Brain micro-ecologies: neural stem cell niches in the adult mammalian brain. *Philos. Trans. R. Soc. Lond. B Biol. Sci.* **363**, 123–137 (2008).
 21. Palmer, T. D., Takahashi, J. & Gage, F. H. The adult rat hippocampus contains primordial neural stem cells. *Mol. Cell. Neurosci.* **8**, 389–404 (1997).
 22. Mercier, F., Kitasako, J. T. & Hatton, G. I. Anatomy of the brain neurogenic zones revisited: fractones and the fibroblast/macrophage network. *J. Comp. Neurol.* **451**, 170–188 (2002).
 23. Jin, K. *et al.* Vascular endothelial growth factor (VEGF) stimulates neurogenesis in vitro and in

- vivo. *Proc. Natl. Acad. Sci. U. S. A.* **99**, 11946–11950 (2002).
24. Hynes, R. O. The extracellular matrix: not just pretty fibrils. *Science* **326**, 1216–1219 (2009).
 25. Tian, L., Prabhakaran, M. P. & Ramakrishna, S. Strategies for regeneration of components of nervous system: scaffolds, cells and biomolecules. *Regen Biomater* **2**, 31–45 (2015).
 26. Abbott, A. Cell culture: Biology's new dimension. *Nature* **424**, 870–872 (2003).
 27. Weaver, V. M. *et al.* Reversion of the malignant phenotype of human breast cells in three-dimensional culture and in vivo by integrin blocking antibodies. *J. Cell Biol.* **137**, 231–245 (1997).
 28. Wolf, K. *et al.* Compensation mechanism in tumor cell migration: mesenchymal-amoeboid transition after blocking of pericellular proteolysis. *J. Cell Biol.* **160**, 267–277 (2003).
 29. Mirzadeh, Z., Merkle, F. T., Soriano-Navarro, M., Garcia-Verdugo, J. M. & Alvarez-Buylla, A. Neural stem cells confer unique pinwheel architecture to the ventricular surface in neurogenic regions of the adult brain. *Cell Stem Cell* **3**, 265–278 (2008).
 30. Kijęńska, E., Prabhakaran, M. P., Swieszkowski, W., Kurzydłowski, K. J. & Ramakrishna, S. Interaction of Schwann cells with laminin encapsulated PLCL core-shell nanofibers for nerve tissue engineering. *Eur. Polym. J.* **50**, 30–38 (2014).
 31. Gefen, A. & Margulies, S. S. Are in vivo and in situ brain tissues mechanically similar? *J. Biomech.* **37**, 1339–1352 (2004).
 32. Den Dunnen, W. F. A. *et al.* Biological performance of a degradable poly(lactic acid- ϵ -caprolactone) nerve guide: Influence of tube dimensions. *J. Biomed. Mater. Res.* **29**, 757–766 (1995).
 33. An, J., Chua, C. K., Leong, K. F., Chen, C.-H. & Chen, J.-P. Solvent-free fabrication of three dimensionally aligned polycaprolactone microfibers for engineering of anisotropic tissues. *Biomed. Microdevices* **14**, 863–872 (2012).
 34. Södergård, A. & Stolt, M. Properties of lactic acid based polymers and their correlation with composition. *Prog. Polym. Sci.* **27**, 1123–1163 (2002).

35. Lee, H. & Kim, G. Enhanced cellular activities of polycaprolactone/alginate-based cell-laden hierarchical scaffolds for hard tissue engineering applications. *J. Colloid Interface Sci.* **430**, 315–325 (2014).
36. Shin, S. R. *et al.* Carbon nanotube reinforced hybrid microgels as scaffold materials for cell encapsulation. *ACS Nano* **6**, 362–372 (2012).
37. Yang, F., Murugan, R., Wang, S. & Ramakrishna, S. Electrospinning of nano/micro scale poly(L-lactic acid) aligned fibers and their potential in neural tissue engineering. *Biomaterials* **26**, 2603–2610 (2005).
38. Yang, F., Xu, C. Y., Kotaki, M., Wang, S. & Ramakrishna, S. Characterization of neural stem cells on electrospun poly(L-lactic acid) nanofibrous scaffold. *J. Biomater. Sci. Polym. Ed.* **15**, 1483–1497 (2004).
39. Coburn, J. M., Gibson, M., Monagle, S., Patterson, Z. & Elisseeff, J. H. Bioinspired nanofibers support chondrogenesis for articular cartilage repair. *Proc. Natl. Acad. Sci. U. S. A.* **109**, 10012–10017 (2012).
40. Visser, J. *et al.* Reinforcement of hydrogels using three-dimensionally printed microfibres. *Nat. Commun.* **6**, 6933 (2015).
41. Coburn, J. *et al.* Biomimetics of the extracellular matrix: an integrated three-dimensional fiber-hydrogel composite for cartilage tissue engineering. *Smart Structures and Systems* vol. 7 213–222 (2011).
42. Xu, T. *et al.* Hybrid printing of mechanically and biologically improved constructs for cartilage tissue engineering applications. *Biofabrication* **5**, 015001 (2013).
43. Bosworth, L. A., Turner, L.-A. & Cartmell, S. H. State of the art composites comprising electrospun fibres coupled with hydrogels: a review. *Nanomedicine* **9**, 322–335 (2013).
44. Agrawal, A., Rahbar, N. & Calvert, P. D. Strong fiber-reinforced hydrogel. *Acta Biomater.* **9**, 5313–5318 (2013).
45. Xia, Z., Patchan, M., Maranchi, J., Elisseeff, J. & Trexler, M. Determination of crosslinking

- density of hydrogels prepared from microcrystalline cellulose. *Journal of Applied Polymer Science* vol. 127 4537–4541 (2013).
46. Beachley, V. & Wen, X. Polymer nanofibrous structures: Fabrication, biofunctionalization, and cell interactions. *Prog. Polym. Sci.* **35**, 868–892 (2010).
 47. Teo, W. E. & Ramakrishna, S. Electrospun fibre bundle made of aligned nanofibres over two fixed points. *Nanotechnology* **16**, 1878–1884 (2005).
 48. Pham, Q. P., Sharma, U. & Mikos, A. G. Electrospun poly(epsilon-caprolactone) microfiber and multilayer nanofiber/microfiber scaffolds: characterization of scaffolds and measurement of cellular infiltration. *Biomacromolecules* **7**, 2796–2805 (2006).
 49. Prabhakaran, M. P., Venugopal, J., Chan, C. K. & Ramakrishna, S. Surface modified electrospun nanofibrous scaffolds for nerve tissue engineering. *Nanotechnology* **19**, 455102 (2008).
 50. Vasita, R. & Katti, D. S. Nanofibers and their applications in tissue engineering. *Int. J. Nanomedicine* **1**, 15–30 (2006).
 51. Ru, C. *et al.* Suspended, shrinkage-free, electrospun PLGA nanofibrous scaffold for skin tissue engineering. *ACS Appl. Mater. Interfaces* **7**, 10872–10877 (2015).
 52. Semino, C. E., Kasahara, J., Hayashi, Y. & Zhang, S. Entrapment of migrating hippocampal neural cells in three-dimensional peptide nanofiber scaffold. *Tissue Eng.* **10**, 643–655 (2004).
 53. Gelain, F. *et al.* Transplantation of nanostructured composite scaffolds results in the regeneration of chronically injured spinal cords. *ACS Nano* **5**, 227–236 (2011).
 54. Ghorani, B. & Tucker, N. Fundamentals of electrospinning as a novel delivery vehicle for bioactive compounds in food nanotechnology. *Food Hydrocoll.* **51**, 227–240 (2015).
 55. Chang, J., Dommer, M., Chang, C. & Lin, L. Piezoelectric nanofibers for energy scavenging applications. *Nano Energy* **1**, 356–371 (2012).
 56. Li, D. & Xia, Y. Electrospinning of Nanofibers: Reinventing the Wheel? *Adv. Mater.* **16**, 1151–1170 (2004).
 57. Noguchi, H., Kang, C.-W. & Murakawa, M. Study on nanofiber spinning using centrifugal force

- rotational speed of spinning disk vs nanofiber/microfiber diameter when disk speed is increased via gears. *Sens. Mater.* **30**, 2833 (2018).
58. Hopkins, A. R., Sawall, D. D., Villahermosa, R. M. & Lipeles, R. A. Interfacial synthesis of electrically conducting polyaniline nanofiber composites. *Thin Solid Films* **469-470**, 304–308 (2004).
 59. Jin, Y., Huang, S., Zhang, M. & Jia, M. Preparation of sulfonated graphene–polyaniline nanofiber composites by oil/water interfacial polymerization and their application for supercapacitors. *Synth. Met.* **168**, 58–64 (2013).
 60. Chen, T., Yang, K. & Wu, L.-L. Fabrication of nanofiber non-wovens on the melt blowing die with air by-passes. *Thermal Science* **20**, 1006–1007 (2016).
 61. Nayak, R. *Polypropylene Nanofibers: Melt Electrospinning Versus Meltblowing*. (Springer, 2017).
 62. Wang, W. *et al.* Macroporous nanofibrous vascular scaffold with improved biodegradability and smooth muscle cells infiltration prepared by dual phase separation technique. *Int. J. Nanomedicine* **13**, 7003–7018 (2018).
 63. Sundararajan, P. R. Features of self-assembly. in *Physical Aspects of Polymer Self-Assembly* 37–104 (John Wiley & Sons, 2016).
 64. Gao, M., Guo, J., Leung, G. K. K. & Wu, W. Use of self-assembly nanofibre biomaterials for neural repair after injury. in *Advances in Nanofibers* (2013).
 65. Sui, G., Zhong, W.-H., Fuqua, M. A. & Ulven, C. A. Crystalline structure and properties of carbon nanofiber composites prepared by melt extrusion. *Macromol. Chem. Phys.* **208**, 1928–1936 (2007).
 66. Yu, B. & Li, H. Morphology and photoluminescent properties of poly(p-phenylene) nanofibre arrays fabricated by template method. *Materials Science and Engineering: A* **325**, 215–220 (2002).
 67. Chesunov, V. M. & Vasenin, R. M. The kinetics of solvent evaporation during film formation

- from polymer solutions. *Polymer Science U.S.S.R.* **9**, 2333–2338 (1967).
68. Reneker, D. H. & Chun, I. Nanometre diameter fibres of polymer, produced by electrospinning. *Nanotechnology* **7**, 216–223 (1996).
 69. Earnshaw, S. On the nature of the molecular forces which regulate the constitution of the luminiferous ether. **7**, 97 (1839).
 70. Reneker, D. H., Yarin, A. L., Fong, H. & Koombhongse, S. Bending instability of electrically charged liquid jets of polymer solutions in electrospinning. *J. Appl. Phys.* **87**, 4531–4547 (2000).
 71. Park, S. H., Kim, T. G., Kim, H. C., Yang, D.-Y. & Park, T. G. Development of dual scale scaffolds via direct polymer melt deposition and electrospinning for applications in tissue regeneration. *Acta Biomater.* **4**, 1198–1207 (2008).
 72. Zong, X. *et al.* Electrospun fine-textured scaffolds for heart tissue constructs. *Biomaterials* **26**, 5330–5338 (2005).
 73. Van der Schueren, L., De Schoenmaker, B., Kalaoglu, Ö. I. & De Clerck, K. An alternative solvent system for the steady state electrospinning of polycaprolactone. *Eur. Polym. J.* **47**, 1256–1263 (2011).
 74. Zeugolis, D. I. *et al.* Electro-spinning of pure collagen nano-fibres - just an expensive way to make gelatin? *Biomaterials* **29**, 2293–2305 (2008).
 75. Yang, W., Duan, H., Li, C. & Deng, W. Crossover of varicose and whipping instabilities in electrified microjets. *Phys. Rev. Lett.* **112**, 054501 (2014).
 76. Liu, H. & Hsieh, Y.-L. Ultrafine fibrous cellulose membranes from electrospinning of cellulose acetate. *J. Polym. Sci. B Polym. Phys.* **40**, 2119–2129 (2002).
 77. Lin, T., Wang, H., Wang, H. & Wang, X. The charge effect of cationic surfactants on the elimination of fibre beads in the electrospinning of polystyrene. *Nanotechnology* **15**, 1375–1381 (2004).
 78. Costolo, M. A., Lennhoff, J. D., Pawle, R., Rietman, E. A. & Stevens, A. E. A nonlinear system model for electrospinning sub-100 nm polyacrylonitrile fibres. *Nanotechnology* **19**, 035707

- (2008).
79. Bhattarai, N., Edmondson, D., Veis, O., Matsen, F. A. & Zhang, M. Electrospun chitosan-based nanofibers and their cellular compatibility. *Biomaterials* **26**, 6176–6184 (2005).
 80. Quigley, A. F. *et al.* Nerve repair: a conducting-polymer platform with biodegradable fibers for stimulation and guidance of axonal growth (adv. Mater. 43/2009). *Adv. Mater.* **21**, (2009).
 81. Chang, C.-J., Hsu, S.-H., Yen, H.-J., Chang, H. & Hsu, S.-K. Effects of unidirectional permeability in asymmetric poly(DL-lactic acid-co-glycolic acid) conduits on peripheral nerve regeneration: An in vitro and in vivo study. *J. Biomed. Mater. Res. B Appl. Biomater.* **83B**, 206–215 (2007).
 82. Wang, B. & De Wang, Y. Effect of fiber diameter on thermal conductivity of the electrospun carbon nanofiber mats. *Advanced Materials Research* vols 332-334 672–677 (2011).
 83. Mo, X. & Weber, H.-J. Electrospinning P(LLA-CL) nanofiber: a tubular scaffold fabrication with circumferential alignment. *Macromolecular Symposia* vol. 217 413–416 (2004).
 84. Mo, X. M., Xu, C. Y., Kotaki, M. & Ramakrishna, S. Electrospun P(LLA-CL) nanofiber: a biomimetic extracellular matrix for smooth muscle cell and endothelial cell proliferation. *Biomaterials* **25**, 1883–1890 (2004).
 85. Yoon, K. *et al.* High flux ultrafiltration membranes based on electrospun nanofibrous PAN scaffolds and chitosan coating. *Polymer* vol. 47 2434–2441 (2006).
 86. Zong, X. *et al.* Structure and process relationship of electrospun bioabsorbable nanofiber membranes. *Polymer* **43**, 4403–4412 (2002).
 87. Cárdenas, J. R., de França, M. G. O., de Vasconcelos, E. A., de Azevedo, W. M. & da Silva, E. F. Growth of sub-micron fibres of pure polyaniline using the electrospinning technique. *Journal of Physics D: Applied Physics* vol. 40 1068–1071 (2007).
 88. Reneker, D. H., Kataphinan, W., Theron, A., Zussman, E. & Yarin, A. L. Nanofiber garlands of polycaprolactone by electrospinning. *Polymer* vol. 43 6785–6794 (2002).
 89. Li, W.-J., Danielson, K. G., Alexander, P. G. & Tuan, R. S. Biological response of chondrocytes

- cultured in three-dimensional nanofibrous poly(epsilon-caprolactone) scaffolds. *J. Biomed. Mater. Res. A* **67**, 1105–1114 (2003).
90. Li, W.-J. W.-J. *et al.* A three-dimensional nanofibrous scaffold for cartilage tissue engineering using human mesenchymal stem cells. *Biomaterials* **26**, 599–609 (2005).
 91. Chew, S. Y., Mi, R., Hoke, A. & Leong, K. W. Aligned protein-polymer composite fibers enhance nerve regeneration: a potential tissue-engineering platform. *Adv. Funct. Mater.* **17**, 1288–1296 (2007).
 92. Laforgue, A. & Robitaille, L. Production of conductive PEDOT nanofibers by the combination of electrospinning and vapor-phase polymerization. *Macromolecules* vol. 43 4194–4200 (2010).
 93. Liu, N. *et al.* Electrospun PEDOT:PSS–PVA nanofiber based ultrahigh-strain sensors with controllable electrical conductivity. *Journal of Materials Chemistry* vol. 21 18962 (2011).
 94. Jaeger, R., Bergshoeff, M. M., Battle, C. M. I., Schönherr, H. & Julius Vancso, G. Electrospinning of ultra-thin polymer fibers. *Macromolecular Symposia* vol. 127 141–150 (1998).
 95. Li, L. & Hsieh, Y.-L. Ultra-fine polyelectrolyte fibers from electrospinning of poly(acrylic acid). *Polymer* vol. 46 5133–5139 (2005).
 96. Liu, Y., Chen, J., Misoska, V. & Wallace, G. G. Preparation of novel ultrafine fibers based on DNA and poly(ethylene oxide) by electrospinning from aqueous solutions. *Reactive and Functional Polymers* vol. 67 461–467 (2007).
 97. Ma, Z., Kotaki, M., Yong, T., He, W. & Ramakrishna, S. Surface engineering of electrospun polyethylene terephthalate (PET) nanofibers towards development of a new material for blood vessel engineering. *Biomaterials* **26**, 2527–2536 (2005).
 98. Savoji, H. *et al.* Electrospun nanofiber scaffolds and plasma polymerization: a promising combination towards complete, stable endothelial lining for vascular grafts. *Macromol. Biosci.* **14**, 1084–1095 (2014).
 99. Kenawy, E.-R. *et al.* Release of tetracycline hydrochloride from electrospun

- poly(ethylene-co-vinylacetate), poly(lactic acid), and a blend. *Journal of Controlled Release* vol. 81 57–64 (2002).
100. Luu, Y. K., Kim, K., Hsiao, B. S., Chu, B. & Hadjiargyrou, M. Development of a nanostructured DNA delivery scaffold via electrospinning of PLGA and PLA–PEG block copolymers. *Journal of Controlled Release* vol. 89 341–353 (2003).
 101. Kim, K. *et al.* Control of degradation rate and hydrophilicity in electrospun non-woven poly(D,L-lactide) nanofiber scaffolds for biomedical applications. *Biomaterials* **24**, 4977–4985 (2003).
 102. Uematsu, K. *et al.* Cartilage regeneration using mesenchymal stem cells and a three-dimensional poly-lactic-glycolic acid (PLGA) scaffold. *Biomaterials* vol. 26 4273–4279 (2005).
 103. Sahoo, S., Ang, L. T., Goh, J. C.-H. & Toh, S.-L. Growth factor delivery through electrospun nanofibers in scaffolds for tissue engineering applications. *J. Biomed. Mater. Res. A* **93**, 1539–1550 (2010).
 104. Viry, L. *et al.* Emulsion-coaxial electrospinning: designing novel architectures for sustained release of highly soluble low molecular weight drugs. *Journal of Materials Chemistry* vol. 22 11347 (2012).
 105. Kang, T. S., Lee, S. W., Joo, J. & Lee, J. Y. Electrically conducting polypyrrole fibers spun by electrospinning. *Synthetic Metals* vol. 153 61–64 (2005).
 106. Verreck, G., Chun, I., Peeters, J., Rosenblatt, J. & Brewster, M. E. Preparation and characterization of nanofibers containing amorphous drug dispersions generated by electrostatic spinning. *Pharm. Res.* **20**, 810–817 (2003).
 107. Riboldi, S. A., Sampaolesi, M., Neuenschwander, P., Cossu, G. & Mantero, S. Electrospun degradable polyesterurethane membranes: potential scaffolds for skeletal muscle tissue engineering. *Biomaterials* **26**, 4606–4615 (2005).
 108. Angammana, C. J. & Jayaram, S. H. Analysis of the effects of solution conductivity on electrospinning process and fiber morphology. *IEEE Trans. Ind. Appl.* **47**, 1109–1117 (2011).

109. Xue, N. *et al.* Rapid patterning of 1-D collagenous topography as an ECM protein fibril platform for image cytometry. *PLoS One* **9**, e93590 (2014).
110. Sill, T. J. & von Recum, H. A. Electrospinning: Applications in drug delivery and tissue engineering. *Biomaterials* **29**, 1989–2006 (2008).
111. Ru, C., Chen, J., Shao, Z., Pang, M. & Luo, J. A novel mathematical model for controllable near-field electrospinning. *AIP Adv.* **4**, 017108 (2014).
112. Paschen, F. Ueber die zum Funkenübergang in Luft, Wasserstoff und Kohlensäure bei verschiedenen Drucken erforderliche Potentialdifferenz. *Annalen der Physik* vol. 273 69–96 (1889).
113. Khan, W. S., Asmatulu, R., Ceylan, M. & Jabbarnia, A. Recent progress on conventional and non-conventional electrospinning processes. *Fibers Polym.* **14**, 1235–1247 (2013).
114. Townsend-Nicholson, A. & Jayasinghe, S. N. Cell electrospinning: a unique biotechnique for encapsulating living organisms for generating active biological microthreads/scaffolds. *Biomacromolecules* vol. 7 3364–3369 (2006).
115. Jayasinghe, S. N., Irvine, S. & McEwan, J. R. Cell electrospinning highly concentrated cellular suspensions containing primary living organisms into cell-bearing threads and scaffolds. *Nanomedicine* vol. 2 555–567 (2007).
116. Teo, W.-E., Inai, R. & Ramakrishna, S. Technological advances in electrospinning of nanofibers. *Sci. Technol. Adv. Mater.* **12**, 013002 (2011).
117. Jungst, T. *et al.* Melt electrospinning onto cylinders: effects of rotational velocity and collector diameter on morphology of tubular structures. *Polym. Int.* **64**, 1086–1095 (2015).
118. Munir, M. M. *et al.* Fabrication of poly(acrylonitrile)/PAN nanofiber using a drum collector electrospinning system for water purification application. *Adv. Mat. Res.* **1123**, 281–284 (2015).
119. Chang, G. & Shen, J. Fabrication of microropes via bi-electrospinning with a rotating needle collector. *Macromol. Rapid Commun.* **31**, 2151–2154 (2010).
120. Theron, A., Zussman, E. & Yarin, A. L. Electrostatic field-assisted alignment of electrospun

- nanofibres. *Nanotechnology* **12**, 384–390 (2001).
121. Zussman, E., Theron, A. & Yarin, A. L. Formation of nanofiber crossbars in electrospinning. *Appl. Phys. Lett.* **82**, 973–975 (2003).
 122. Viswanadam, G. & Chase, G. G. Modified electric fields to control the direction of electrospinning jets. *Polymer* **54**, 1397–1404 (2013).
 123. Kessick, R., Royal Kessick, Fenn, J. & Tepper, G. The use of AC potentials in electrospraying and electrospinning processes. *Polymer* **45**, 2981–2984 (2004).
 124. Pelipenko, J., Kristl, J., Janković, B., Baumgartner, S. & Kocbek, P. The impact of relative humidity during electrospinning on the morphology and mechanical properties of nanofibers. *Int. J. Pharm.* **456**, 125–134 (2013).
 125. Agarwal, S., Greiner, A. & Wendorff, J. H. Functional materials by electrospinning of polymers. *Prog. Polym. Sci.* **38**, 963–991 (2013).
 126. Raspa, A., Pugliese, R., Maleki, M. & Gelain, F. Recent therapeutic approaches for spinal cord injury. *Biotechnol. Bioeng.* **113**, 253–259 (2015).
 127. Luo, C. J., Stoyanov, S. D., Stride, E., Pelan, E. & Edirisinghe, M. Electrospinning versus fibre production methods: from specifics to technological convergence. *Chem. Soc. Rev.* **41**, 4708–4735 (2012).
 128. Teng, Y. D. *et al.* Functional recovery following traumatic spinal cord injury mediated by a unique polymer scaffold seeded with neural stem cells. *Proc. Natl. Acad. Sci. U. S. A.* **99**, 3024–3029 (2002).
 129. Oudega, M. *et al.* Axonal regeneration into Schwann cell grafts within resorbable poly(alpha-hydroxyacid) guidance channels in the adult rat spinal cord. *Biomaterials* **22**, 1125–1136 (2001).
 130. Lee, J. Y., Bashur, C. A., Goldstein, A. S. & Schmidt, C. E. Polypyrrole-coated electrospun PLGA nanofibers for neural tissue applications. *Biomaterials* **30**, 4325–4335 (2009).
 131. Kitsara, M. *et al.* Fabrication of cardiac patch by using electrospun collagen fibers.

- Microelectron. Eng.* **144**, 46–50 (2015).
132. Jiang, Q., Reddy, N., Zhang, S., Roscioli, N. & Yang, Y. Water-stable electrospun collagen fibers from a non-toxic solvent and crosslinking system. *J. Biomed. Mater. Res. A* **101**, 1237–1247 (2013).
 133. Zeleny, J. Instability of electrified liquid surfaces. *Physical Review* **10**, 1–6 (1917).
 134. Taylor, G. Electrically Driven Jets. *Proceedings of the Royal Society A: Mathematical, Physical and Engineering Sciences* **313**, 453–475 (1969).
 135. Baumgarten, P. K. Electrostatic spinning of acrylic microfibers. *J. Colloid Interface Sci.* **36**, 71–79 (1971).
 136. Doshi, J. & Reneker, D. H. Electrospinning process and applications of electrospun fibers. *J. Electrostat.* **35**, 151–160 (1995).
 137. Sun, D., Chang, C., Li, S. & Lin, L. Near-field electrospinning. *Nano Lett.* **6**, 839–842 (2006).
 138. Chang, C., Limkralassiri, K. & Lin, L. Continuous near-field electrospinning for large area deposition of orderly nanofiber patterns. *Appl. Phys. Lett.* **93**, 123111 (2008).
 139. Huang, Y. *et al.* Versatile, kinetically controlled, high precision electrohydrodynamic writing of micro/nanofibers. *Sci. Rep.* **4**, 5949 (2014).
 140. Zheng, G. *et al.* Electrohydrodynamic direct-writing of three-dimensional multi-loop nanofibrous coils. *Appl. Phys. A: Mater. Sci. Process.* **116**, 171–177 (2014).
 141. Kessick, R., Royal Kessick & Tepper, G. Microscale polymeric helical structures produced by electrospinning. *Appl. Phys. Lett.* **84**, 4807–4809 (2004).
 142. Bisht, G. S. *et al.* Controlled continuous patterning of polymeric nanofibers on three-dimensional substrates using low-voltage near-field electrospinning. *Nano Lett.* **11**, 1831–1837 (2011).
 143. Hochleitner, G. *et al.* Fibre pulsing during melt electrospinning writing. *BioNanoMaterials* **17**, (2016).
 144. Xu, J. *et al.* Accuracy improvement of nano-fiber deposition by near-field electrospinning. in *IWMF 9th International Workshop on Microfactories* (2014).

145. Martinez-Prieto, N. *et al.* Feasibility of fiber-deposition control by secondary electric fields in near-field electrospinning. *Journal of Micro and Nano-Manufacturing* **3**, 041005 (2015).
146. Lee, M. & Kim, H.-Y. Toward nanoscale three-dimensional printing: nanowalls built of electrospun nanofibers. *Langmuir* **30**, 1210–1214 (2014).
147. Wang, H. *et al.* Deposition characteristics of the double nozzles near-field electrospinning. *Appl. Phys. A: Mater. Sci. Process.* **118**, 621–628 (2014).
148. Wang, Z. *et al.* Controllable deposition distance of aligned pattern via dual-nozzle near-field electrospinning. *AIP Adv.* **7**, 035310 (2017).
149. Wang, Z. *et al.* Fabrication and evaluation of controllable deposition distance for aligned pattern by multi-nozzle near-field electrospinning. *AIP Adv.* **8**, 075111 (2018).
150. Yen, C. K. *et al.* Electrospun PVDF fibers on bio-wings using multi-spinnerets. in *The 9th IEEE International Conference on Nano/Micro Engineered and Molecular Systems (NEMS)* (2014). doi:10.1109/nems.2014.6908885.
151. Deitzel, J. Controlled deposition of electrospun poly(ethylene oxide) fibers. *Polymer* **42**, 8163–8170 (2001).
152. Bellan, L. M. & Craighead, H. G. Control of an electrospinning jet using electric focusing and jet-steering fields. *J. Vac. Sci. Technol. B Microelectron. Nanometer Struct. Process. Meas. Phenom.* **24**, 3179 (2006).
153. Zhu, Z. *et al.* The process of wavy fiber deposition via auxiliary electrodes in near-field electrospinning. *Appl. Phys. A: Mater. Sci. Process.* **120**, 1435–1442 (2015).
154. Laurencin, C. T., Ambrosio, A. M., Borden, M. D. & Cooper, J. A., Jr. Tissue engineering: orthopedic applications. *Annu. Rev. Biomed. Eng.* **1**, 19–46 (1999).
155. Fuh, Y. K., Chen, S. Z. & He, Z. Y. Direct-write, highly aligned chitosan-poly(ethylene oxide) nanofiber patterns for cell morphology and spreading control. *Nanoscale Res. Lett.* **8**, 97 (2013).
156. Fuh, Y.-K., Wu, Y.-C., He, Z.-Y., Huang, Z.-M. & Hu, W.-W. The control of cell orientation using biodegradable alginate fibers fabricated by near-field electrospinning. *Mater. Sci. Eng. C*

- Mater. Biol. Appl.* **62**, 879–887 (2016).
157. Castilho, M. *et al.* Mechanical behavior of a soft hydrogel reinforced with three-dimensional printed microfibre scaffolds. *Scientific Reports* vol. 8 (2018).
 158. Hrynevich, A. *et al.* Dimension-based design of melt electrowritten scaffolds. *Small* **14**, e1800232 (2018).
 159. Chen, Z. *et al.* Biomaterials for corneal bioengineering. *Biomedical Materials* vol. 13 032002 (2018).
 160. SangHoon Lee *et al.* Chip-to-chip fluidic connectors via near-field electrospinning. in *2007 IEEE 20th International Conference on Micro Electro Mechanical Systems (MEMS)* (2007). doi:10.1109/memsys.2007.4433013.
 161. Bhullar, S. K., Kaya, B. & Jun, M. B.-G. Development of bioactive packaging structure using melt electrospinning. *J. Polym. Environ.* **23**, 416–423 (2015).
 162. Dalton, P. D., Klinkhammer, K., Salber, J., Klee, D. & Möller, M. Direct in vitro electrospinning with polymer melts. *Biomacromolecules* **7**, 686–690 (2006).
 163. Muerza-Cascante, M. L., Haylock, D., Hutmacher, D. W. & Dalton, P. D. Melt electrospinning and its technologization in tissue engineering. *Tissue Eng. Part B Rev.* **21**, 187–202 (2015).
 164. Brown, T. D., Dalton, P. D. & Hutmacher, D. W. Direct writing by way of melt electrospinning. *Adv. Mater.* **23**, 5651–5657 (2011).
 165. Farrugia, B. L. *et al.* Dermal fibroblast infiltration of poly(ϵ -caprolactone) scaffolds fabricated by melt electrospinning in a direct writing mode. *Biofabrication* **5**, 025001 (2013).
 166. Ristovski, N. *et al.* Improved fabrication of melt electrospun tissue engineering scaffolds using direct writing and advanced electric field control. *Biointerphases* **10**, 011006 (2015).
 167. Hochleitner, G. *et al.* Additive manufacturing of scaffolds with sub-micron filaments via melt electrospinning writing. *Biofabrication* **7**, 035002 (2015).
 168. McColl, E., Groll, J., Jungst, T. & Dalton, P. D. Design and fabrication of melt electrowritten tubes using intuitive software. *Mater. Des.* **155**, 46–58 (2018).

169. Kim, H.-Y., Lee, M., Park, K. J., Kim, S. & Mahadevan, L. Nanopottery: coiling of electrospun polymer nanofibers. *Nano Lett.* **10**, 2138–2140 (2010).
170. Lee, J., Lee, S. Y., Jang, J., Jeong, Y. H. & Cho, D.-W. Fabrication of patterned nanofibrous mats using direct-write electrospinning. *Langmuir* **28**, 7267–7275 (2012).
171. Luo, G. *et al.* Direct-write, self-aligned electrospinning on paper for controllable fabrication of three-dimensional structures. *ACS Appl. Mater. Interfaces* **7**, 27765–27770 (2015).
172. He, J., Xu, F., Dong, R., Guo, B. & Li, D. Electrohydrodynamic 3D printing of microscale poly (ϵ -caprolactone) scaffolds with multi-walled carbon nanotubes. *Biofabrication* **9**, 015007 (2017).
173. Zhu, P. *et al.* Fabrication of three-dimensional nanofibrous macrostructures by electrospinning. *AIP Adv.* **6**, 055304 (2016).
174. Liang, F. *et al.* Fabrication of three-dimensional micro-nanofiber structures by a novel solution blow spinning device. *AIP Adv.* **7**, 025002 (2017).
175. Tokarev, A. *et al.* Touch- and Brush-Spinning of Nanofibers. *Adv. Mater.* **27**, 6526–6532 (2015).
176. Zhang, K., Wang, X., Jing, D., Yang, Y. & Zhu, M. Bionic electrospun ultrafine fibrous poly(L-lactic acid) scaffolds with a multi-scale structure. *Biomed. Mater.* **4**, 035004 (2009).
177. Li, D., Wang, Y. & Xia, Y. Electrospinning Nanofibers as Uniaxially Aligned Arrays and Layer-by-Layer Stacked Films. *Adv. Mater.* **16**, 361–366 (2004).
178. Chen, D. *et al.* Polyaniline nanofiber gas sensors by direct-write electrospinning. in *2011 IEEE 24th International Conference on Micro Electro Mechanical Systems* (2011).
doi:10.1109/memsys.2011.5734689.
179. Kriebel, A. *et al.* Three-dimensional configuration of orientated fibers as guidance structures for cell migration and axonal growth. *J. Biomed. Mater. Res. B Appl. Biomater.* **102**, 356–365 (2014).
180. Li, D., Wang, Y. & Xia, Y. Electrospinning of polymeric and ceramic nanofibers as uniaxially aligned arrays. *Nano Lett.* **3**, 1167–1171 (2003).
181. Fuh, Y.-K., Chen, S.-Y. & Ye, J.-C. Massively parallel aligned microfibers-based harvester

- deposited via in situ, oriented poled near-field electrospinning. *Appl. Phys. Lett.* **103**, 033114 (2013).
182. Liu, L. & Dzenis, Y. A. Analysis of the effects of the residual charge and gap size on electrospun nanofiber alignment in a gap method. *Nanotechnology* **19**, 355307 (2008).
 183. Baker, S. R., Banerjee, S., Bonin, K. & Guthold, M. Determining the mechanical properties of electrospun poly- ϵ -caprolactone (PCL) nanofibers using AFM and a novel fiber anchoring technique. *Materials Science and Engineering: C* vol. 59 203–212 (2016).
 184. Beachley, V., Katsanevakis, E., Zhang, N. & Wen, X. A novel method to precisely assemble loose nanofiber structures for regenerative medicine applications. *Adv. Healthc. Mater.* **2**, 343–351 (2012).
 185. Pu, J., Yan, X., Jiang, Y., Chang, C. & Lin, L. Piezoelectric actuation of direct-write electrospun fibers. *Sensors and Actuators A: Physical* vol. 164 131–136 (2010).
 186. Dalton, P. D., Klee, D. & Möller, M. Electrospinning with dual collection rings. *Polymer* vol. 46 611–614 (2005).
 187. Liu, Y. *et al.* Effects of solution properties and electric field on the electrospinning of hyaluronic acid. *Carbohydr. Polym.* **83**, 1011–1015 (2011).
 188. Students, C. A. On the 100th anniversary of the birth of I.V. Petryanov-Sokolov. *Izv. Atmos. Ocean. Phys.* **43**, 395–395 (2007).
 189. Annis, D. *et al.* An elastomeric vascular prosthesis. *Trans. Am. Soc. Artif. Intern. Organs* **24**, 209–214 (1978).
 190. Larrondo, L. & St. John Manley, R. Electrostatic fiber spinning from polymer melts. I. Experimental observations on fiber formation and properties. *Journal of Polymer Science: Polymer Physics Edition* **19**, 909–920 (1981).
 191. Fisher, A. C., De Cossart, L., How, T. V. & Annis, D. Long term in-vivo performance of an electrostatically-spun small bore arterial prosthesis: the contribution of mechanical compliance and anti-platelet therapy. *Life Support Syst.* **3 Suppl 1**, 462–465 (1985).

192. He, J.-H., Liu, Y. & Xu, L. Apparatus for preparing electrospun nanofibres: a comparative review. *Mater. Sci. Technol.* **26**, 1275–1287 (2010).
193. He, F.-L. *et al.* A novel layer-structured scaffold with large pore sizes suitable for 3D cell culture prepared by near-field electrospinning. *Mater. Sci. Eng. C Mater. Biol. Appl.* **86**, 18–27 (2018).
194. Luo, G. *et al.* High aspect-ratio 3D microstructures via near-field electrospinning for energy storage applications. in *2016 IEEE 29th International Conference on Micro Electro Mechanical Systems (MEMS)* (2016). doi:10.1109/memsys.2016.7421549.
195. Fattahi, P., Dover, J. T. & Brown, J. L. 3D near-field electrospinning of biomaterial microfibers with potential for blended microfiber-cell-loaded gel composite structures. *Adv. Healthc. Mater.* **6**, (2017).
196. Bisht, G., Nesterenko, S., Kulinsky, L. & Madou, M. A computer-controlled near-field electrospinning setup and its graphic user interface for precision patterning of functional nanofibers on 2D and 3D substrates. *J. Lab. Autom.* **17**, 302–308 (2012).
197. Kwon, K.-S. & Lee, D.-Y. Investigation of pulse voltage shape effects on electrohydrodynamic jets using a vision measurement technique. *J. Micromech. Microeng.* **23**, 065018 (2013).
198. Phung, T. H., Kim, S. & Kwon, K.-S. A high speed electrohydrodynamic (EHD) jet printing method for line printing. *J. Micromech. Microeng.* **27**, 095003 (2017).
199. Chang, C., Tran, V. H., Wang, J., Fuh, Y.-K. & Lin, L. Direct-write piezoelectric polymeric nanogenerator with high energy conversion efficiency. *Nano Lett.* **10**, 726–731 (2010).
200. Shen, C., Wang, C.-P., Sanghadasa, M. & Lin, L. Flexible micro-supercapacitors prepared using direct-write nanofibers. *RSC Adv.* **7**, 11724–11731 (2017).
201. Liu, Z. H. *et al.* Crystallization and mechanical behavior of the ferroelectric polymer nonwoven fiber fabrics for highly durable wearable sensor applications. *Appl. Surf. Sci.* **346**, 291–301 (2015).
202. He, X.-X. *et al.* Near-field electrospinning: progress and applications. *J. Phys. Chem. C* **121**, 8663–8678 (2017).

203. Liao, I.-C., Moutos, F. T., Estes, B. T., Zhao, X. & Guilak, F. Composite three-dimensional woven scaffolds with interpenetrating network hydrogels to create functional synthetic articular cartilage. *Adv. Funct. Mater.* **23**, 5833–5839 (2013).
204. McMahon, R. E. *et al.* Hydrogel-electrospun mesh composites for coronary artery bypass grafts. *Tissue Eng. Part C Methods* **17**, 451–461 (2011).
205. Cullen, D. K. *et al.* Microtissue engineered constructs with living axons for targeted nervous system reconstruction. *Tissue Eng. Part A* **18**, 2280–2289 (2012).
206. Schrobback, K., Klein, T. J. & Woodfield, T. B. F. The importance of connexin hemichannels during chondroprogenitor cell differentiation in hydrogel versus microtissue culture models. *Tissue Eng. Part A* **21**, 1785–1794 (2015).
207. Legant, W. R., Chen, C. S. & Vogel, V. Force-induced fibronectin assembly and matrix remodeling in a 3D microtissue model of tissue morphogenesis. *Integr. Biol.* **4**, 1164–1174 (2012).
208. Zhang, B. G. X. *et al.* Recent advances in nerve tissue engineering. *Int. J. Artif. Organs* **37**, 277–291 (2014).
209. Vieira, M. S. *et al.* Neural stem cell differentiation into mature neurons: Mechanisms of regulation and biotechnological applications. *Biotechnol. Adv.* **36**, 1946–1970 (2018).
210. Flemming, R. G., Murphy, C. J., Abrams, G. A., Goodman, S. L. & Nealey, P. F. Effects of synthetic micro- and nano-structured surfaces on cell behavior. *Biomaterials* **20**, 573–588 (1999).
211. Abrams, G. A., Schaus, S. S., Goodman, S. L., Nealey, P. F. & Murphy, C. J. Nanoscale topography of the corneal epithelial basement membrane and Descemet's membrane of the human. *Cornea* **19**, 57–64 (2000).
212. Morrison, S. J. & Spradling, A. C. Stem cells and niches: mechanisms that promote stem cell maintenance throughout life. *Cell* **132**, 598–611 (2008).
213. Semino, C. E., Merok, J. R., Crane, G. G., Panagiotakos, G. & Zhang, S. Functional differentiation of hepatocyte-like spheroid structures from putative liver progenitor cells in

- three-dimensional peptide scaffolds. *Differentiation* **71**, 262–270 (2003).
214. Yao, L., O'Brien, N., Windebank, A. & Pandit, A. Orienting neurite growth in electrospun fibrous neural conduits. *J. Biomed. Mater. Res. B Appl. Biomater.* **90**, 483–491 (2009).
 215. Quigley, A. F. *et al.* A conducting-polymer platform with biodegradable fibers for stimulation and guidance of axonal growth. *Adv. Mater.* **21**, 4393–4397 (2009).
 216. Liu, X. *et al.* Guidance of neurite outgrowth on aligned electrospun polypyrrole/poly(styrene-beta-isobutylene-beta-styrene) fiber platforms. *J. Biomed. Mater. Res. A* **94**, 1004–1011 (2010).
 217. Neal, R. A. *et al.* Alignment and composition of laminin-polycaprolactone nanofiber blends enhance peripheral nerve regeneration. *J. Biomed. Mater. Res. A* **100**, 406–423 (2012).
 218. Agarwal, S., Wendorff, J. H. & Greiner, A. Progress in the field of electrospinning for tissue engineering applications. *Adv. Mater.* **21**, 3343–3351 (2009).
 219. Bajgai, M. P. *et al.* Poly(ϵ -caprolactone) grafted dextran biodegradable electrospun matrix: A novel scaffold for tissue engineering. *J. Appl. Polym. Sci.* **108**, 1447–1454 (2008).
 220. Zhu, Y., Cao, Y., Pan, J. & Liu, Y. Macro-alignment of electrospun fibers for vascular tissue engineering. *J. Biomed. Mater. Res. B Appl. Biomater.* **92**, 508–516 (2010).
 221. Stitzel, J. *et al.* Controlled fabrication of a biological vascular substitute. *Biomaterials* **27**, 1088–1094 (2006).
 222. Yixiang, D., Yong, T., Liao, S., Chan, C. K. & Ramakrishna, S. Degradation of electrospun nanofiber scaffold by short wave length ultraviolet radiation treatment and its potential applications in tissue engineering. *Tissue Eng. Part A* **14**, 1321–1329 (2008).
 223. He, W., Ma, Z., Yong, T., Teo, W. E. & Ramakrishna, S. Fabrication of collagen-coated biodegradable polymer nanofiber mesh and its potential for endothelial cells growth. *Biomaterials* **26**, 7606–7615 (2005).
 224. Wei, J. *et al.* Electrohydrodynamic Direct Writing Platform Based on Near-Field Electrospinning. *Key Eng. Mater.* **562-565**, 614–619 (2013).

225. Hotaling, N. A., Bharti, K., Kriel, H. & Simon, C. G., Jr. DiameterJ: A validated open source nanofiber diameter measurement tool. *Biomaterials* **61**, 327–338 (2015).
226. Rezakhaniha, R. *et al.* Experimental investigation of collagen waviness and orientation in the arterial adventitia using confocal laser scanning microscopy. *Biomech. Model. Mechanobiol.* **11**, 461–473 (2011).
227. Sacks, M. S., Smith, D. B. & Hiester, E. D. A small angle light scattering device for planar connective tissue microstructural analysis. *Ann. Biomed. Eng.* **25**, 678–689 (1997).
228. D’Amore, A., Stella, J. A., Wagner, W. R. & Sacks, M. S. Characterization of the complete fiber network topology of planar fibrous tissues and scaffolds. *Biomaterials* **31**, 5345–5354 (2010).
229. Tutak, W. *et al.* The support of bone marrow stromal cell differentiation by airbrushed nanofiber scaffolds. *Biomaterials* **34**, 2389–2398 (2013).
230. Jaworek, A. & Sobczyk, A. T. Electro spraying route to nanotechnology: An overview. *J. Electrostat.* **66**, 197–219 (2008).
231. Liu, J. *et al.* Bead-on-string structure printed by electrohydrodynamic jet under alternating current electric field. *Appl. Phys. A: Mater. Sci. Process.* **122**, (2016).
232. Zhang, T. Y. & Suen, C. Y. A fast parallel algorithm for thinning digital patterns. *Commun. ACM* **27**, 236–239 (1984).
233. Yao, J., Bastiaansen, C. & Peijs, T. High strength and high modulus electrospun nanofibers. *Fibers* vol. 2 158–186 (2014).
234. World Health Organization. *Neurological Disorders: Public Health Challenges*. (World Health Organization, 2006).
235. Vaz, C. M., van Tuijl, S., Bouten, C. V. C. & Baaijens, F. P. T. Design of scaffolds for blood vessel tissue engineering using a multi-layering electrospinning technique. *Acta Biomater.* **1**, 575–582 (2005).
236. Whang, K., Thomas, C. H., Healy, K. E. & Nuber, G. A novel method to fabricate bioabsorbable scaffolds. *Polymer* vol. 36 837–842 (1995).

237. O'Brien, F. J. *et al.* The effect of pore size on permeability and cell attachment in collagen scaffolds for tissue engineering. *Technol. Health Care* **15**, 3–17 (2007).
238. O'Brien, F. J., Harley, B. A., Yannas, I. V. & Gibson, L. J. The effect of pore size on cell adhesion in collagen-GAG scaffolds. *Biomaterials* **26**, 433–441 (2005).
239. Nisbet, D. R., Forsythe, J. S., Shen, W., Finkelstein, D. I. & Horne, M. K. Review paper: a review of the cellular response on electrospun nanofibers for tissue engineering. *J. Biomater. Appl.* **24**, 7–29 (2009).
240. Banerjee, M. & Bhonde, R. R. Application of hanging drop technique for stem cell differentiation and cytotoxicity studies. *Cytotechnology* **51**, 1–5 (2006).
241. Smedt, A. D. *et al.* Optimisation of the cell cultivation methods in the embryonic stem cell test results in an increased differentiation potential of the cells into strong beating myocard cells. *Toxicology in Vitro* vol. 22 1789–1796 (2008).
242. Chen, X. *et al.* Shell-core bi-layered scaffolds for engineering of vascularized osteon-like structures. *Biomaterials* **34**, 8203–8212 (2013).
243. Sharma, R., Barakzai, S. Z., Taylor, S. E. & Donadeu, F. X. Epidermal-like architecture obtained from equine keratinocytes in three-dimensional cultures. *J. Tissue Eng. Regen. Med.* **10**, 627–636 (2016).
244. Levenberg, S., Burdick, J. A., Kraehenbuehl, T. & Langer, R. Neurotrophin-induced differentiation of human embryonic stem cells on three-dimensional polymeric scaffolds. *Tissue Engineering* vol. 11 506–512 (2005).
245. Wells, E. K., Yarborough, O., 3rd, Lifton, R. P., Cantley, L. G. & Caplan, M. J. Epithelial morphogenesis of MDCK cells in three-dimensional collagen culture is modulated by interleukin-8. *Am. J. Physiol. Cell Physiol.* **304**, C966–75 (2013).
246. Ferreira, L. S. *et al.* Bioactive hydrogel scaffolds for controllable vascular differentiation of human embryonic stem cells. *Biomaterials* **28**, 2706–2717 (2007).
247. Chwalek, K., Tsurkan, M. V., Freudenberg, U. & Werner, C. Glycosaminoglycan-based

- hydrogels to modulate heterocellular communication in in vitro angiogenesis models. *Sci. Rep.* **4**, 4414 (2014).
248. Lien, S.-M., Ko, L.-Y. & Huang, T.-J. Effect of pore size on ECM secretion and cell growth in gelatin scaffold for articular cartilage tissue engineering. *Acta Biomater.* **5**, 670–679 (2009).
249. Zhang, X. N. *et al.* A tough and stiff hydrogel with tunable water content and mechanical properties based on the synergistic effect of hydrogen bonding and hydrophobic interaction. *Macromolecules* vol. 51 8136–8146 (2018).
250. Pescosolido, L. *et al.* Mesh size distribution determination of interpenetrating polymer network hydrogels. *Soft Matter* vol. 8 7708 (2012).
251. Gutowska, A., Jeong, B. & Jasionowski, M. Injectable gels for tissue engineering. *Anat. Rec.* **263**, 342–349 (2001).
252. Gupta, D., Tator, C. H. & Shoichet, M. S. Fast-gelling injectable blend of hyaluronan and methylcellulose for intrathecal, localized delivery to the injured spinal cord. *Biomaterials* **27**, 2370–2379 (2006).
253. Jain, A., Kim, Y.-T., McKeon, R. J. & Bellamkonda, R. V. In situ gelling hydrogels for conformational repair of spinal cord defects, and local delivery of BDNF after spinal cord injury. *Biomaterials* vol. 27 497–504 (2006).
254. Coburn, J. *et al.* Biomimetics of the extracellular matrix: an integrated three-dimensional fiber-hydrogel composite for cartilage tissue engineering. *Smart Struct. Syst.* **7**, 213–222 (2011).
255. Hsieh, A. *et al.* Hydrogel/electrospun fiber composites influence neural stem/progenitor cell fate. *Soft Matter* **6**, 2227 (2010).
256. Ruel-Gariépy, E. & Leroux, J.-C. In situ-forming hydrogels--review of temperature-sensitive systems. *Eur. J. Pharm. Biopharm.* **58**, 409–426 (2004).
257. Anseth, K. S., Bowman, C. N. & Brannon-Peppas, L. Mechanical properties of hydrogels and their experimental determination. *Biomaterials* vol. 17 1647–1657 (1996).
258. Stammen, J. A., Williams, S., Ku, D. N. & Guldberg, R. E. Mechanical properties of a novel

- PVA hydrogel in shear and unconfined compression. *Biomaterials* **22**, 799–806 (2001).
259. Jeon, O. *et al.* Mechanical properties and degradation behaviors of hyaluronic acid hydrogels cross-linked at various cross-linking densities. *Carbohydrate Polymers* vol. 70 251–257 (2007).
260. Matthews, J. A., Boland, E. D., Wnek, G. E., Simpson, D. G. & Bowlin, G. L. Electrospinning of collagen type II: a feasibility study. *J. Bioact. Compat. Polym.* **18**, 125–134 (2003).
261. Wang, B., Cai, Q., Zhang, S., Yang, X. & Deng, X. The effect of poly (L-lactic acid) nanofiber orientation on osteogenic responses of human osteoblast-like MG63 cells. *J. Mech. Behav. Biomed. Mater.* **4**, 600–609 (2011).
262. Li, W.-J., Laurencin, C. T., Catterson, E. J., Tuan, R. S. & Ko, F. K. Electrospun nanofibrous structure: A novel scaffold for tissue engineering. *J. Biomed. Mater. Res.* **60**, 613–621 (2002).
263. Ekaputra, A. K., Prestwich, G. D., Cool, S. M. & Hutmacher, D. W. Combining electrospun scaffolds with electrosprayed hydrogels leads to three-dimensional cellularization of hybrid constructs. *Biomacromolecules* **9**, 2097–2103 (2008).
264. Shin, H. J. *et al.* Electrospun PLGA nanofiber scaffolds for articular cartilage reconstruction: mechanical stability, degradation and cellular responses under mechanical stimulation in vitro. *J. Biomater. Sci. Polym. Ed.* **17**, 103–119 (2006).
265. Balgud, A. *et al.* Tailoring fiber diameter in electrospun poly(ϵ -caprolactone) scaffolds for optimal cellular infiltration in cardiovascular tissue engineering. *Tissue Eng. Part A* **15**, 437–444 (2009).
266. Bacelar, A. H., Silva-Correia, J., Oliveira, J. M. & Reis, R. L. Recent progress in gellan gum hydrogels provided by functionalization strategies. *Journal of Materials Chemistry B* vol. 4 6164–6174 (2016).
267. Liao, J. *et al.* The fabrication of biomimetic biphasic CAN-PAC hydrogel with a seamless interfacial layer applied in osteochondral defect repair. *Bone Res* **5**, 17018 (2017).
268. Fairbanks, B. D., Schwartz, M. P., Bowman, C. N. & Anseth, K. S. Photoinitiated polymerization of PEG-diacrylate with lithium phenyl-2,4,6-trimethylbenzoylphosphinate: polymerization rate

- and cytocompatibility. *Biomaterials* **30**, 6702–6707 (2009).
269. Luo, C. J., Stride, E. & Edirisinghe, M. Mapping the influence of solubility and dielectric constant on electrospinning polycaprolactone solutions. *Macromolecules* **45**, 4669–4680 (2012).
 270. Coutinho, D. F. *et al.* Modified Gellan Gum hydrogels with tunable physical and mechanical properties. *Biomaterials* **31**, 7494–7502 (2010).
 271. Lin, H. *et al.* Application of visible light-based projection stereolithography for live cell-scaffold fabrication with designed architecture. *Biomaterials* **34**, 331–339 (2013).
 272. Potrč, T. *et al.* Electrospun polycaprolactone nanofibers as a potential oromucosal delivery system for poorly water-soluble drugs. *Eur. J. Pharm. Sci.* **75**, 101–113 (2015).
 273. Dash, T. K. & Konkimalla, V. B. Poly-ε-caprolactone based formulations for drug delivery and tissue engineering: A review. *J. Control. Release* **158**, 15–33 (2012).
 274. França, D. C., Bezerra, E. B., de Souza Morais, D. D., Araújo, E. M. & Wellen, R. M. R. Hydrolytic and thermal degradation of PCL and PCL/bentonite compounds. *Materials Research* vol. 19 618–627 (2016).
 275. Sun, H., Mei, L., Song, C., Cui, X. & Wang, P. The in vivo degradation, absorption and excretion of PCL-based implant. *Biomaterials* **27**, 1735–1740 (2006).
 276. Papkov, D. *et al.* Simultaneously strong and tough ultrafine continuous nanofibers. *ACS Nano* vol. 7 3324–3331 (2013).
 277. Lin, Y. *et al.* Mechanical properties of polymer nanofibers revealed by interaction with streams of air. *Polymer* vol. 53 782–790 (2012).
 278. Hwang, K. Y., Kim, S.-D., Kim, Y.-W. & Yu, W.-R. Mechanical characterization of nanofibers using a nanomanipulator and atomic force microscope cantilever in a scanning electron microscope. *Polymer Testing* vol. 29 375–380 (2010).
 279. Bazbouz, M. B. & Stylios, G. K. The tensile properties of electrospun nylon 6 single nanofibers. *Journal of Polymer Science Part B: Polymer Physics* vol. 48 1719–1731 (2010).
 280. Maranchi, J. P., Trexler, M. M., Guo, Q. & Elisseeff, J. H. Fibre-reinforced hydrogels with high

- optical transparency. *Int. Mater. Rev.* **59**, 264–296 (2014).
281. Shakil, U. A., Hassan, S. B. A., Yahya, M. Y. & Nauman, S. Mechanical properties of electrospun nanofiber reinforced/interleaved epoxy matrix composites—A review. *Polymer Composites* (2020) doi:10.1002/pc.25539.
 282. Chew, S. Y., Hufnagel, T. C., Lim, C. T. & Leong, K. W. Mechanical properties of single electrospun drug-encapsulated nanofibres. *Nanotechnology* vol. 17 3880–3891 (2006).
 283. Richard-Lacroix, M. & Pellerin, C. Molecular Orientation in Electrospun Fibers: From Mats to Single Fibers. *Macromolecules* vol. 46 9473–9493 (2013).
 284. Jiang, S., Duan, G., Chen, L., Hu, X. & Hou, H. Mechanical performance of aligned electrospun polyimide nanofiber belt at high temperature. *Materials Letters* vol. 140 12–15 (2015).
 285. Kai, D. *et al.* Mechanical properties and in vitro behavior of nanofiber–hydrogel composites for tissue engineering applications. *Nanotechnology* vol. 23 095705 (2012).
 286. Jiang, S., Hou, H., Greiner, A. & Agarwal, S. Tough and transparent nylon-6 electrospun nanofiber reinforced melamine–formaldehyde composites. *ACS Applied Materials & Interfaces* vol. 4 2597–2603 (2012).
 287. Christenson, E. M. *et al.* Nanobiomaterial applications in orthopedics. *J. Orthop. Res.* **25**, 11–22 (2007).
 288. Zeng, J. *et al.* The direction and stability control system for near-field electrospinning direct-writing technology. *2016 IEEE International Conference on Manipulation, Manufacturing and Measurement on the Nanoscale (3M-NANO)* (2016) doi:10.1109/3m-nano.2016.7824960.
 289. Wang, X., Zheng, G., Luo, Z. & Li, W. Current characteristics of various ejection modes in electrohydrodynamic printing. *AIP Advances* vol. 5 127120 (2015).
 290. Reneker, D. H. & Fong, H. *Polymeric Nanofibers*. (Amer Chemical Society, 2006).
 291. Li, Z., Al-Milaji, K. N., Zhao, H. & Chen, D.-R. Electrohydrodynamic (EHD) jet printing with a circulating dual-channel nozzle. *Journal of Micromechanics and Microengineering* vol. 29 035013 (2019).

292. Youn, D.-H. *et al.* Electrohydrodynamic micropatterning of silver ink using near-field electrohydrodynamic jet printing with tilted-outlet nozzle. *Applied Physics A* vol. 96 933–938 (2009).